Proceedings of the

5th NIRS-SNU

Workshop on Nuclear Medicine Imaging Science and Technology

August 26, 2018 National Institute of Radiological Sciences (NIRS-QST), Chiba, Japan
August 28, 2018 Oxide Corporation, Hokuto, Yamanashi, Japan

Dear Colleagues,

It is our great pleasure to hold the 5th National Institute of Radiological Sciences (NIRS) – Seoul National University (SNU) Workshop on Nuclear Medicine Imaging Science and Technology, from the 26th to 29th of August in Japan.

This workshop disseminates new research in physics and engineering involving the detection of ionizing radiation and quantitative image reconstruction in nuclear medicine imaging. The techniques of primary interest are position emission tomography (PET), single photon emission computed tomography (SPECT) and Compton imaging.

The 1st NIRS-SNU workshop was held successfully in Japan in February 2012 and the 2nd workshop was held in Korea in April 2013. The 3rd and the 4th workshops were held with the valuable support from the Japan Society for the Promotion of Science (JSPS) and the National Research Foundation of Korea (NRF), in Japan in March 2014 and in Korea in April 2016, respectively. The 5th workshop this time is planned with the support of JSPS and NRF as well.

Through this workshop, we will discuss scientific issues and solutions in nuclear medicine physics by sharing the state-of-the-art research results in each research group. This will subsequently lead to advancement of nuclear medicine imaging techniques and its applications in diagnostic and therapeutic areas. We would like to warmly welcome you to the 5th NIRS-SNU Workshop.

Jae Sung Lee,
Seoul National University College of Medicine

Taiga Yamaya,
National Institute of Radiological Sciences (NIRS-QST)

History of the workshops

	Date	Location	Excursion	Support
1st	Jan 24-26, 2012	NIRS (Chiba)	Hitachi Chemical (Ibaraki)	-
2nd	Apr 24-26, 2013	SNU (Seoul)	-	-
3rd	Mar 26-30, 2014	NIRS (Chiba)	Hamamatsu Photonics (Shizuoka)	JSPS/NRF
4th	Apr 18-21, 2016	Jeju	SNU (Seoul)	NRF/JSPS
5th	Aug 26-29, 2018	Oxide (Yamanashi)	NIRS (Chiba)	JSPS/NRF

Table of contents

Introduction of PET imaging physics research at NIRS

Taiga Yamaya[1], *on behalf of the Imaging Physics Team*

[1] National Institute of Radiological Sciences (NIRS-QST), Japan

Abstract

This paper summarized a brief overview of research works under development at Imaging Physics Team at National Institute of Radiological Sciences (NIRS-QST).

1. Introduction

Positron emission tomography (PET) plays important roles in cancer diagnosis, neuroimaging and molecular imaging research. The National Institute of Radiological Sciences (NIRS) has been focusing on PET research since 1979 when NIRS developed the first PET scanner in Japan. However, regarding instrumentations, potential points remain for which big improvements could be made, including spatial resolution, sensitivity and manufacturing costs. Therefore, research on next generation PET technologies remains a hot topic worldwide. The Imaging Physics Team (IPT) is engaging in nuclear medicine physics research by realizing innovative ideas.

2. Whole gamma imaging (WGI) concept

Whole gamma imaging (WGI) is a concept utilizing all detectable gamma rays for imaging by combining PET and Compton imaging. An additional detector ring, which is used as the scatterer, is inserted in a conventional PET ring so that single gamma rays can be detected by the Compton imaging method. As a wide range of radioisotopes can be visualized, WGI is expected to enable imaging of the targeted radioisotope therapy. In addition, triple gamma emitters such as ^{44}Sc, that emits a pair of 511 keV photons and a 1157 keV gamma ray almost at the same time, are selected as an

Figure 1. The WGI prototype

imaging target. In theory, localization from a single decay is possible by identifying the intersection point between a coincidence line and a Compton cone. Following the simulation, we succeeded in prototyping the first WGI system and showed a proof-of-concept of WGI. We showed the localization accuracy of the 12.7mm FWHM which was obtained as the intersection point between a coincidence line and a Compton cone. Further improvement will be possible by optimizing the detectors.

3. Brain dedicated PET systems

Numbers of brain PET scanners have been developed, but all previous prototypes were based on a cylindrical geometry, which is not the most efficient for brain imaging. Making the detector ring as small as possible is essential in PET, because sensitivity can be increased with a limited number of detectors. Therefore, we developed a novel brain dedicated PET, in which DOI detectors are arranged to form a hemisphere, for compact, high-sensitivity, high-resolution, and low-cost brain PET imaging.

Combination of MRI systems was also investigated. Since DOI measurement enables smaller ring diameter to obtain higher sensitivity and lower production costs, we proposed an add-on PET, which is a RF coil combined with DOI-PET detectors. In theory, the proposed birdcage coil integrated with PET detectors can be applied to any existing MRI.

Changing the chin-detector position to the neck

- More patient-friendly geometry
- 7% sensitivity improvement
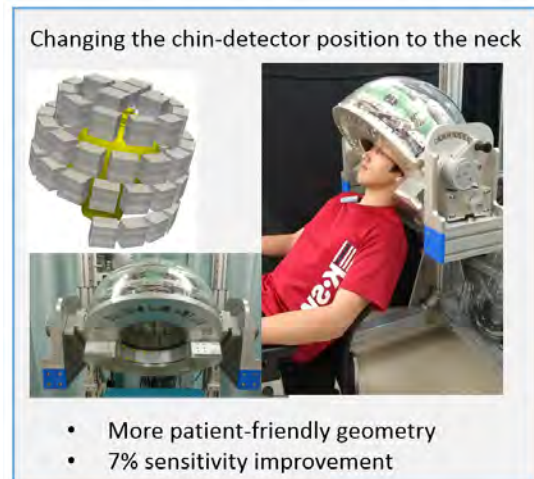
Figure 2. A brain PET prototype with hemisphere detector arrangement

4. OpenPET

OpenPET is our original idea to realize the world's first open-type 3D PET scanner for PET-image guided particle therapy such as *in situ* dose verification and direct tumor tracking. The principal of dose verification for particle therapy is based on the measurement of positron emitters which are produced through fragmentation reactions caused by proton or ^{12}C ion irradiation. Even with a full-ring geometry, the OpenPET has an open gap through which the treatment beam passes. Outstanding HIMAC experiments which made full use of the potential of the OpenPET system were done. A PET-dose conversion method was studied in collaboration with Ludwig-Maximilians-Universität München. Validation of Monte Carlo codes was investigated in collaboration with Australian Nuclear Science and Technology Organisation (ANSTO) / University of Wollongong.

Figure 3. OpenPET compared with a commercial system

References

[1]   2017ReportonPETImagingPhysicsResearch

http://www.nirs.qst.go.jp/usr/medical-imaging/ja/study/pdf/QST_R_7.pdf

Deep Learning for Nuclear Medicine

Jae Sung Lee, Donghwi Hwang, Seung Kwan Kang, JunyoungPark

[1] Department of Nuclear Medicine and Biomedical Sciences,
Seoul National University College of Medicine, Korea

Abstract

Recently, deep learning has outperformed the traditional machine learning and Bayesian approaches in many different applications such as image restoration and super-resolution with the large dataset and high computing power graphical processing unit. Furthermore, the deep learning approach apparently has great potential for providing answers to unsolved problems in medical imaging physics and engineering. In this talk, the challenges in radiation image generation and analysis and deep learning approaches to overcome these challenges will be presented.

1. Noise and artifact reduction in PET

Although positron emission tomography (PET) is highly sensitive and quantitative imaging too that provides functional, biochemical & molecular information, it suffers insufficient anatomical information, low resolution and high noise level. Some early attempts to reduce the noise level in PET images using deep learning approach will be introduced. This will be followed by recent advances in noise and artifact reduction in simultaneously reconstructed activity and attenuation images from only the emission PET [1]. These advances were achieved by training some convolutional neural networks (CNNs) that learns computed tomography (CT) derived PET attenuation maps from simultaneously reconstructed activity and attenuation data (Fig. 1).

2. Spatial normalization of amyloid PET

Accurate spatial normalization of amyloid PET images for Alzheimer's disease assessment without coregistered anatomical magnetic resonance imaging (MRI) of the same individual is technically challenging. The distinct difference in the uptake pattern of amyloid PET imaging tracers between amyloid positive and negative groups is a significant benefit in visual interpretation of the images. Therefore, performing spatial normalization of coregistered three-dimensional (3D) MRI with PET onto the MRI template and applying the same transformation parameters to the PET image is the current standard in amyloid PET image analysis. However, this process requires an additional coregistration procedure of amyloid PET and 3D MRI that is not always available. To overcome this challenge, we propose deep learning-based self-generation of PET templates for amyloid PET spatial normalization using supervised deep neural networks. In the proposed approach, deep neural networks are trained to produce the best individually adaptive PET template [2].

3. Automatic volume of interest drawing

Glomerular filtration rate (GFR), the rate at which the kidney filters the waste from the blood, is considered the most useful test to measure the level of renal function and determine the stage of kidney disease. Quantitative single photon emission tomography (SPECT)/CT is potentially useful for more accurate and reliable GFR measurement than conventional planar scintigraphy. However, manual drawing of a volume of interest (VOI) on renal parenchyma in CT images is labor-intensive and time-consuming job usually taking around 15 min per scan. How we have applied deep learning approach to the 3D segmentation of kidney parenchyma in CT for the fully automated GFR quantification will be presented (Fig. 2).
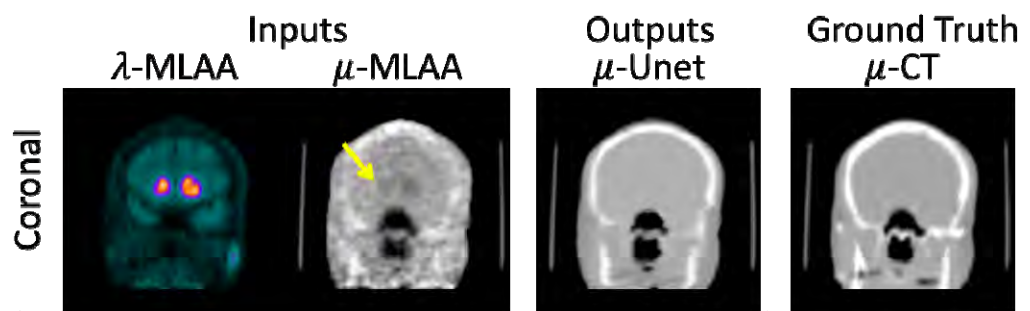
Figure 1. Comparison of CNN outputs (μ-Unet) to the μ-MLAA and μ-CT.
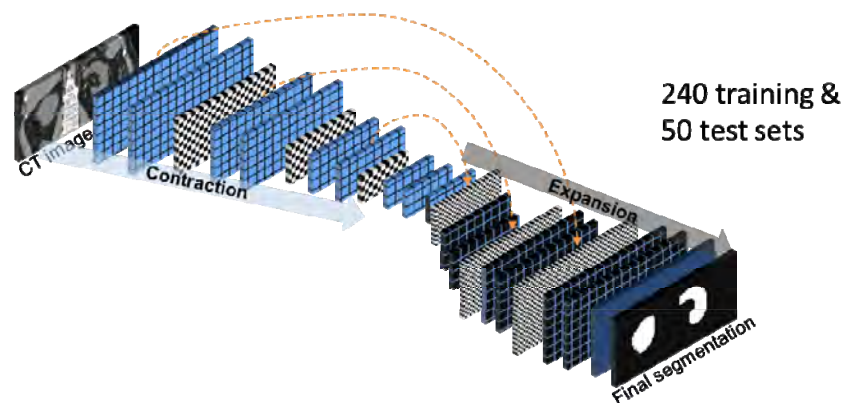
Figure 2. Deep learning network for renal parenchyma segmentation

References

[1] D. Hwang, et al. "Improving accuracy of simultaneously reconstructed activity and attenuation maps using deep learning," J. Nucl. Med. 2018. doi: 10.2967/jnumed.117.202317. [Epub ahead of print]

[2] S. K. Kang et al., "Adaptive template generation for amyloid PET using a deep learning approach," Human Brain Map. 2018 May 11. doi: 10.1002/hbm.24210. [Epub ahead of print]

[3] J. Park et al., "Computed tomography super-resolution using deep convolutional neural network," Phys. Med. Biol. 2018 Jul 16;63(14):145011.

Optical and gamma photon imaging in radiation therapy

Seiichi Yamamoto [1]

[1] University Graduate School of Medicine, Japan

Abstract

We discovered that the luminescence of water and the phenomenon was confirmed to be used for dose distribution measurements of proton therapy. Also the low energy gamma camera can be used for bremsstrahlung X-ray imaging during irradiation of proton and carbon-ion irradiations. The author will show a part of these results on optical and gamma photon imaging in radiation therapy.

1. Introduction

Measurements of dose distribution during proton therapy are important because of the dose accumulation at the target. Ionization chambers are typically used to measure dose distributions, but these measurements take a long time. To measure the dose distribution more precisely and efficiently, a new method is desired. We tried the optical method to image a water phantom during proton and carbon-ion irradiations using a high-sensitivity cooled charge coupled device (CCD) camera with lower energy than the Cerenkov-light threshold. Amazingly, we discovered a luminescence image similar to proton dose distribution in the phantom. We conducted additional experiments and obtained the evidence that this method could be used for the dose estimations at least for proton therapy. We also tried gamma photon imaging during irradiations of proton and carbon-ion to obtain the real time range estimation of these beams. We developed high and low energy gamma (X-ray) camera to image the annihilation photons from produced positrons and prompt X-rays from the secondary electrons produced by the proton and carbon-ion.

2. Methods

(1) Optical imaging in therapy

Figure 1(A) shows a schematic drawing of the experimental setup for luminescence imaging during proton irradiation. We placed a phantom on a table with the spot scanning proton therapy system (Hitachi Corporation). A cooled CCD camera operating at -10 degree C (BITRAN BS-40L, Japan) with a C-mount F-1.4 lens (Computar, Japan) was set 43 cm from the phantom surface. A photo during imaging experiments is shown in Fig. 1(B). When conducting the luminescence imaging experiments, the phantom and the CCD camera were covered with a black curtain to minimize the detection of background light by the CCD camera.
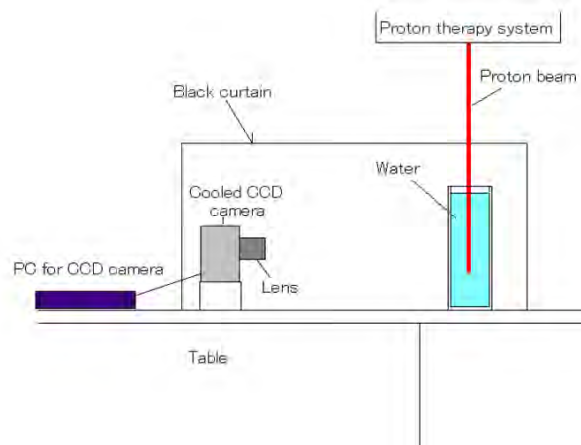
Fig. 1 Schematic drawing of experimental setup for luminescence imaging during proton irradiation

The phantom used was a transparent liquid container and the other was an acrylic block. The liquid container was made of acrylic resin plates with outer dimensions of 20 cm (horizontal) x 20 cm (vertical) x 10 cm (depth), and was 5-mm-thick. The measurements using water phantoms were to evaluate the shapes and ranges of the proton beam from the images during irradiations and compared with those measured by an ionization chamber. A 100-MeV energy proton beam was irradiated to the water phantom.

(2) Gamma photon (X-ray) imaging in therapy

Fig. 2 shows the developed X-ray camera. We used a 20 x 20 x 1 mm thick GAGG scintillator that is finely grooved in 0.2 x 0.2 mm pixels with 0.05 mm wide slits and optically coupled to a 1-inch square high quantum efficiency type position sensitive photomultiplier tube (R8900-100-C12, Hamamatsu). The thickness of tungsten container and camera head was 20 mm.
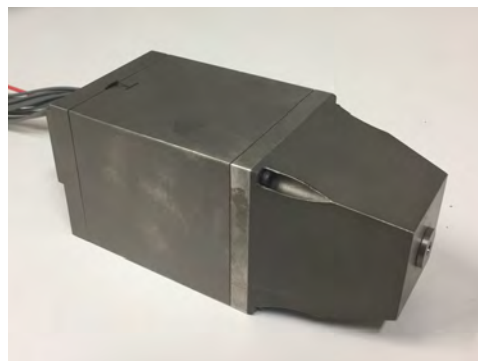
Fig. 2 Photo of developed X-ray camera

We conducted the imaging experiments of proton beams. The developed X-ray camera was set 100 cm from the water phantom (20 x 20 x 10 cm). Proton beam was irradiated to the center of the water phantom from the left side. We imaged the bremsstrahlung X-ray during proton irradiations for three different proton beam energies; 100 MeV, 139 MeV and 171 MeV. Also we image during 290MeV carbon-ion irradiation to a water phantom.

3. Results

(1) Optical imaging in therapy

Figure 3 (A) shows the optical photo of the water phantom to measure the dimension of the phantom. Figure 3 (B) shows the luminescence image of the water phantom during 100.2-MeV proton-beam irradiation from the upper direction. We were really surprised with this image because a luminescence image was obtained for proton beam lower than the Cerenkov light threshold. Figure 3 (C) shows the fused image of the luminescence image and optical photo of the water phantom. We could observe the luminescence started from the surface of the water and ended with the Bragg peak [1].

(A)   (B)   (C)
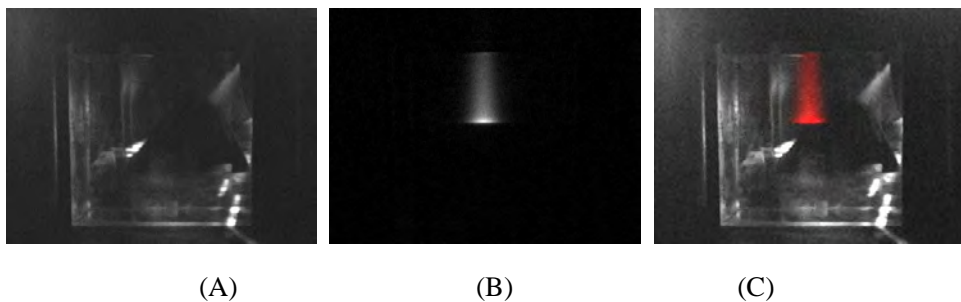
Fig. 3 Optical photo of water phantom (A), luminescence image of the water phantom during 100.2-MeV proton-beam irradiation (B), and fused image of luminescence image and optical photo (C).

The depth profile of the produced light is shown in Fig. 4 (A). The range of luminescence of water was the same as the dose, but the Bragg-peak height was smaller and the offset value was observed longer than the Bragg peak. We hypnotized that these were attributed to the prompt gamma produced Cerenkov light, and the component was calculated by simulation as shown in Fig. 4 (B). Corrected depth profile showed identical distribution to the dose as shown in Fig. 4 (C) [2].

(A)   (B)   (C)
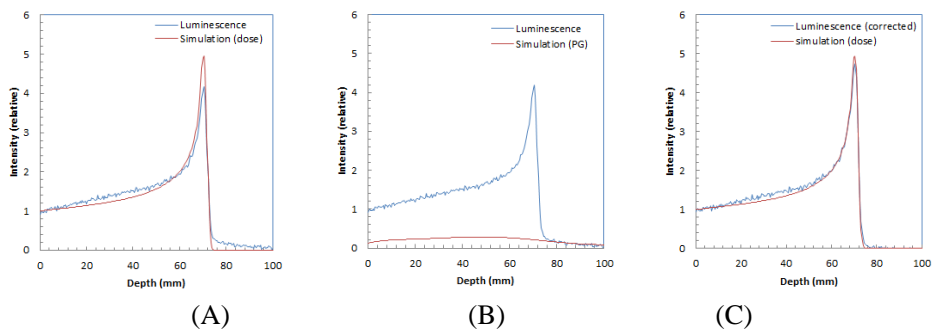
Fig. 4 Depth profile of luminescence image of the water phantom during 100.2-MeV (A), that shown with estimated prompt gamma produced Cerenkov light (B), and that subtracted prompt gamma produced Cerenkov light (C)

(2) Gamma photon (X-ray) imaging in therapy

Figure 5 shows the measured images of bremsstrahlung X-ray during 100 MeV (A), 139 MeV (B) and 171 MeV (C) proton irradiations. We could observe the prompt X-ray trajectories of the proton beams. The measured ranges were almost identical to the calculated results [3].

(A)   (B)   (C)
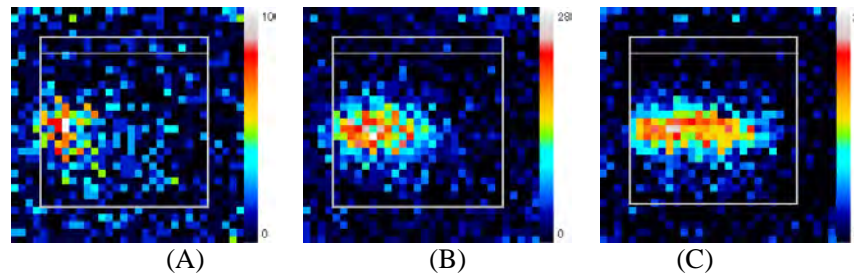
Fig. 5 Measured images of bremsstrahlung X-ray during 100 MeV (A), 139 MeV (B) and 171 MeV (C) proton irradiations. White lines in images indicate the contour of water phantom.

Figure 6 shows measured images of bremsstrahlung X-ray during 290MeV carbon-ion with 50mm range shifter (A), 25 mm range shifter (B), and without range shifter. We could obtain clear images of X-rays during irradiation of carbon-ion beams. Ranges estimated from the images were also almost identical to the calculated results [4].

(A)   (B)   (C)
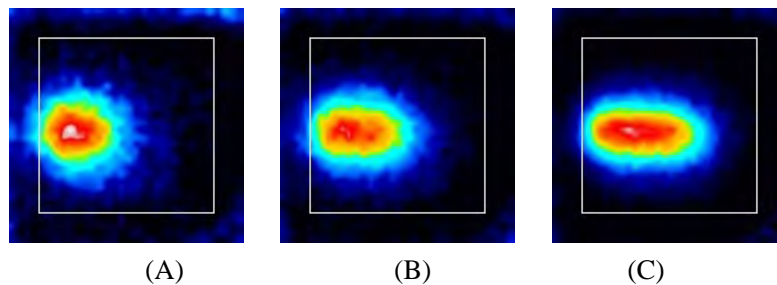
Fig. 6 Measured images of bremsstrahlung X-ray during 290MeV carbon-ion with 50mm range shifter (A), 25 mm range shifter (B), and without range shifter (C).

4. Conclusions

We confirmed that the luminescence of water can be used for dose distribution measurements of proton therapy. Low energy gamma camera can be used for bremsstrahlung X-ray imaging during irradiation of proton and carbon-ion irradiations. These new methods are promising in imaging in radiation therapy.

Acknowledgments

References

[1] S. Yamamoto, et al, Medical Physics, 42 (11), 6498-6506, 2015

[2] T. Yabe, et al., Phys. Med. Biol. 63, 04NT02, 2018

[3] K. Ando, et al., Phys. Med. Biol. 62, 5006–5020, 2017]

[4] M. Yamaguchi, et al., Phys Med Biol. 2018;63(4):045016

A feasibility study of NIR/gamma/visible multimodal laparoscopic imaging

Seong Jong Hong[1,2], Young Been Han[1], Seong Hyun Song[1], Ho Young Lee[3], and Han Gyu Kang[1*]

[1] Department of Senior Healthcare, Graduate School, Eulji University, Korea
[2] Department of Radiological Science, Eulji University, Korea
[3] Department of Nuclear Medicine, Seoul National University, Korea

Abstract

We present a feasibility study of multimodal laparoscopic imaging, for which NIR/gamma/visible images are simultaneously obtained. A miniaturized gamma detection module was fitted into a laparoscopic tube with a 12.5 mm ID. The central region of the gamma detection module was occupied by a GRIN lens for focusing NIR and visible photons. A well-separated crystal map with a ^{22}Na source and a clean visible/NIR image were obtained.

1. Introduction

In the previous study, we developed a prototype multimodal laparoscope which employed a fiber bundle to transfer scintillation photons by gamma, and visible and NIR photons to CCDs [1], [2]. In this study, the array of scintillation crystals was directly coupled to SiPMs to minimize a loss of photons by the fiber bundle and NIR/visible images were obtained using a GRIN (Gradient Index) lens at the center of the GAGG crystal array.

2. Methods

A tungsten pinhole collimator, the array of 52 GAGG crystals ($0.9 \times 0.9 \times 4$ mm^3, C&A Corporation, Japan), the array of 12 MPPC S13615-1050 and 8 S13360-2050VE SiPMs (Hamamatsu photonics, Japan), a charge division circuit board (Brightonix imaging, Korea), and the GRIN lens (GRIN tech, Germany) were fitted into a stainless steel laparoscopic tube with a 12.5 mm ID (Fig. 1). Inside a light splitting module consisted of a dichroic mirror and aspheric achromatic lenses, photons transferred through the GRIN lens were splitted into NIR and visible photons. The NIR and visible photons were subsequently detected by 2 CCD cameras (Fig. 1).

Position information was obtained by an Anger-like weighted logic (Eq. (1)) using four output signals (A, B, C and D) from the charge division board and a trigger signal was obtained by summing the four signals.

$$X = \frac{A+B-C-D}{A+B+C+D}, \quad Y = \frac{-A+B+C-D}{A+B+C+D} \tag{1}$$

The four output and trigger signals were fed into a DRS4 based high speed waveform digitizer DT5742B

(CAEN S.p.A, Italy) with a sampling rate 1 Gsa/s of DT5742.
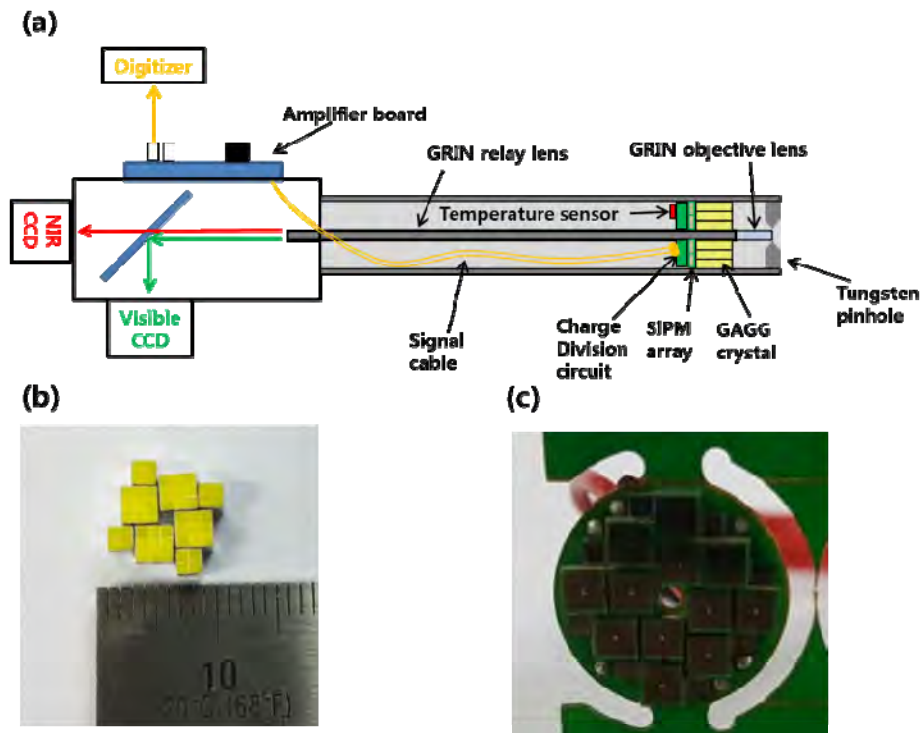
Figure 1. (a) Schematic diagram of the multimodal laparoscope system, (b) the gamma detection module, and (c) the GAGG crystal array.

3. Results

Figure 2 shows a schematic diagram of the arrays of SiPMs and GAGG crystals and a well-separated crystal map.
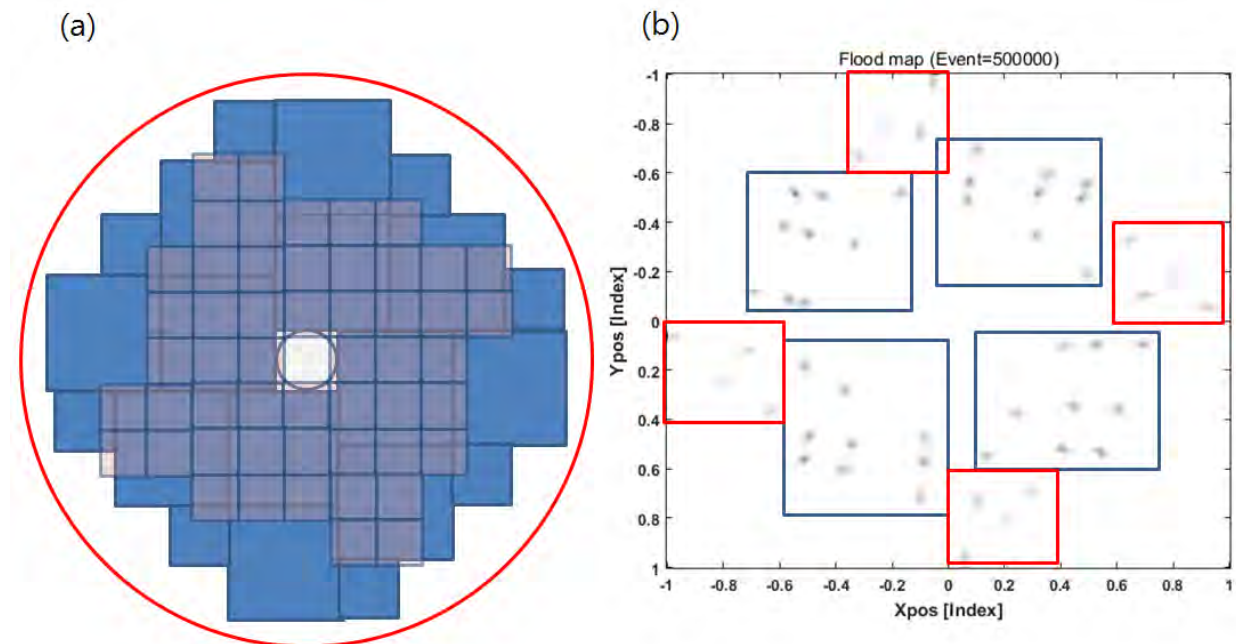
Figure 2. (a) Schematic diagram of the arrays of SiPMs (blue) and GAGG crystals (grey) and (b) the crystal map. At the center of the SiPM and crystal arrays was placed the GRIN lens.

Figure 3 shows a NIR/visible image obtained with EP tubes containing ICG fluorophore. NIR image was green pseudo-colored and overlaid on the visible image.
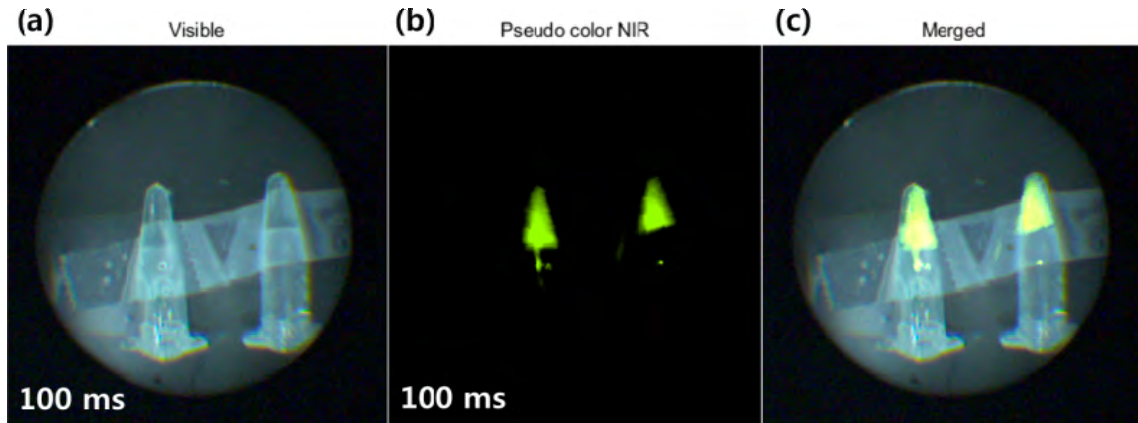
Figure 3. Simultaneous NIR/visible image: (a) the visible image of the EP-tubes containing ICG fluorophore, (b) the NIR image, and (c) the visible/NIR fusion image.

4. Conclusions

We obtained the well-separated crystal map with the ^{22}Na source and the clean visible/NIR image. Simultaneous image acquisition with a mixture of ^{99m}Tc and ICG is in progress.

Acknowledgments

References

[1]   H.G. Kang, H.Y. Lee, K.M. Kim, S.H. Song, G.C. Hong, and S.H. Hong., "A feasibility study of an integrated NIR/gamma/visible imaging system for endoscopic sentinel lymph node mapping," *Medical Physics*, vol. 44, no. 1, pp. 227-239, 2017.

[2]   H.G. Kang, S.H. Song, Y.B. Han, H.Y. Lee, K.M. Kim, and S.H. Hong., "Proof-of-concept of a multimodal laparoscope for simultaneous NIR/gamma/visible imaging using wavelength division multiplexing," *Optics Express*, vol. 26, no. 7, pp. 8325-8339, 2018.

Scintillation crystals for radiation detectors

Hiroyuki Ishibashi

Oxide Corporation, Japan

Abstract

Scintillation crystals are widely used for radiation detectors such as in PET. The scintillation crystals and features, and those crystal growth methods are reviewed.

1. Introduction

Since its discovery by Hofstadter in 1948, NaI:Tl scintillators have been widely used as detectors for radiation [1, 2]. With the development and market penetration of medical equipment such as X-ray computed tomography (X-ray CT) in 1973 [3] and positron emission tomography (PET) in 1975 [4], dense scintillator oxide crystals have been developed as alternatives to NaI:Tl. These include bismuth germinate (BGO), cadmium tungstate (CWO), cerium-doped gadolinium silicate (GSO), cerium-doped lutetium silicate (LSO) and other Lu-based scintillators (LYSO and LGSO). These scintillators have good radiation sensitivity because of their density and of their constituent elements with high atomic numbers. They are made use in nuclear and high energy physics research as well as detectors for the abovementioned medical equipment to downsize the radiation detector resulting to better image quality.

A scintillator crystal must produce luminescence from an incident radiation and serve as a guide to transfer the scintillation light efficiently to a detector such as a photomultiplier tube (PMT) or photodiode. To be able to do so, many scintillators are made from high purity single crystals with great performance because of few defects and less grain boundaries to avoid light scattering [5].

2. Properties of typical scintillators

Table 1 shows the properties of typical scintillators grown by Czochralski method compare to a standard scintillator, NaI:Tl. These scintillators are currently used as radiation detectors practically because of their density and large absorption coefficients.

In my talk, the crystal growth technology and the scintillation characteristics of these scintillation crystals are reviewed. These crystals have distinguished features and are applied to radiation detectors especially for medical equipment and high energy physics. The scintillators are mostly grown by the Czochralski method with a large diameter for practical use. Some novel scintillation crystals such as GPS will be also discussed.

Table 1.   Comparison in properties of typical scintillators

	NaI:Tl	BGO	CWO	GSO	LSO	LYSO	LGSO	GPS
Density (g/cm^3)	3.67	7.13	7.9	6.71	7.4	7.2	7.3	5.5
Effective Atomic Number Z_{eff}	50	75.2	64.2	58	63	63	63	-
Emission Wavelength λ_{em} (nm)	415	480	470	430	410	410	410	400
Light Output (relative)	100	12	～35	20	~90	~90	~90	~140
Decay Time (ns)	230	300	5,000	35～70	41	41	41	50-130
Energy Resolution (% at 662keV)	7	~12	-	8-10	~8	~8	~8	5-7
Refractive Index	1.85	2.15	2.2	1.85	1.83	1.83	1.83	-
Hygroscopicity	Yes	No	No	No	No	No	No	No
Radioactivity	No	No	No	No	Yes	Yes	Yes	No
Growth Method	VB	VB CZ	CZ	CZ	CZ	CZ	CZ	CZ, DCCZ
Melting Point (ºC)	651	1050	1272	1950	2150	2100	2100	1700

References

[1]   R. Hofstadter, Phy. Rev., 74 (1948) 100

[2]   R. Hofstadter, Phy. Rev., 75 (1949) 796

[3]   G. N. Hounsfield, Brit. J. Radiol., 46 (1973) 1016

[4]   M. M. Ter-Pogossian, M. E. Phelps. E. J. Hoffman and N. A. Mullani, Radiology, 114 (1975) 89

[5]   M. Ishii and M. Kobayashi, Prog. Crystal Growth and Charact., 23 (1991) 245

Preliminary study on gamma imaging camera for BNCT

Kyeong Min Kim[1], Minho Kim[1,2], Jae Keon Bae[1] and Wonho Lee[2]

[1] Radiation devices research team, Division of Applied RI, Korea Institute of Radiological and Medical Sciences, Korea

[2] School of Health and Environmental Science, Korea University, Korea

Abstract

Boron Neutron Capture Therapy (BNCT) is a well-known methodology of cancer therapy using alpha radiation emitted from the neutron capture reaction with boron. In BNCT, prompt gamma rays of 478 keV is generated and has been studied for monitoring tools of treatment. In this study, we suggest an approach of scintillator-based prompt gamma ray imaging using Monte-Carlo simulation.

1. Introduction

BNCT is a method of cancer therapy using high reaction of neutron and boron. When neutrons are captured to boron labeled in tumor localizing drug, activated Li-7 and alpha particles are produced with the prompt gamma rays of 478 keV[1]. These prompt gamma rays can be utilized in imaging of tumor regions in treatment. However, because of 511 keV annihilation gamma rays generated by high energy (2.32 MeV) gamma rays, it is hard to get imaging with prompt gamma rays only. There have been many studies about prompt gamma imaging (PGI) in BNCT[2], in which CZT or CdTe semiconductor has been mainly considered rather than scintillator-based camera, because of high energy resolution of semiconductor detector. New developed scintillator can be an alternative solution for PGI camera overcoming the limitations of high-cost and low high energy sensitivity of semiconductor detector.

2. Methods

GATE (v7.0) package was used in Monte-Carlo simulation of gamma ray generation and imaging camera imaging. In the simulation, the size of detector FOV of gamma camera was set to 200×200 mm^2. The scintillator of detector was selected to GAGG crystal[3] with 20 mm depth and energy resolution of 6.2 % at 662 keV. Parallel-hole shape collimator was designed with 3 types of penetration fractions (5, 0.1 and 0.01 %).

In the simulation of realization of prompt gamma ray, QGSP_BIC_HP_EMZ physics list used. Several neutron energies of 0.025, 0.05, 0.1 and 10 eV are selected in the verification of neutron stop range in water. For imaging acquisition, a water-filled spherical phantom was position in the center of FOV and a boron sphere of 10 mm diameter was positioned to the center of water phantom. With changing the diameter of water phantom from 10 to 50 mm, we checked the change of prompt gamma image performance using line-profile.

3. Results & Discussion

The higher neutron energy, the greater the neutron stop range in water. From this result, we could verify the mechanism of gamma ray generation by reaction of neutron boron.
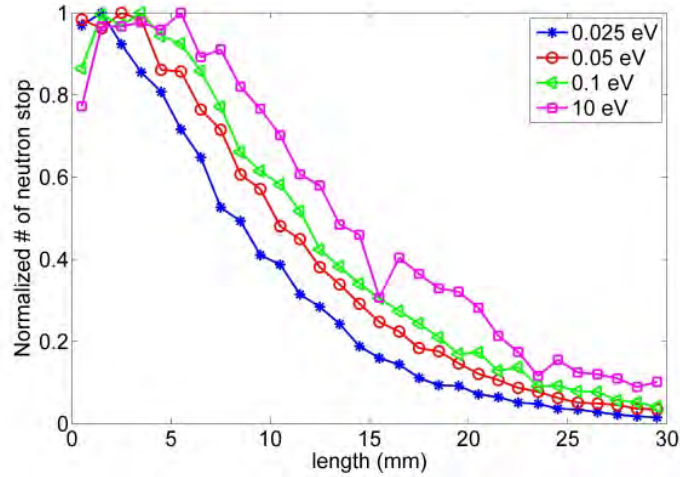
Figure 1. Normalized neutron stop range in water phantom due to neutron energy

As the amount of scattering material increased, image quality was degraded by the components of scatter and 511 keV annihilation gamma photons. Penetration fraction affect image quality significantly. Lower value of penetration faction is desirable for better imaging, but the level of 5%, which has been generally accepted for gamma camera of nuclear medicine imaging, can be considered to PGI camera for differentiation of tumor region in BNCT.
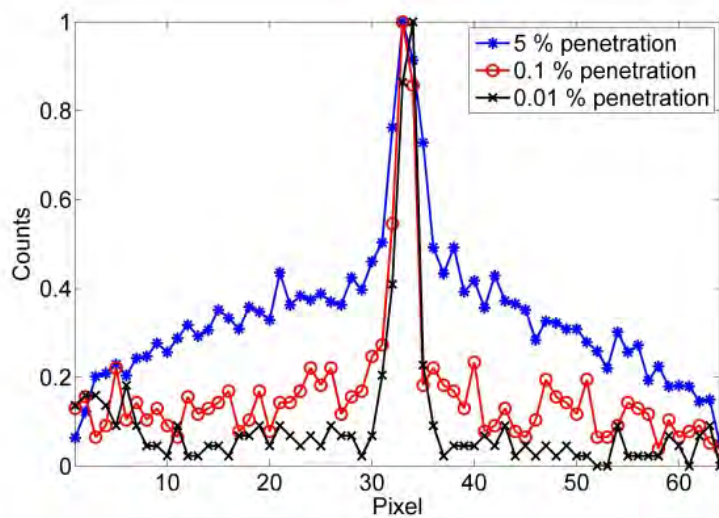
Figure 2. Changes of line profiles shape of boron sphere with the increase of penetration fraction. Boron sphere in water phantom with 15 mm diameter.
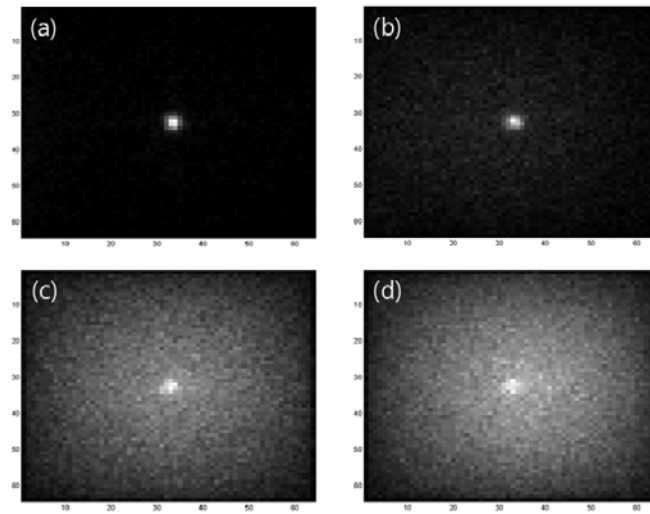
Figure 3. Prompt gamma images of different sized water phantom. Penetration fraction of 5% was assumed. (a) 10 mm, (b) 20 mm, (3) 40 mm, and (d) 50 mm diameter

4. Conclusion

These results show the possibility of PGI camera based on scintillator with lower energy resolution, compared to CZT or CdTe. Additional considerations to minimize the amount of scatter and penetrated photons should be essential in PGI imaging of BNCT.

Acknowledgments

References

[1]   S. Savolainen, M. Kortesniemi, M. Timonen, et al., "Boron neutron capture therapy (BNCT) in Finland: Technological and physical prospects after 20 years of experiences," Physica Medica, 29, pp.233-248, 2013.

[2]   T. Kobayashia, Y. Sakurai, "A noninvasive dose estimation system for clinical BNCT based on PG-SPECT — Conceptual study and fundamental experiments using HPGe and CdTe semiconductor detectors," Med. Phys., 27, pp.2124-2132, 2000.

[3]   J. Iwanowska, L. Swiderski, T. Szczesniak, et al., "Performance of cerium-doped $Gd_3Al_2Ga_3O_{12}$ (GAGG:Ce) scintillator in gamma-ray spectrometry," Nucl. Instrum. Methods Phys. Res. A, 712, pp.34-40, 2013.

How to overcome PET drawbacks?

Hiroshi Watabe[1]

[1] Cyclotron and Radioisotope Center, Tohoku University, Japan

Abstract

Positron emission tomography (PET) is an imaging technology to visualize distribution of particular ligand inside living organisms from rodent to human. PET has ultra high sensitivity and quantitativity, and is considered the de facto standard for molecular imaging. However, PET has several drawbacks, such as limited spatial resolution, and high cost. In this paper, the author focused the drawbacks of PET, and discussed how to overcome these drawbacks.

1. Introduction

The principle of positron emission tomography (PET) is simultaneously detecting annihilation photons and determining the position of positron-emitter. Since Wrenn et al. proposed to utilize positron-emitting radioisotopes for the localization of brain tumors in 1951[1], instrumentation of PET has been evolved by many researchers, and nowadays, PET is considered the most sensitive and specific molecular imaging modality. However, up to now there are still some drawbacks of PET. In this paper, I describes some drawbacks we still face for PET, and challenges to overcome these drawbacks.

2. Spatial resolution

The limited spatial resolution is one of the most notable drawbacks of PET. Even the most advanced clinical PET scanner cannot achieve less than 4 mm full width at half maximum (FWHM)[2], while X-ray CT or MRI scanners can easily have less than 1 mm FWHM. There are several reasons for the degradation of spatial resolution, such as positron range, acollinearity and limited size of detector, and these causes are considered fundamental. One can reduce the detector size which results in the improvement of the spatial resolution, however, the number of the detector must be tremendously increased, and it is economically unrealistic. Software-based approaches are attractive because no additional hardware is required to improve spatial resolution. Two categories of the software-based approaches exist. One is the resolution recovery during image reconstruction[3], and the other is post process after image reconstruction. The former utilizes point-spread function (PSF) for each line-of-response (LOR), which is obtained empirically or by computer simulation. The latter is often called ’partial volume correction’ (PVC) and spatial resolution is improved by modeling the reference image with high spatial resolution, such as MRI. Several PVC methods[4] have been proposed by researchers. Either software-based approaches rely on some assumptions, and there is no guarantee the final image is correct.

3. **Temporal resolution**

The unavoidable enemy in PET is noise, which is driven by the observed individual event of annihilation 511 keV photon. Therefore, in order to preserve good statistics of voxel counts in PET image, it is necessary to collect data for certain time, and temporal resolution of PET system is limited. The minimum frame duration for conventional PET scanner is more or less three seconds. On the other hand, synapse in neuron transmits signal within less than 100 milliseconds, and PET cannot observe the transmission of the single signal. By increasing amount of injected radioactivity, count statistics will be better. But, random events detected by PET scanner are also increased, and count statistics reach saturation. Also, it must be aware that as the dosage of injected radioactivity increases the amount of radiation exposure to the subject increases. Time-of-flight (TOF) PET[5] has potential to dramatically improve the temporal resolution. The ultimate PET scanner is to image by every-by-event by means of TOF technology. But to realize such a scanner, scintillation crystal with ultra short decay time and ultra-fast electric circuit must be invented, and we are not ready for the dream PET scanner.

4. **Cost**

The equipment of PET scanner itself is very expensive to taking account of the cost, not only PET scanner itself but total system of PET study must be considered. Simon et al.[6] proposed the total body PET (TB-PET) scanner which has two meter in axial length. Obviously the cost of TB-PET scanner is extravagant. They claim the ultra-high sensitivity of TB-PET scanner results in the great economical benefit due to the highest patient throughput. The cost of PET study include the development of PET tracer. So far, only [F-18]FDG is commercially successful PET tracer, and most PET tracers employed are research purpose only. If a new PET tracer has impact beyond [F-18]FDG, a PET scanner is more popular than now and the cost of PET scanner could be reduced. The development of a new PET tracer takes long period and is very costly. During the drug development, thousands of candidates of compounds exist, and only a few compounds go to clinical trial and the success rate in the clinical trial is very low. To speed up this screening process, we have developed index to judge clinical usefulness of candidate PET tracer.[7] .

5. **Conclusion**

In this paper, drawbacks of PET, namely, spatial resolution, temporal resolution, and cost are described and some challenges to overcome these drawbacks are introduced. There are still some spaces to improve the performance of PET, and future PET scanner is eagerly waited.

References

[1] F.R. Wrenn, M.L. Good, P. Handler,"The use of positron-emitting radioisotopes for the localization of brain tumors",Science,113,pp.525‑527,1951..

[2] A.M. Grant, T.W. Deller, M.M. Khalighi, et al.,"NEMA NU 2-2012 performance studies for the SiPM-based ToF-PET component of the GE SIGNA PET/MR system",Med Phys,43,pp.2334‑2343,2016.

[3] A. Rahmim, J. Qi, V. Sossi,"Resolution modeling in PET imaging: theory, practice, benefits, and pitfalls.",Med Phys,40,pp.064301,2013.

[4] M. Shidahara, B.A. Thomas, N. Okamura, et al.,"A comparison of five partial volume correction methods for tau and amyloid PET imaging with [(18)F]THK5351 and [(11)C]PIB.",Ann Nucl Med,31,pp.563‑569,2017.

[5] S. Surti, J.S. Karp,"Advances in time-of-flight PET",Physica Medica,32,pp.12‑22,2016.

[6] S.R. Cherry, R.D. Badawi, J.S. Karp, et al.,"Total-body imaging: Transforming the role of positron emission tomography",Sci Trans Med,9,pp.eaaf6169,2017.

[7] Y.H. Nai, M. Shidahara, C. Seki, et al.,"Biomathematical screening of amyloid radiotracers with clinical usefulness index",Alz Dementia: Trans Res Clin Intervent,3,pp.542‑52,2017

Neuroreceptor PET quantification with reduced scan

Seongho Seo[1,2] and Jae Sung Lee[3,4,5]

[1]Department of Neuroscience, College of Medicine, Gachon University, Incheon, Korea

[2]Neuroscience Research Institute, Gachon University, Incheon, Korea

[3]Department of Biomedical Sciences, Seoul National University College of Medicine, Seoul, Korea

[4]Department of Nuclear Medicine, Seoul National University College of Medicine, Seoul, Korea

[5]Institute of Radiation Medicine, Medical Research Center, Seoul National University, Seoul, Korea

Abstract

A long scan duration in quantitative analysis of dynamic neuroreceptor PET is a challenge for clinical applications. We examined a reduction of scan duration for the quantification of slow kinetic tracers using a newly developed linearized full reference tissue model that has no restriction on the selection of data point required for model fitting. We performed a computer simulation using the kinetic parameters of [18F]FP-CIT PET in human brain.

1. Introduction

Dynamic PET imaging can accurately capture the temporally changing spatial distribution of the radioligand in the brain, which reflects the targeted receptor's density and dynamic interaction with the radioligand; the techniques of tracer kinetic modeling refine the enriched information from dynamic imaging into quantitative parameters that characterize the receptor distribution and the binding process in the brain [1,2]. However, the acquisition and analysis of dynamic PET data typically requires a long-lasting scan that remains a main obstacle for their wide clinical application in terms of patient throughput and comfort [2,3]. Thus, before a clinical application of radiotracer of interest, a minimal scan duration for the best-fitted kinetic model or an equivalent semi-quantitative method based on static imaging is often investigated [4,5].

The challenge of long scan duration becomes more prominent in PET studies with slow-kinetic tracers. Since those tracers commonly experience delayed equilibrium relative to the input function or one between the free and specifically bound compartments, standard methods for neuroreceptor PET quantification may suffer from some issues. For instance, the simplified reference tissue model (SRTM) leads to biased parameter estimation due to a violation of instantaneous equilibrium assumption [5-7]. Although some linear models closely associated with the SRTM is free from instantaneous equilibrium assumption, they rely on limited number of late-phase data points [6], hindering an early termination of dynamic scan.

Recently, a new linearized full reference tissue model (LFRTM) has been devised [7], which uses a full range of dynamic data without requiring instantaneous equilibrium. In this preliminary study, we investigated the feasibility of shortening scan duration when applying this model to the quantification of PET study with slow kinetic tracers such as [18F]FP-CIT.

2. Methods

2.1 Model equations

For the quantification of neuroreceptor PET, we evaluated the basis-function-based implementation of the LFRTM for varying scan durations:

$$C_T(t) = R_1 C_R(t) + k_2 \left(\int_0^t C_R(s)ds - C_T(t) \otimes e^{-k_4 \frac{k_2}{k_{2a}} t} \right) - k_{2a} \left(\int_0^t C_T(s)ds - C_T(t) \otimes e^{-k_4 \frac{k_2}{k_{2a}} t} \right),$$

where $C_T(t)$ and $C_R(t)$ are the tracer concentrations (kBq/mL) at the post-injection time t (min) in the target tissue and reference tissue region, respectively, and R_1 is a target-to-reference ratio of the rate constant for a delivery of radiotracer from arterial plasma to tissue; k_2 (min^{-1}) is a rate constant for its efflux from tissue; and k_{2a} (min^{-1}), given as $k_2/(1+k_3/k_4)$, denotes the apparent efflux rate constant from tissue when the tissue region become approximately described with one compartment after equilibrium within tissue. The rate constants k_3 and k_4 (min^{-1}) are for the binding and release from the neuroreceptor. We iteratively generated a set of basis functions for the convolution term using different k_4 values, predefined between 0.005 and 0.05 (min^{-1}), and updated the values of k_2 and k_{2a} in the basis functions from those estimated at the previous iteration step. To investigate the feasibility of a shorter dynamic PET scan for neuroreceptor PET quantification, we also tested the reduced models of the LFRTM, in which the set of kinetic parameters involved was reduced from (R_1,k_2,k_{2a},k_4) to (R_1,k_2,k_3), (R_1,k_2), and (R_1) (LRTM-3P, LRTM-2P, and LRTM-1P, respectively).

2.2 Computer simulations

We performed a preliminary simulation study to evaluate each model's goodness-of-fit in different scan termination times (t_{end}) from 90 min to 60, 30, 20, and 10 min. We generated 90-min noiseless tissue (striatum) and reference (cerebellum) TACs of [18F]FP-CIT using a metabolite-corrected plasma input function and reversible two-tissue compartmental model (2TCM) parameters given from previous studies [5,6]; we assumed an ideal reference region whose tissue kinetic follows one-tissue compartment model.

3. Results

The preliminary results revealed that the LFRTM showed good fit for all t_{end} values but parameter estimates' accuracies were different from each other. The k_4 estimate changes largely for $t_{end} \leq 60$ (min) and k_{2a} for $t_{end} \leq 20$ while the estimates of R_1 and k_2 are stable even for $t_{end} = 10$. On the other hand, the reduced models demonstrated good fits only for the cases of reduced scan protocols: LRTM-3P for $t_{end} \leq 30$; LRTM-2P for $t_{end} \leq 20$; and LRTM-1P for $t_{end} < 10$. Their resulting parameter estimates showed good accuracies except for each model's last parameter; Estimates of k_3 in LRTM-3P and k_2 in LRTM-2P varies depending on t_{end} despite of good fit, and R_1 of LRTM-1P was slightly biased even for $t_{end} = 10$.
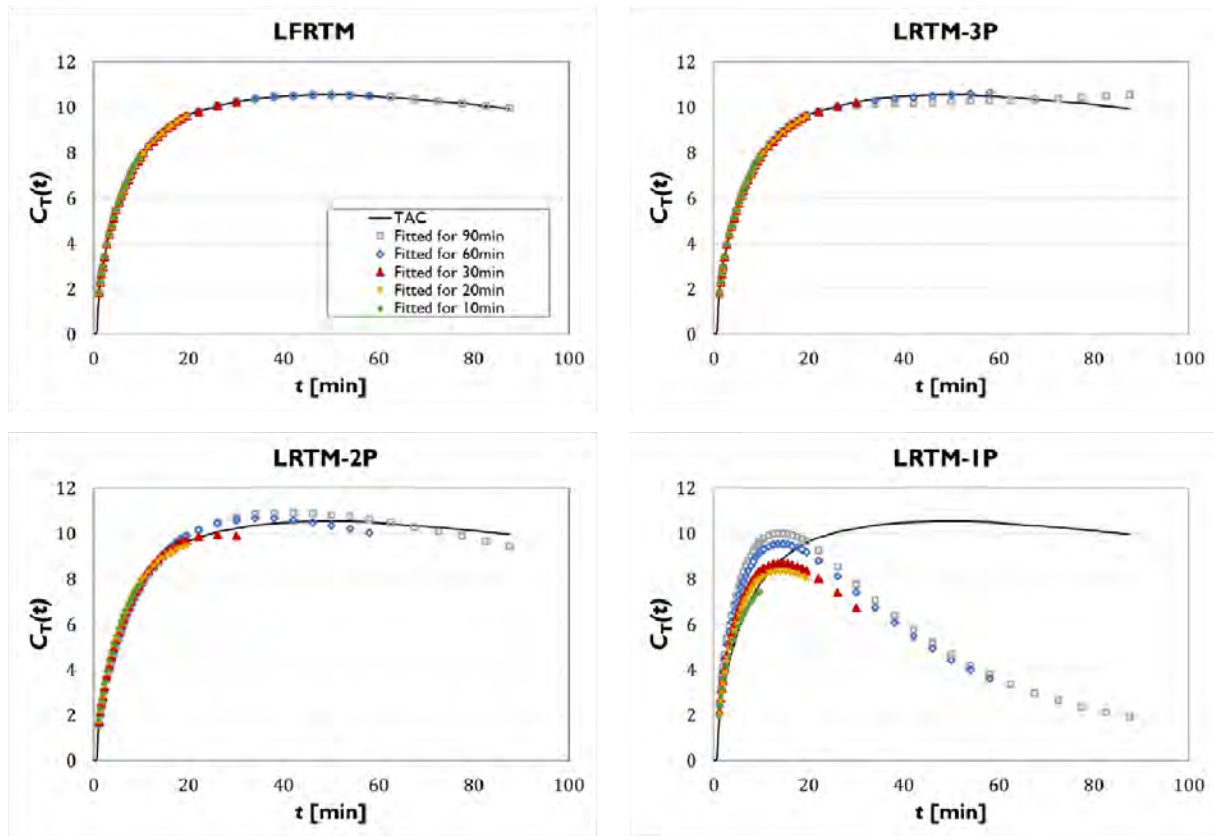
Figure 1. Fit of different models to simulated time-activity curve (TAC) with various scan durations.

4. Discussion

We preliminarily evaluated the use of short scan protocol in the quantification of slow tracer kinetics using the LFRTM and its reduced models. Depending on the scan end time, there were limitations on estimating all parameters stably even in the reduced model, requiring researcher to seek for additional regularization or to focus only on specific parameters that can be stably provided by each model. The finding should be further validated using more comprehensive simulation and clinical data in future, and statistical properties of each model should be explored.

Acknowledgments

References

[1] S. Seo, S. J. Kim, D. S. Lee, *et al.*, "Recent advances in parametric neuroreceptor mapping with dynamic PET: basic concepts and graphical analyses," *Neurosci. Bull.*, 30(5), pp. 733–754, 2014.

[2] A. A. Lammertsma, "Forward to the Past: The Case for Quantitative PET Imaging," *J. Nucl. Med.*, 58(7), pp. 1019–1024, 2017.

[3] N. A. Karakatsanis, M. A. Lodge, M. E. Casey, *et al.,* "Impact of acquisition time-window on clinical whole-body PET parametric imaging," in 2014 IEEE Nuclear Science Symposium and Medical Imaging Conference (NSS/MIC), 2014, pp. 1–8.

[4] G. Warnock, M. Sommerauer, L. Mu, et al., "A first-in-man PET study of [^{18}F]PSS232, a fluorinated ABP688 derivative for imaging metabotropic glutamate receptor subtype 5," *Eur. J. Nucl. Med. Mol. Imaging*, 45(6), pp. 1041–1051, 2018.

[5] M. Yaqub, R. Boellaard, B. N. M. van Berckel, *et al.*, "Quantification of dopamine transporter binding using [^{18}F]FP-β-CIT and positron emission tomography," *J. Cereb. Blood Flow Metab.*, 27, pp.1397–406, 2007.

[6] S. Seo, S. J. Kim, H. B. Yoo, *et al.*, "Noninvasive bi-graphical analysis for the quantification of slowly reversible radioligand binding," *Phys. Med. Biol.*, 61(18), pp. 6770–6790, 2016.

[7] J. B. Mandeville, C. Y. M. Sander, H.-Y. Wey, et al., "A regularized full reference tissue model for PET neuroreceptor mapping," *NeuroImage*, 139, pp. 405–414, 2016.

Nuclear medicine imaging in central nervous system diseases

Miwako Takahashi

National Institute of Radiological Sciences (NIRS-QST), Japan

Abstract

Nuclear medicine (NM) images are useful for decision-making of patient management as well as just for diagnosis. Among central nervous system (CNS) diseases, epilepsy, brain tumor and dementia have been intensively addressed by brain SPECT and PET imaging. In this paper, how to analyze NM images and what limitations to be overcome by NM technologies are discussed.

1. Epilepsy

Epileptic seizure is considered to be caused by the excessive, hypersynchronous discharge of neurons, while the fundamental pathophysiology has not been elucidated. In about 80% of patients with epilepsy, seizures are controlled with anti-epileptic drugs (AEDs), but in the remains, seizures cannot be controlled even after trying almost all available AEDs. Surgical treatment is the final option for obtaining seizure control. It is important for us to identify who would become seizure-free after surgery. It should be noted that 1) seizure is actually due to neuronal abnormal discharges, not psychogenic causes; 2) epileptic focus is localized to area to be safely resected or transected by surgery. Recently surgical treatment for mesial temporal lobe epilepsy (mTLE) has been confirmed to be effective rather than the prolonged AEDs therapy. Therefore, an analysis method using FDG-PET was developed for identifying patients who would become seizure-free after mTLE surgery. In the proposed method, severity of hypometabolism and laterality of them were calculated by statistical analysis using asymmetry index [1]. As a result, severe hypometabolism restricted to the unilateral temporal lobe, with ipsilateral dominant hypometabolism, even if slight decreases, may support the existence of an epileptogenic focus in the unilateral temporal lobe and a favorable seizure outcome after mTLE surgery (Figure 1) [2].
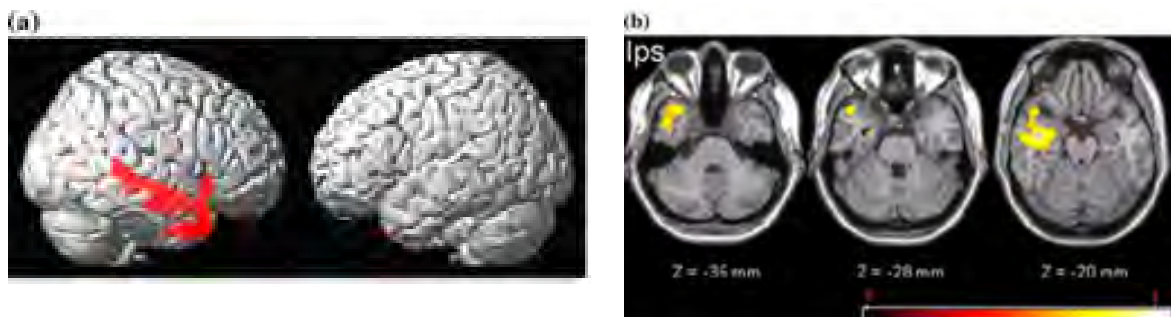

Figure 1 The characteristic distribution of hypometabolism in the seizure-free group (n=17) as compared to the controls. (Revise of reference 2): (a) surface view and (b) transaxial view.

2. Brain tumor

On management of patients with brain tumor, the timing and the area of surgical intervention are critical. The timing is decided by the tumor malignancy: the role of NM imaging is to provide the grade of malignancy in preoperative state and the extent of tumor. Even within the tumor, the most malignant area should also be identified. FDG-PET and MET-PET have been the most effective PET examinations for evaluating brain tumors. They provide the metabolic index for the grade. First, a group at University of Tokyo (Dr Toshimitsu Momose and the author) tried to determine the voxels corresponding to the normal cortex as reference (Figure 2), which used for the calculation of metabolic index [3]. Secondly, the group identified the most effective index among various indices according to 2016 WHO classification. Then, in order to improve the accuracy in deterring malignant grade, the group analyzed the metabolic pattern not only for the tumor core but also the surrounding metabolic changes where tumor cells potentially infiltrate (in submission).
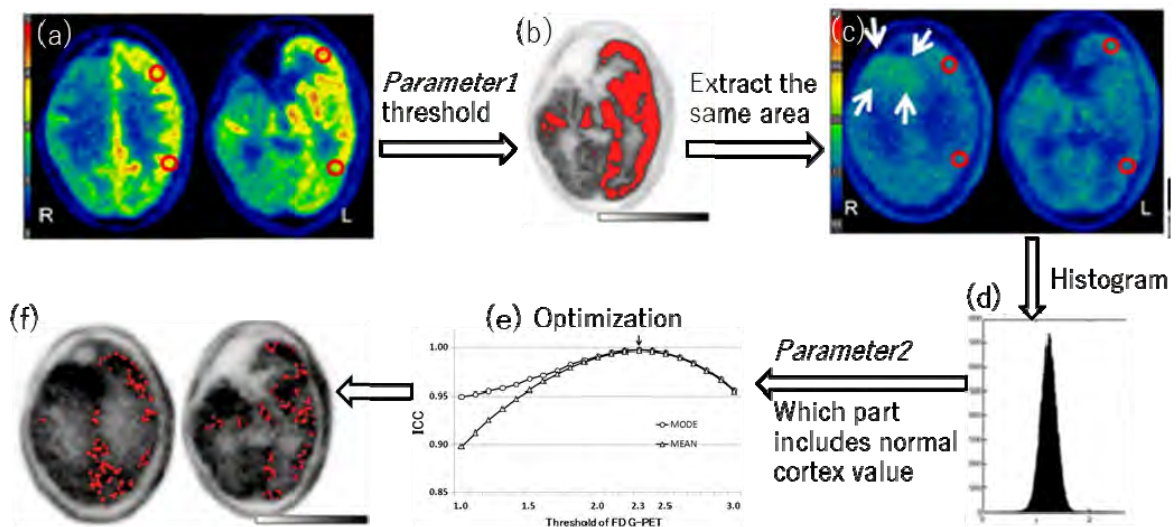
Figure 2 **On FDG-PET (a) and on MET-PET (c),** ROIs are manually placed (*red circles*) at the centrum semiovale level and at the striatum level. Brain tumor is not distinctive on FDG-PET but can be somewhat visualized on MET-PET (*arrows*). (b)The proposed method extract voxels over a threshold (parameter1), and apply the same coordination to MET-PET, and put their voxel-value into a histogram (**d**). Determine the part of the histogram include normal cortex value, mode or mean (parameter2). (e)Optimization of parameters. (f)Selected voxels are shown in *red*.

3. Dementia

NM images now available in Japan for the management of patients with dementia include rCBF-SPECT, ^{123}I-MIBG, ^{123}I-FP-CIT SPECT, FDG-PET and Amyloid PET. For patients with dementia, rCBF-SPECT has an important role for estimating the underlying degenerative disease and severity and brain area of neuronal impairments (FDG-PET is more useful, but is not covered by Japanese national insurance). To clear the usefulness of rCBF-SPECT in prediction of underlying pathology, the same group investigated the

correlation of hypoperfusion pattern on rCBF-SPECT and amyloid-PET results, namely Aβ+ or Aβ-, in patients who complain of memory disturbance. As a result, all four patients with typical AD pattern on rCBF-SPECT can reflect Aβ+, but among the other nine patients without typical AD pattern on rCBF-SPECT, four were Aβ+. Patients who do not exhibit typical AD pattern on rCBF-SPECT may have a benefit from amyloid-PET for more precise diagnosis (paper in revision).

4. Cerebral FDG distribution in healthy volunteers with jPET

Physiological distribution of FDG uptake in the brain is needed to find abnormality and analyze the NM images in patients with CNS diseases. With the use of appropriate depth-of-interaction (DOI) detectors, degradation of spatial resolution at the peripheral region, which is often seen in compact PET systems, could be eliminated. Therefore the Imaging Physics Team at NIRS developed the jPET-D4, which is a brain prototype PET with 4-layer DOI detectors. The author compared the brain FDG-PET data of healthy volunteers each obtained by a non-DOI PET scanner (HR+) and a DOI-PET scanner (jPET-D4). In visual inspection, the mesial temporal area and the dentate nucleus of the cerebellar were depicted clearer in jPET-D4 than in HR+ (Figure 3). In the ROI analysis, the region-to-cerebellum ratios of the frontal lobe and the parietal lobe were slightly lower in jPET-D4 than in HR+ (1.33 vs. 1.47, 1.09 vs. 1.29, respectively). The mesial temporal area was slightly higher in jPET-D4 than in HR+ (1.06 vs. 0.95). Other areas, such as the occipital, striatum and lateral temporal area did not show significant difference. More precise standard data of human brain will be helpful for progressing brain science as well as for evaluation of various neurological diseases.
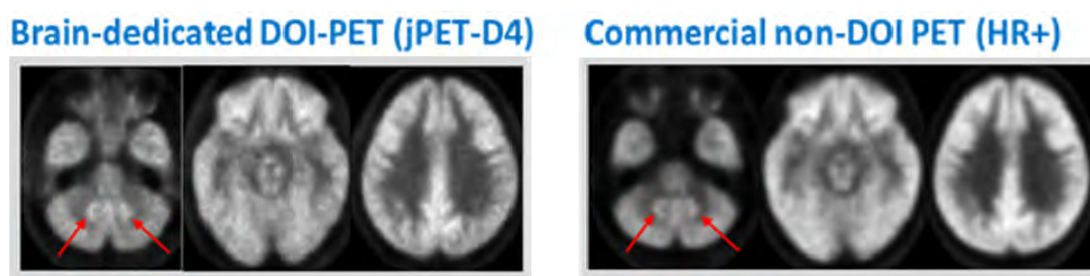
Figure 3 The dentate nucleus (*red arrow*) is identified clearer in jPET-D4. The second slice from the left includes the mesial temporal area, which is depicted more apparently in jPET-D4.

5. Future perspectives

(1) Epilepsy

Clinical routine protocol for brain FDG-PET is the integral images obtained from 45 to 55 min after FDG injection, but during the time between FDG injection and scan completed, neuronal electrical activities could be fluctuated, both of raising and inhibited within and around epileptic focus. Monitoring with electroencephalogram (EEG) around the time of FDG-PET study would improve the interpretation of brain FDG-PET.

(2) Brain tumor

Most of brain tumors cannot be cure, therefore, residual tumor or recurrence is inevitable. During follow-up, the most effective intensity and timing of anti-tumor treatment remain to be clarified. FDG-PET and MET-PET are partly helpful for evaluation of recurrence, but metabolism is modified by treatment intervention or sparse infiltration is affected by partial volume effect on PET images.

While various biological sciences are investigating brain tumor, the author believes that the precise localization on NM images where tumor sample obtained by surgery may contribute to clarify the correlation of biological information such as pathological, immunological and genetical changes, and PET and SPECT tracers, which contribute the understanding of biological features of brain tumors.

(3) Dementia

Patients with cognitive impairment, especially elderly people, are sometimes difficult to keep supine position in SPECT or PET scanner. This problem are due to not only just physical deformities, but also difficulties to understand the situation or their embarrassment. The helmet-type PET which is under development at NIRS may be helpful for these people to feel relaxed for undergoing PET examinations.

6. Conclusions

Setting a clear aim of interpretation of NM images and appropriate mathematical analytic approaches based on deep understanding of NM techniques are especially important to extract findings enough from NM images. These findings will lead the development of NM technologies and in turn, NM technologies can provide more precise data for development of neuroscience.

Acknowledgments

References

[1] Soma T, Momose T, Takahashi M, Koyama K, Kawai K, Murase K. Usefulness of extent analysis for statistical parametric mapping with asymmetry index using inter-ictal FDG-PET in mesial temporal lobe epilepsy. *Ann Nucl Med.* 2012;26(4):319-26.

[2] Takahashi M, Soma T, Kawai K, Koyama K, Ohtomo K, Momose T. Voxel-based comparison of preoperative FDG-PET between mesial temporal lobe epilepsy patients with and without postoperative seizure-free outcomes. *Ann Nucl Med.* 2012;26(9):698-706.

[3] Takahashi M, Soma T, Mukasa A, Koyama K, Arai T, Momose T. An automated voxel-based method for calculating the reference value for a brain tumour metabolic index using 18F-FDG-PET and 11C-methionine PET. *Ann Nucl Med.* 2017;31(3):250-259.

Wavelength Discrimination (WLD) Phoswich Detectors for Nuclear Medicine

Muhammad Nasir Ullah[1], Jinho Park[1], Eva Pratiwi[1], Chansun Park[1], Chanho Kim[1], and Jung-Yeol Yeom[1,2]

[1] *Department of Bio-Convergence Engineering, Korea University, Seoul, South Korea*
[2] *School of Biomedical Engineering, Korea University, Seoul, South Korea*

Abstract

In this paper, we propose a new wavelength discrimination (WLD) phoswich detector for real-time radiation discrimination in a mixed radiation field of positron (β+) and gamma (γ) radiation for use as an intraoperative positron probe. The method exploits scintillators' emission wavelength property, in place of the conventional pulse shape discrimination (PSD) approach. The advantage of this method is in its simple readout and yet accurate measurement. Experimental results confirm that we can achieve an excellent gamma rejection rejection ratio of 99.97% for the positron probe, and this method can be applied to acquire the depth-of-interaction (DOI) information in a positron emission tomography (PET) detector.

1. Introduction

Discrimination of radiation types in a mixed radiation field such as beta (β) and gamma (γ) is need to improve the performance of the positron probe in nuclear medicine. On the other hand, depth-of-interaction (DOI) detector for positron emission tomography (PET) allows a more uniform spatial resolution acroos the field-of-view in a positron emission tomography scanner.

Pulse shape discrimination (PSD) is a widely used technique for such purposes but requires fast front-end electronics to capture the raw signal waveforms and complex back-end processing system. In this presentation, we propose an accurate yet cost-effective solution for real-time positron-gamma discrimination in a mixed radiation field, and which can be used for DOI information in PET detectors. Scintillation crystals used in radiation detectors often have varied emission wavelength. In contrast to PSD method which utilizes the rise and decay time of scintillators, we exploited the emission wavelength property of scintillators to discriminate radiation signals at the detector level.

The schematic of the proposed method is illustrated in figure 1. Optical filters with appropriate bandwidth matching that of the scintillators in phoswich configuration can be used to allow or block light photons of selected bandwidth. For example, a two layered phoswich detector will require two optical filters and two photo-detectors. Each scintillator type will require a dedicated optical filter, which only allows light from its corresponding scintillator while blocking that from the other scintillator. Since the origin of light photons (source scintillator) can easily be identified at the detector level based on the optical filter and photodetector, the interacting scintillator (or radiation) can be discriminated without the use of complex algorithms.
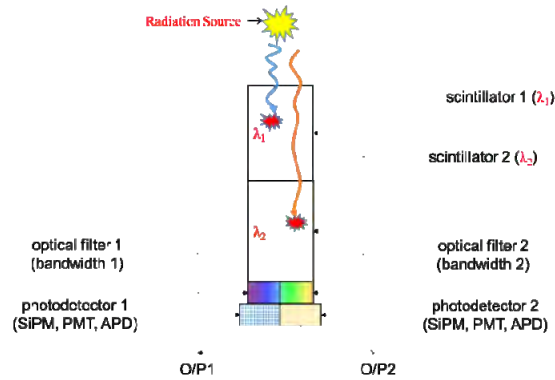
Fig. 1. Basic principle behind Wavelength Discrimination (WLD) method for radiation discrimination.

2. Methods

2.1 Positron probe

A two layered poswich detector has been configured to detect positron particles in the presence of gamma radiation. A detector consisting of a a europium-doped calcium fluoride (CaF$_2$(Eu)) for beta particle detection, and Ce^{3+} doped Lu$_3$Al$_5$O$_{12}$ (Ce:LuAG) (polished) for gamma-ray detection was fabricated. The peak emission wavelengths for CaF$_2$(Eu) and Ce:LuAG are ~425 nm and ~510 nm respectively. The bottom crystal (Ce:LuAG) of phoswich configuration was chosen such that it is able to transmit the wavelength range of the top scintillator CaF$_2$(Eu). Figure 2 shows the scintillators and optical filters used while figure 3 shows the actual detector setup.
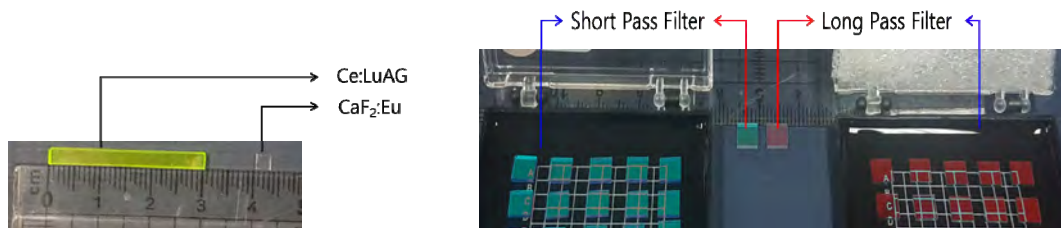
Fig. 2. (left) A photograph of Ce:LuAG and CaF$_2$:Eu scintillators, and (right) optical filters used for the positron probe.
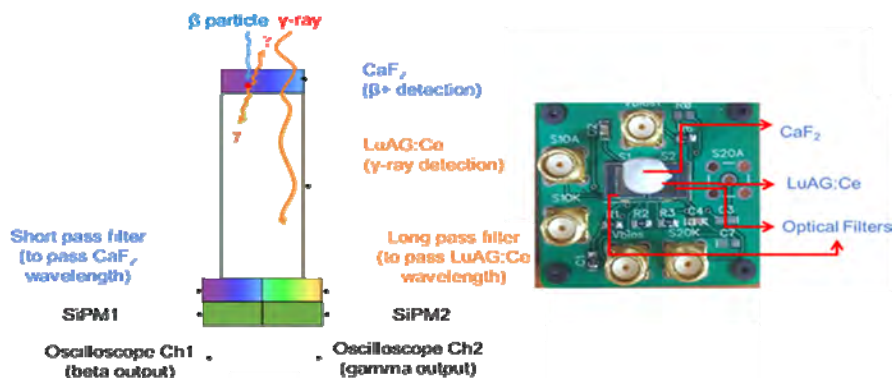
Fig. 3. Illustration and principle of the two-layered phoswich detector coupled to SiPMs for positron-gamma probe application (a), and the actual picture of the phoswich detectors module on a PCB circuit board (b). Since a positron event is always accompanied by the emission of an annihilation gamma radiation. A coincident Ch1 and Ch2 event implies a positron interaction.

Table 1 shows the possible outputs and the corresponding radiation types depending on the SiPM outputs. As a positron interaction will always be accompanied by two gammas annihilation photons, one of which will be directed towards the Ce:LuAG crystal (see figure 4(a)), a coincident signal from both SiPM1 and SiPM2 implies a positron event. A nuclear medicine beta probe with high sensitivity (true positive rate) can thus be achieve by selectively acquiring coincident signals (case 1 events of table 1).

Table 1. Decision table corresponding to signals from SiPMs

Case	Incident radiation type	Actual outputs from	Verdict
1	β+	SiPM1 and SiPM2	β+
2	γ	SiPM2 only	γ
3	β+	SiPM2 only	γ (error event)
4	γ	SiPM1 and SiPM2	β+ (error event)
5	β+	SiPM1 only	Unknown (β+ or ɣ)
6	γ	SiPM1 only	Unknown (β+ or γ)

3. Results

A Na-22 positron source was used to irradiate the scintillators crystals. The radiation source was placed on the top of the phoswich detector. The positron energy spectrum was obtained by setting oscilloscope Ch1 and Ch2 gamma outputs in coincidence (see figure 3). The beta and gamma spectra are shown in figure 5. The energy resolution of the 511 keV annhilation gamma radiation was 18.0%.

Finally, in order to calculate the gamma rejection ratio, a Cs-137 gamma radiation sources were placed above the phoswich detector and 100,000 counts were acquired. Out of the 100,000 counts, 35 coincident events (signal from both SiPM1 and SiPM2 simultaneously) were observed which correspond to the false positive positron events. The gamma rejection efficiency was calculated as 99.965% by using equation 1.

$$\gamma \text{ rejection ratio } (\%) = \frac{(\gamma \text{ counts}) - (\text{false postive } \beta \text{ counts})}{\text{total counts}} \times 100\% \tag{1}$$
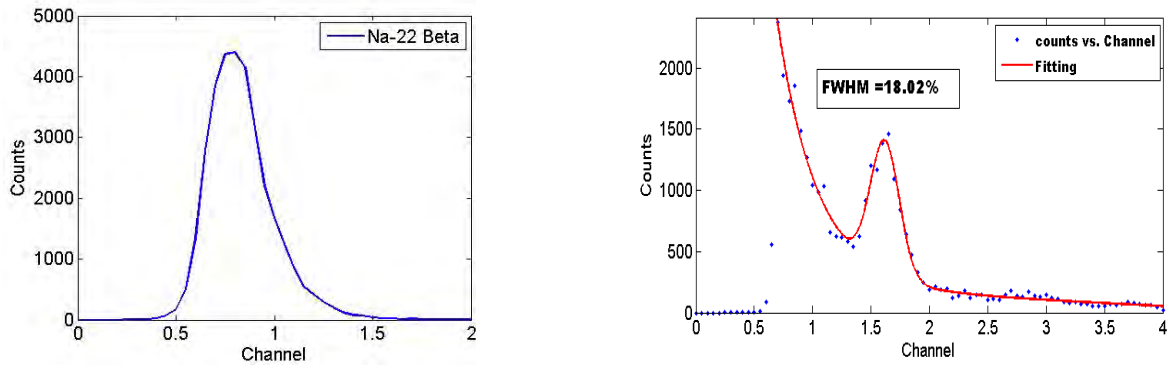
Fig. 5. Positron (β+) (a), and Gamma (γ) (b) spectra of CaF$_2$(Eu) and Ce:LuAG respectively with a Na-22 positron source.

4. Discussion and Conclusion

We propose a new wavelength discrimination (WLD) method for 1) discriminating positron and gamma radiation, and 2) PET DOI detector at the expense of some light lost due to the use of the optical filters.

When applied to a positron probe, the proposed detector is capable of accurately discriminating between positron and gamma radiation, and an excellent gamma rejection ratio was acquired (99.965%). This can be achieved real-time without fast digitizers or complex algorithms.

Acknowledgments

Improvement of LGSO scintillator

Yutaka Anzai, Junya Osada, Katsuhiro Nagao and Hiroyuki Ishibashi

Oxide Corporation, Japan

Abstract

Recent improvement in scintillation performance of LGSO has been reviewed. Material composition such as Ce concentration of LGSO crystal has impacted to its light output and decay time and energy resolution.

1. Introduction

Table 1 shows the properties of Lu-based silicate scintillators. These scintillators are currently used as radiation detectors for a TOF-PET.

Table 1. Comparison in properties of typical scintillators for TOF-PET

	LSO	LYSO	LGSO
Density (g/cm^3)	7.4	7.2	7.3
Effective Atomic Number Z$_{eff}$	63	63	63
Emission Wavelength λ_{em} (nm)	410	410	410
Light Output (NaI=100)	~90	~90	~90
Decay Time (ns)	41	41	41
Energy Resolution (% at 662keV)	~8	~8	~8
Refractive Index	1.83	1.83	1.83
Hygroscopicity	No	No	No
Radioactivity	Yes	Yes	Yes
Growth Method	CZ	CZ	CZ
Melting Point (ºC)	2150	2100	2100

LGSO ($Lu_{2-x}Gd_xSiO_5$:Ce, x~0.2) has a high stopping power and a short decay time, which already makes it very suitable for PET, but its scintillation performances were only moderate initially as compared to other Lu-based scintillators. Then Hitachi Chemical discovered Fast-LGSO with around 34 ns of faster decay time than conventional LGSO by modification of its material composition [1]. Timing performance of Fast-LGSO compared with other Lu-based silicate scintillators were measured by S. Yamamoto as shown in figure 1 [2]. Slightly lower light output of the Fast-LGSO might be a remaining problem [3].
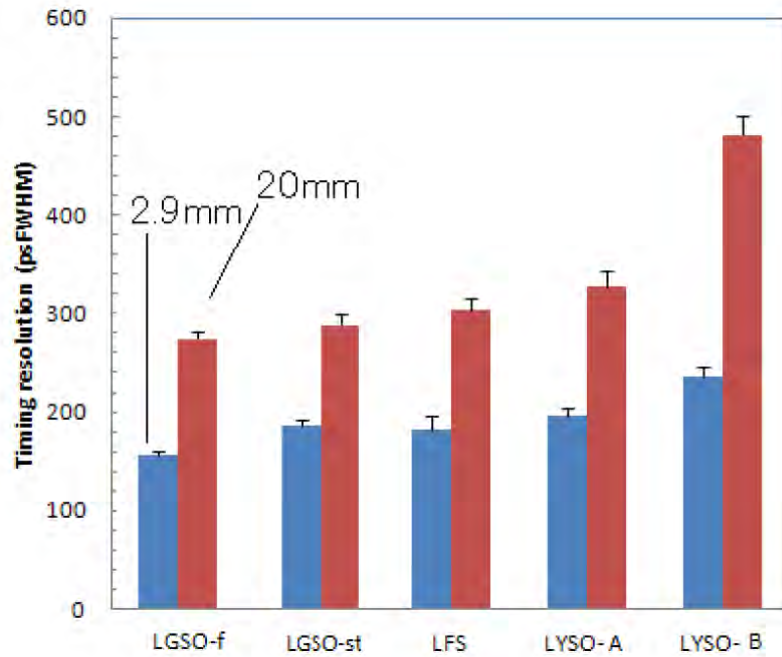
Figure 1. Coincidence timing resolution of Lu-based scintillators for 2.9 mm long (blue) and 20 mm long (red) [3].

2. Recent improvement of LGSO

To improve scintillation performance of LGSO, we have tried to optimize its material composition such as Ce concentration using a more established crystal preparation technology at Oxide. Table 2 shows results of the improvement of LGSO with different Ce concentration.

Table 2. Scintillation performance of improved LGSO with different Ce concentration

Ce concentration	High	Middle	Low
Light output (relative)	113	116	115
Decay time	42 ns	40 ns	36 ns
Energy resolution at 662keV	9.3 %	8.9 %	8.8 %

Results of timing resolution of the improved LGSO will be discussed in the session.

References

[1]   S. Shimizu et al., IEEE Trans. Nucl. Sci. **NS57** (2010) 55.

[2]   S. Yamamoto et al., Technical Report, 2015 JINST-2015, Published by IOP Publishing for Sissa Medialab.

[3]   S. Shimizu et al., IEEE Trans. Nucl. Sci. **NS57** (2010) 1512.

Timing performance for a single- and dual-end readout detectors using segmented crystal bars with subsurface laser engraving

Akram Mohammadi[1], Sodai Takyu[1], Eiji Yoshida[1], Fumihiko Nishikido[1], Keiji Shimizu[2], Toshiaki Sakai[2], Taiga Yamaya[1]

[1] National Institute of Radiological Sciences (NIRS-QST), Japan

[2] Hamamatsu Photonics K.K., Japan

Abstract

The quality and uniformity of positron emission tomography (PET) images can be improved significantly by time-of-flight (TOF) and depth-of-interaction (DOI) capabilities. We have already developed a DOI dual-end readout detector using crystal bars segmented by applying a subsurface laser engraving (SSLE) technique. The DOI was determined by the ratio of detected light between two readouts using Anger calculations. In this study, we investigated the influence of the number of DOI segments on timing performance of a single- and dual-end readout detectors composed of a lutetium fine silicate (LFS) single crystal bar ($3\times3\times20$ mm^3) having several DOI segments, made by applying the SSLE technique, and Hamamatsu TOF PET modules. The coincidence resolving time (CRT) was evaluated by facing the single- or dual-end readout detector to another Hamamatsu TOF PET module coupled with the same LFS crystal bar without DOI as a reference detector. The CRT for each segment of the crystal bars was obtained from irradiation of that segment and the CRT of the segment coupled to the MPPC was improved 10% compared with the top segment of the crystal for single-end detector. The improvement of timing performance of the detector with dual-end readout was observed for all segmented crystal bars.

1. Introduction

Time-of-flight (TOF) positron emission tomography (PET) uses precise measurements of 511 keV photon interaction times to position annihilation events within system detector lines-of-response [1]. TOF information can greatly improve PET image quality due to significant improvement of the signal to noise ratio. Moreover, depth-of-interaction (DOI) information increases spatial resolution of PET images. Therefore, TOF and DOI information can significantly enhance quality and uniformity of PET images [2].

Several types of DOI detectors have been proposed using monolithic scintillators or segmented scintillator arrays composed of small crystal elements for PET detectors [3-7]. We recently developed a dual-ended detector using segmented crystal bars [8]. Conventional fabrication of segmented crystal bars needs complicated crystal cutting and assembly steps; however, we obtained the segmented bars by using the subsurface laser engraving (SSLE) technique which provides efficient and precise fabrication [9]. We identified 13 DOI segments by two-sided readout of multi pixelated photon counter (MPPC). Next, we are planning to add TOF capability to our DOI detector for a prototype TOF-PET system with high timing

performance. Therefore, in this study, we evaluate coincidence timing performance of segmented crystal bars with various numbers of DOI segments to determine the influence of the DOI segment numbers on timing resolution of single- and dual-end detector.

2. Methods

Scintillation crystal bars $(3\times3\times20$ mm$^3)$ of lutetium fine silicate (LFS) were segmented in the height direction using the SSLE technique. The crystal bars were segmented into two to a maximum of six DOI segments with an equal height as shown in Figure 1. We used a Hamamatsu TOF PET module (C13500-4075LC-12), which has a highly accurate photon arrival timing measurement function composed of a 12×12 MPPC and signal processing circuit, see Figure 1. The MPPCs are TSV (through silicon via) type with an effective area of 4×4 mm^2 and 0.075 mm pitch sub pixels.
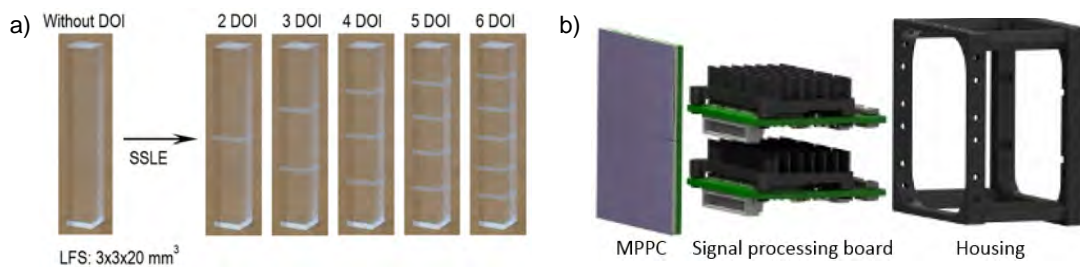
Figure 1 Crystal bars with 2 to 6 DOI segments formed by applying the SSLE technique to monolithic crystal bars, a), the TOF-PET MPPC module, b).
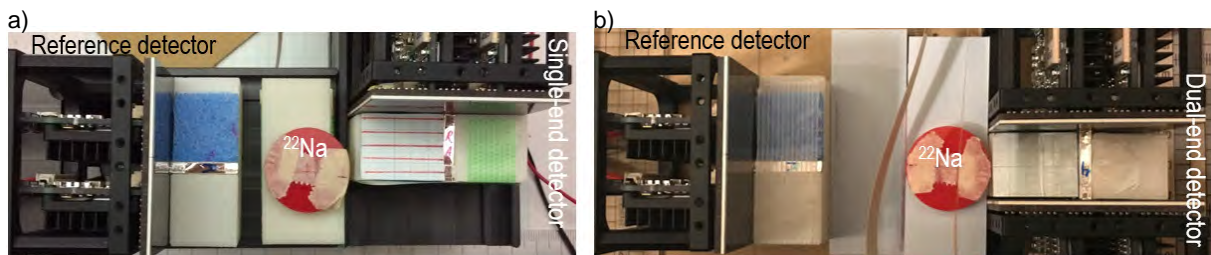
Figure 2 Experimental setup for measuring CRT of each segment of crystal bars for single-end, a), and dual-end, b), detectors.

Coincidence resolving time (CRT) of each segment of all crystal bars with different numbers of DOI segments was measured for single and dual-end detectors using side irradiation of the segmented crystal bars as shown in Figure 2. The lateral and top surfaces of segmented crystal bar were wrapped in mirror reflectors and the bases were optically coupled to one channel of the MPPC module at the middle of the array for the single-end detector. Although, for dual-end detector the lateral surfaces of the segmented crystal bars were only wrapped in the reflectors and both bases were optically coupled to two channels of

two MPPC modules, see Figure 2 (right). A crystal bar of LFS without DOI segment was coupled to another TOF PET MPPC module and it was used as a reference detector. Since we did not have enough segmented crystal bars and MPPC modules the reference detector for CRT evaluation of both single and dual-end detectors was a single-end detector. CRT for each segments was measured by side irradiation of that segment of the detector using a ^{22}Na point source (Figure 2).

3. Results

The CRT histogram for the center segment of the dual-end detector composed of a crystal bars with three DOI is shown in Figure 3. The intrinsic timing resolution of the MPPC modules was 15.625 ps per channel. The histogram was fitted by a Gaussian function to obtain the FWHM value and it was 229 ps for center segment of the dual-end detector with three DOI segments.
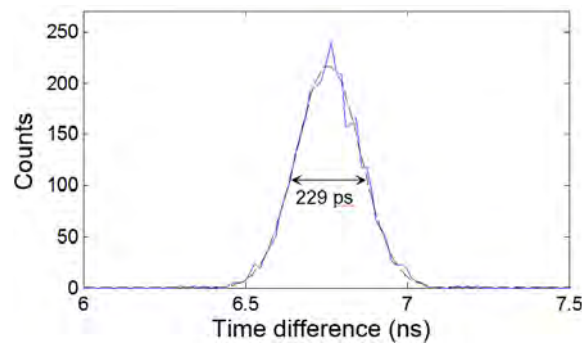
Figure 3 CRT histogram between the reference detector and the center segment of the dual-end detector composed of the crystal with three DOI segments.
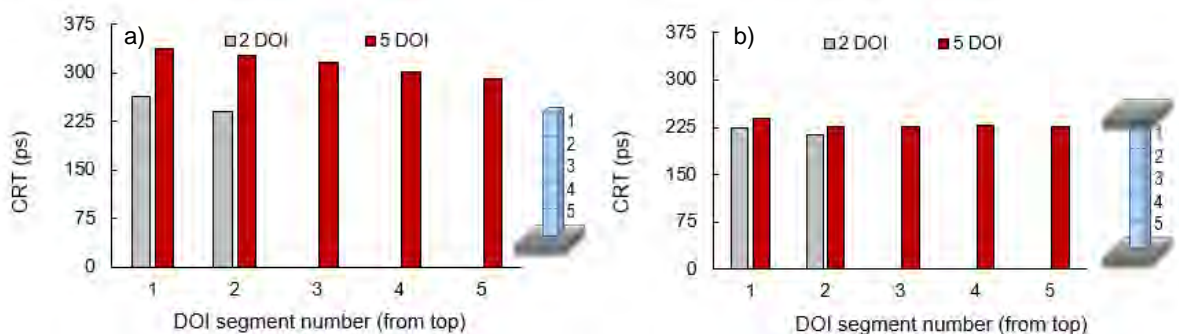
Figure 4 CRT (ps) of each segment of single-end, a), and dual-end, b), detectors with two and five DOI segments.

The CRT for each segment of the detectors with two and five DOI segments are shown in Figure 4 for both single- and dual-end detectors. The top (first) segment showed the highest value of the CRT and the

segment coupled to the MPPC showed the minimum CRT for the single-end detector. In other words, the CRT of the base segment was improved 10% compared with the top segment for the single-end detector. CRT for dual-end detector was smaller than that of single-end detector and did not show significant differences for different segments of crystal bars. Timing resolution of dual-ended detector improved around 20% compared with single-end detector as it was expected.

4. Discussion

The CRT of each segment of crystal increased with the increased number of DOI segments for both single- and dual-end detectors. An insignificant change (less than 25 ps) between CRTs of individual segments of a segmented crystal bar was observed for single-end detector (see Figure 4a)). Almost the same CRT values were observed for individual segments of a dual-end detectors with five (two) DOI segments. The CRT for individual segments of the detector composed of a crystal bar with five DOI segments were less than 340 and 240 ps for the single- and dual-end detectors, respectively. Improvement of timing performance of the detector with the dual-ended readout is due to shorter distance that scintillation light propagates to reach the MPPCs compared with single-end detector.

5. Conclusions

We investigated timing performance of a single- and dual-end detectors composed of a crystal bar with different numbers of DOI segments. The LFS crystal bars of $3\times3\times20$ mm^3 were segmented in the height direction using the SSLE technique. Hamamatsu TOF PET modules were used to investigate timing performance of the crystal bars. The CRT of each segment of crystal increased with the increased number of DOI segments for both single- and dual-end detectors. We observed an insignificant change between CRTs of individual segments of a segmented crystal bar for both detectors. The CRT for individual segments of the detector composed of a crystal bar with five DOI segments were less than 340 and 240 ps for the single- and dual-end detectors, respectively. We observed improvement of timing performance of the detector with a dual-ended readout.

References

[1]   J. S Karp et al., "Benefit of time-of-flight in PET: experimental and clinical results," J Nucl Med., 49, pp 462-70, 2008.

[2]   V. C. Spanoudaki et al., "Investigating the temporal resolution limits of scintillation detection from pixellated elements: comparison between experiment and simulation," Phys Med Biol., 56, pp 735-56, 2011.

[3]   S. Yamamoto, H. Ishibashi, "A GSO depth of interaction detector for PET," IEEE Trans Nucl Sci., 45, pp 1078-1082, 1998.

[4]   RS Miyaoka *et al.*, "Design of a depth of interaction (DOI) PET detector module," IEEE Trans Nucl Sci., 45, pp 1069-1073, 1998.

[5]   T. Tsuda T *et al.*, "A Four-Layer Depth of Interaction Detector Block for Small Animal PET," IEEE Trans Nucl Sci., 5, pp2537-2542, 2004.

[6]   Y. Yang *et al.*, "Investigation of depth of interaction encoding for a pixelated LSO array with a single multi-channel PMT," IEEE Trans Nucl Sci., 56, pp 2594-9, 2009.

[7]   *D. R. Schaart et al.,* "A novel, SiPM-array-based, monolithic scintillator detector for PET," Phys. Med. Biol., *54, pp 3501-12, 2009.*

[8]   A. Mohammadi et al., "Development of an Isotropic DOI Detector Based on a Dual-Ended Readout and Subsurface Laser Engraving Technique," NSS-MIC 2016, Strasbourg, France.

[9]   T Moriya et al., "Fabrication of finely pitched LYSO arrays using sub-surface laser engraving technique with picosecond and nanosecond pulse lasers," IEEE Trans Nucl Sci., 61, pp 1032-38, 2014.

Highly Integrated FPGA-only Signal Digitization Method Using Single-ended Memory Interface Input Receivers

Jun Yeon Won[1,2] and Jae Sung Lee[1,2]

[1] Department of Biomedical Sciences, Seoul National University, Korea

[2] Department of Nuclear Medicine, Seoul National University, Korea

Abstract

We propose a new highly integrated FPGA-only signal digitization method for individual signal digitization of time-of-flight positron emission tomography (TOF PET). We configured I/O port of the FPGA with a single-ended memory interface (SeMI) input receiver. The SeMI is a single-ended voltage-referenced interface that has a common reference voltage per I/O Bank, such that each SeMI input receiver can serve as a voltage comparator. The FPGA-only digitizer that uses the single-ended input receivers does not require a separate digitizing integrated chip, and can obtain twice as many signals as that using LVDS input receivers. We implemented a highly integrated digitizer consisting of 82 energy and 82 timing channels using a 28-nm FPGA. The energy and arrival time were measured using a 625-ps binary counter, and a 10-ps TDC, respectively. We fed signals from the TOF PET detectors to the SeMI input receivers directly and collected data. The TOF PET detector consisted of a $3\times3\times20$ mm^3 LYSO crystal coupled with a silicon photomultiplier. The energy resolutions were 7.7% and 7.1% for two TOF PET detectors. The coincidence resolving time was 204 ps FWHM. The SeMI digitizer with a high-performance signal digitizer, processor, and high-speed transceivers provides a compact all-in-one data acquisition system.

1. Introduction

Individual signal readout of TOF detectors can draw the best timing performance; however, it requires a large number of signal digitization channels. ASICs are highly integrated, resulting in high-performance signal digitization with low power consumption and small footprint. However, given that most ASICs use a LVDS interface for communication, ASICs require an additional FPGA to process data and transfer data packets to a host computer. Compared with ASICs, FPGA-only digitizers have the advantage of using a single FPGA for signal digitization and communication [1]. However, the conventional FPGA-only digitizers use LVDS input receivers as voltage comparators, each requiring two configurable input/output (I/O) ports: one for the signal and the other for the threshold. Thus, the number of signal digitization channels is less than half the total available I/O ports.

In this paper, we propose a new highly integrated FPGA-only signal digitization method using single-ended input receivers. The voltage comparator implemented using the single-ended interface of the FPGA has the advantage that almost all configurable FPGA I/O ports can be used as digitization channels.

2. Single-ended Memory Interface (SeMI) Digitizer

We refer to a new FPGA-only digitizer as a single-ended memory interface (SeMI) digitizer where the analog signal is digitized by the single-ended voltage-referenced input receiver and the logic state is read by timestamp modules consisting of multiphase counters (MPCNTs) and time-to-digital converters (TDCs) implemented in the same FPGA as shown in Figure 1.
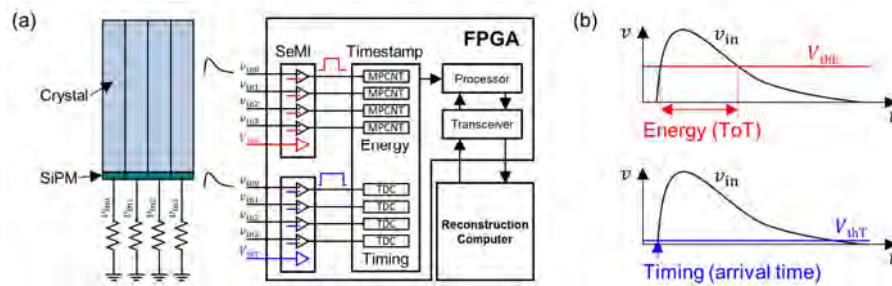

Figure 1. Conceptual diagram of the SeMI digitizer. (a) Individual signal readout of SiPM-based TOF PET detector. (b) Energy and timing measurement methods using the SeMI digitizer.

2.1 Single-ended Memory Interface (SeMI) Input Receiver

Most FPGA I/O ports can be configured with single-ended / differential and supply voltage-ratioed / voltage referenced interfaces. In the Joint Electron Device Engineering Council (JEDEC) standards, SeMI such as stub series terminated logic (SSTL) and high-speed transceiver logic (HSTL) are single-ended voltage-referenced interfaces where the logic state of the input receiver is determined by comparing the input signal with an adjustable common reference voltage (V_{REF}). Therefore, by applying analog signal and the common threshold to the SeMI input receiver and a dedicated V_{REF} port, respectively, the SeMI input receivers function as multiple voltage comparators as shown in Figure 2(c). A notable advantage of the SeMI input receiver is that each signal digitization channel requires only one configurable I/O port, since the SeMI input receivers in an I/O bank share a common V_{REF}.
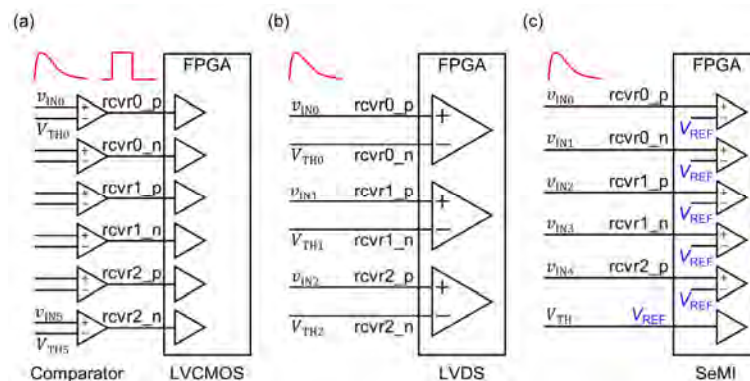

Figure 2. Time-based signal digitization methods. (a) Conventional signal digitization method using the discrete voltage comparators. (b) FPGA-only signal digitization method using the LVDS input receivers. (c) Proposed FPGA-only signal digitization method using the SeMI input receivers.

2.2 Timestamp Module

The MPCNT operated at 400 MHz with phases of 0°, 90°, 180°, and 270°, providing a time resolution of 625 ps to obtain time-over-threshold (ToT) [2]. The tapped-delay-line TDC with a 10-ps resolution was used to measure the arrival time when the leading edge of the signal crossed V_{REF} at the SeMI input receiver [3], [4].

2.3 Implementation of SeMI Digitizer

We implemented a highly integrated digitizer consisting of 82 energy and 82 timing channels using 171 I/O ports (164 ports for digitization channels and 7 ports for V_{REF}) in five I/O Banks. The input signal was directly fed into the SeMI input receiver and terminated to the ground using a 50 Ω resistor. A bypass capacitor of 0.1 μF was placed between V_{REF} and the ground. The V_{REF} values were adjusted using a 12-bit DAC (LTC2625, Linear Technology) from 0 to 2.048 V in steps of 0.5 mV.

3. Experimental Setup

We acquired the ToT and the arrival time of coincidence events from TOF detectors to demonstrate the feasibility of SeMI digitizer as a DAQ system. In addition, the energy resolution and coincidence resolving time (CRT) were compared with those obtained using a 5-GSPS waveform digitizer (DT5742B, CAEN).

We assembled two TOF detectors, each consisting of a 3×3×20 mm^3 LYSO crystal and a SensL J-series SiPM (MicroFJ-SMA-30035) as shown in Figure 3. The LYSO crystal was polished and wrapped with an enhanced specular reflector film (ESR, 3M).

For the data acquisition using the waveform digitizer as shown in Figure 4(a), the standard and the fast output signals of two detectors were sampled. The energy was obtained using either integration or *in-silico* ToT method. The integration method was to sum the standard output signal for 160 ns after baseline correction. The *in-silico* ToT was to extract pulse width when the standard output signal crossed the voltage threshold of 400 mV. In addition, the relation between energy and ToT for each detector was obtained. The arrival time was picked off when the interpolated fast output signal crossed the voltage threshold of 5 mV.

For the data acquisition using the SeMI digitizer as shown in Figure 4(b), the standard and the fast output signals were fed into the SeMI input receivers with respective V_{REF} values of 400 mV and 5 mV. The ToT was obtained from the standard output signal using MPCNT, and then calibrated with energy. The arrival time was picked off from the fast output signal, and then measured by TDC.
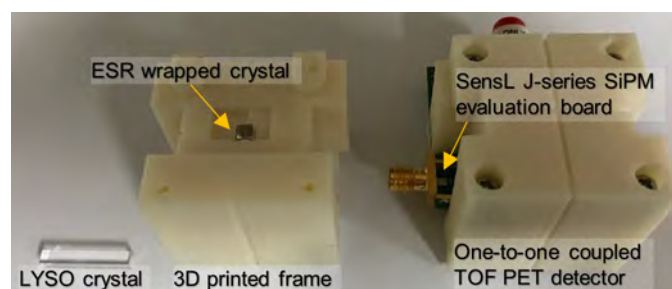
Figure 3. One-to-one coupled TOF PET detector.
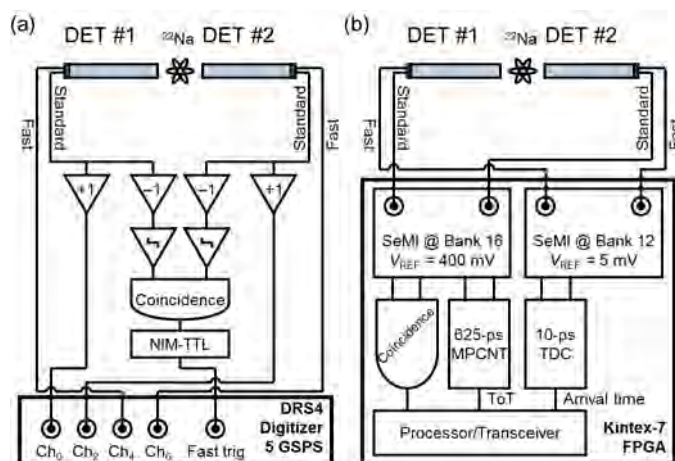
Figure 4. Individual signal readout of TOF detectors
using (a) the waveform digitizer and (b) the SeMI digitizer.

4. Results

The SeMI digitizer obtained the comparable performance with the 5-GSPS waveform digitizer. The photopeak of energy histogram obtained using the SeMI digitizer was well resolved as shown in Figure. 5(a). The energy resolutions of two detectors using the integration method were 6.1% and 6.8%. Those using the *in-silico* ToT method were 7.5% and 6.5%. Those using the SeMI ToT were 7.7% and 7.1%. The CRT values within energy windows generated by the integration, *in-silico* ToT, and SeMI ToT were 203, 205, and 204 ps FWHM, respectively.
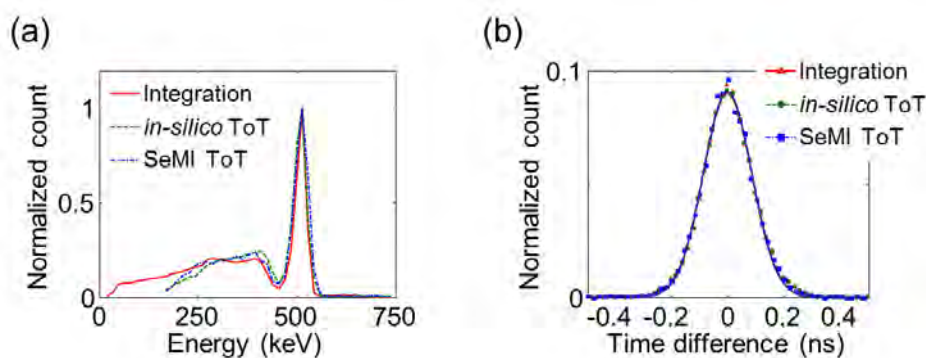
Figure 5. (a) Normalized energy histograms using integration, *in-silico* ToT, and SeMI ToT methods.
(b) Normalized time difference histograms within energy windows
generated using integration, *in-silico* ToT, and SeMI ToT methods.

5. Conclusions

We proposed a new highly integrated FPGA-only digitizer using the SeMI input receiver that enables one to use almost every I/O port as a comparator. The SeMI digitizer demonstrates the great prospects that the FPGA itself can be used as an all-in-one DAQ system suitable for individual signal readout of TOF detectors.

Acknowledgments

References

[1]   D. Xi, C.-M. Kao, W. Liu, C. Zeng, X. Liu, and Q. Xie, "FPGA-Only MVT Digitizer for TOF PET," IEEE Transactions on Nuclear Science, vol. 60, no. 5, pp. 3253-3261, 2013.

[2]   J. Wu, S. Hansen, and Z. Shi, "ADC and TDC Implemented Using FPGA," Nuclear Science Symposium Conference Record, 2007. NSS '07. IEEE, pp. 281-286, 2007.

[3]   J. Y. Won, S. I. Kwon, H. S. Yoon, G. B. Ko, J. W. Son, and J. S. Lee, "Dual-Phase Tapped-Delay-Line Time-to-Digital Converter With On-the-Fly Calibration Implemented in 40 nm FPGA," IEEE Trans Biomed Circuits Syst, vol. 10, no. 1, pp. 231-42, Feb 2016.

[4]   J. Y. Won and J. S. Lee, "Time-to-Digital Converter Using a Tuned-Delay Line Evaluated in 28-, 40-, and 45-nm FPGAs," IEEE Transactions on Instrumentation and Measurement, vol. 65, no. 7, pp. 1678-1689, 2016.

Improvement of edge crystal separation using a light guide for high resolution small animal PET detector – GATE simulation study

Han Gyu Kang[1], Sodai Takyu[1], Fumihiko Nishikido[1], Akram Mohammadi[1], Naoko Inadama[1], Eiji Yoshida[1], and Taiga Yamaya[1]

[1] National Institute of Radiological Sciences (NIRS-QST), Japan

Abstract

The spatial resolution of small animal positron emission tomog4raphy (PET) scanner be improved by using small cross section scintillation crystal. However, the separation of crystals becomes more difficult as the cross section of the crystal is reduced. In particular, the identification of edge crystals is more challenging than the central crystals. This aim of this study is to improve the edge crystal separation by using an optimized light guide for small animal PET detector. The small animal PET module consists of an 11 × 11 array of pixelated LYSO crystals ($0.92 \times 0.92 \times 10.0$ mm^3), a 1 mm thick light guide, and a 4 × 4 array SiPM (Hamamatsu Photonics, Japan; S13361-3050NE-04; each channel has an effective area of 3×3 mm^2). The optical characteristics of LYSO and the SiPM were taken into account for the GATEv6.2 optical simulation. In order to improve the crystal resolvability in the edge and corner regions, four air slits were inserted into the light guide. The flood map was obtained with various slit depths of 0.2, 0.5, and 0.8 mm, respectively. The separation of the corner crystals could be improved by using a combination of a light guide thickness of 1 mm, and a slit depth of 0.5 mm without compromising energy resolution. In future, the optimized light guide design using GATE optical simulation will be validated by an experimental measurement.

1. Introduction

Small animal positron emission tomography (PET) scanner employing a scintillation crystal with a small cross section (~1 mm^2) can improve the spatial resolution. PET detectors with high spatial resolution are also required for PET inserts for the virtual pinhole[1] and whole gamma imaging[2]. However, the use of small scintillation crystal makes it hard to identify the crystals at the edge and corner regions. Therefore, the aim of this study is to optimize the light guide design using GATEv6.2 optical simulation to improve the resolvability of the edge and corner crystals in the 2D flood histogram. In this paper, the optical simulation results of a pixelated LYSO crystal array with different light guide designs are presented.

2. Methods

2.1 GATEv6.2 optical simulation setup

The GATEv6.2 optical simulation[3-4] was performed to improve the resolvability of the edge crystals by using a light guide with air slit. The PET detector module consists of a 11 × 11 array of LYSO crystals ($0.92 \times 0.92 \times 10$ mm^3), a light guide (13 × 13 mm^2), and a 4 × 4 array SiPM as shown in Figure 1(a) and

Figure 2. The crystal pitch was 1 mm and the light yield was set to 26,000 [photons/MeV]. The energy resolution scale of the LYSO crystal was set to 4.4 which corresponds to the intrinsic energy resolution of 9.0% with respect to the 511 keV peak. The surface roughness (σ_α) of the crystal was set to 1.5°, and the surface finish was defined as "ground-back-painted" with a specular lobe constant of 1. A light guide with a refractive index of 1.45 was inserted between the LYSO crystal and SiPM.
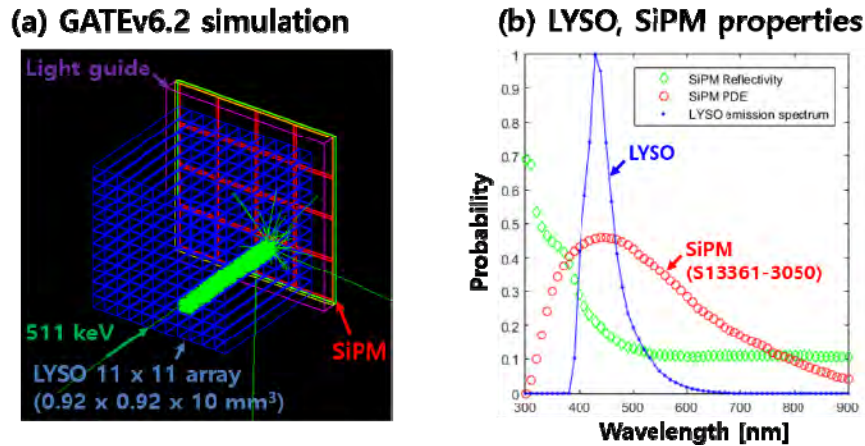
Figure 1. (a) GATEv6.2 optical simulation setup, (b) optical properties of LYSO and SiPM.

The SiPM (Hamamatsu, S13360-3050NE-04, Japan) consists of 4×4 channels, (each channel has an effective area of 3×3 mm^2). The pitch of the SiPM channels was 3.2 mm both in X and Y directions. The photon detection efficiency (PDE) of the SiPM was taken into account for the simulation. Four air slits, each with a width of 0.2 mm, were inserted inside the light guide to improve the edge crystal resolvability as shown in Figure 2.
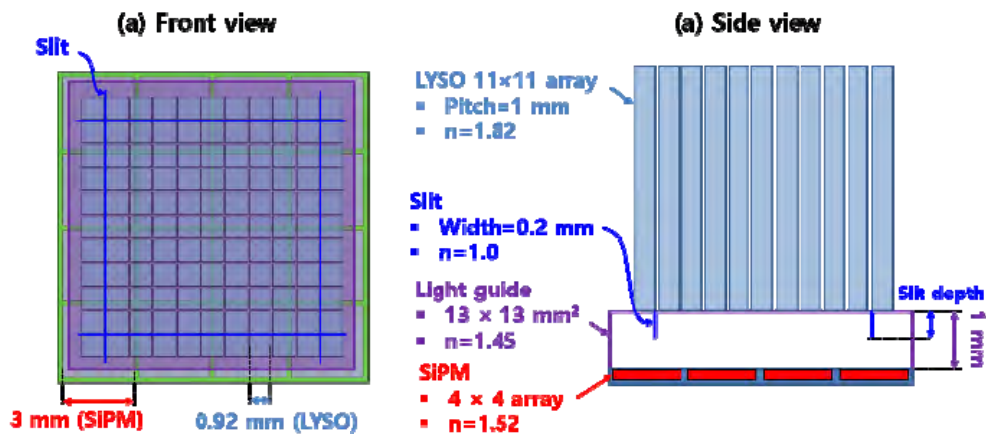
Figure 2. (a) LYSO and SiPM configurations, (b) schematic diagram of the detector geometry.

2.2 Two-layer DOI detector

The GATEv6.2 optical simulation of two-layer DOI PET detector module was performed. The 1st (10×10) and 2nd (11×11) layers were offset to each other to provide DOI information as shown in Figure 3. The light guide thickness of 1 mm was inserted between the LYSO crystal and SiPM. The four air slits were inserted inside the light guide as same as the previous section.
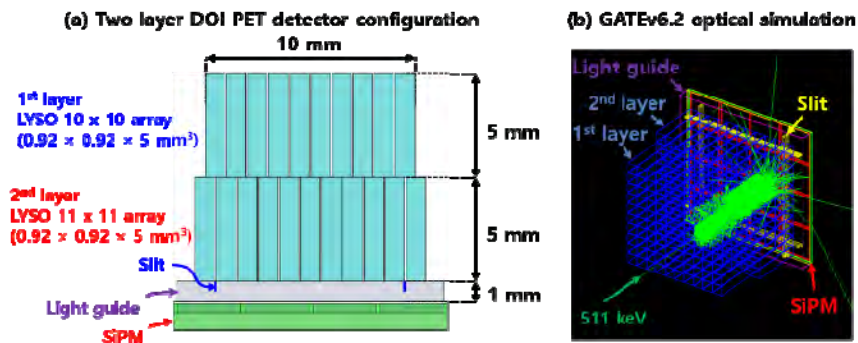
Figure 3. (a) Two-layer small animal DOI PET detector geometry, (b) GATEv6.2 optical simulation setup.

2.3 Data analysis and flood map generation

The GATEv6.2 optical simulation output file (Singles.dat) was analyzed using a custom-made MATLAB code for generation of the flood map. The 2D flood map was segmented using a Voronoi diagram. Subsequently, the photo-peak and energy resolution were calculated. An energy window of 30% with respect to the 511 keV peak was applied to the flood map. The distance-to-width ratio (DWR) of the corner crystals was calculated to evaluate the crystal resolvability at the edge region.

$$DWR = \frac{Average\ distance\ between\ the\ peaks}{Average\ width\ of\ the\ peaks}.$$

3. Results

3.1 Flood map with different light guide thicknesses

The photo-peak values (averaged over the LYSO crystal array) of the 0.5, 1, 2, and 3 mm light guides were 2111 ± 46, 2077 ± 26, 2041 ± 11, and 2015 ± 7 number of photons], respectively. The energy resolutions of 0.5, 1, 2, and 3 mm light guides were 11.7 ± 1.2%, 10.9 ± 0.8%, 10.7 ± 0.8%, and 10.9 ± 0.9%, respectively. The light guides thicker than 0.5mm might slightly lessen the saturation effect of the SiPM. The DWRs of the corner region were 9.02, 5.89, 3.46, and 2.82, respectively. The optimal light guide thickness was 1 mm in terms of the energy resolution and crystal separation as shown in Figure 4.
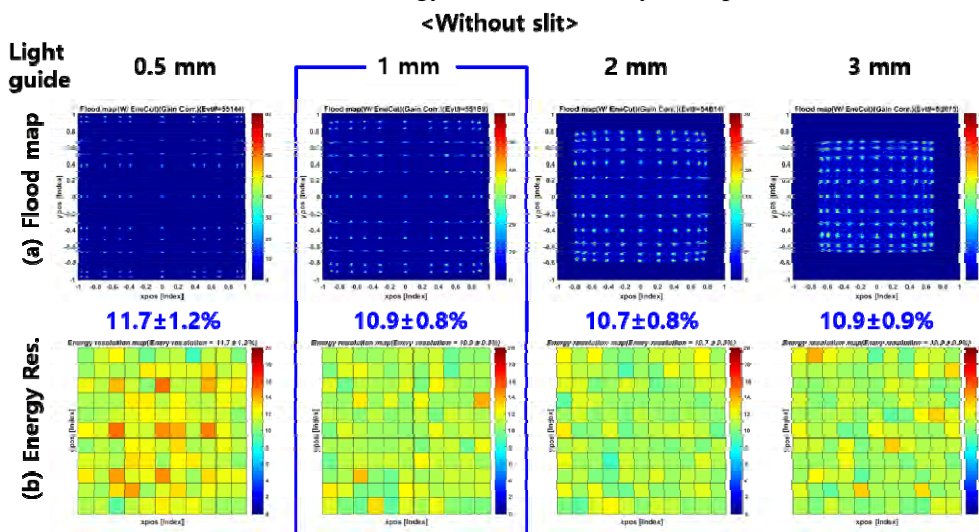
Figure 4. (a) Flood map of LYSO crystal array with different light guide thicknesses and (b) energy resolution map.

46

3.2 Flood map with different slit depths

The flood map was obtained with different slit depths of 0, 0.2, 0.5, and 0.8 mm while the light guide thickness was fixed to 1 mm. In order to evaluate the crystal resolvability, the left top corner region of the flood map was cropped and the line profile was obtained from the second crystal row as shown in Figure 5. The DWRs of the corner region were 5.89, 6.39, 6.65, and 5.98, for the slit depths of 0, 0.2, 0.5, and 0.8 mm, respectively. The photo-peak values were 2077 ± 26, 2060 ± 39, 2063 ± 36, and 2101 ± 18 [#ph.], and the energy resolutions were $10.9 \pm 0.8\%$, $11.0 \pm 0.8\%$, $10.9 \pm 0.9\%$, and $11.2 \pm 1.0\%$, for the slit depths of 0, 0.2, 0.5, and 0.8 mm, respectively.
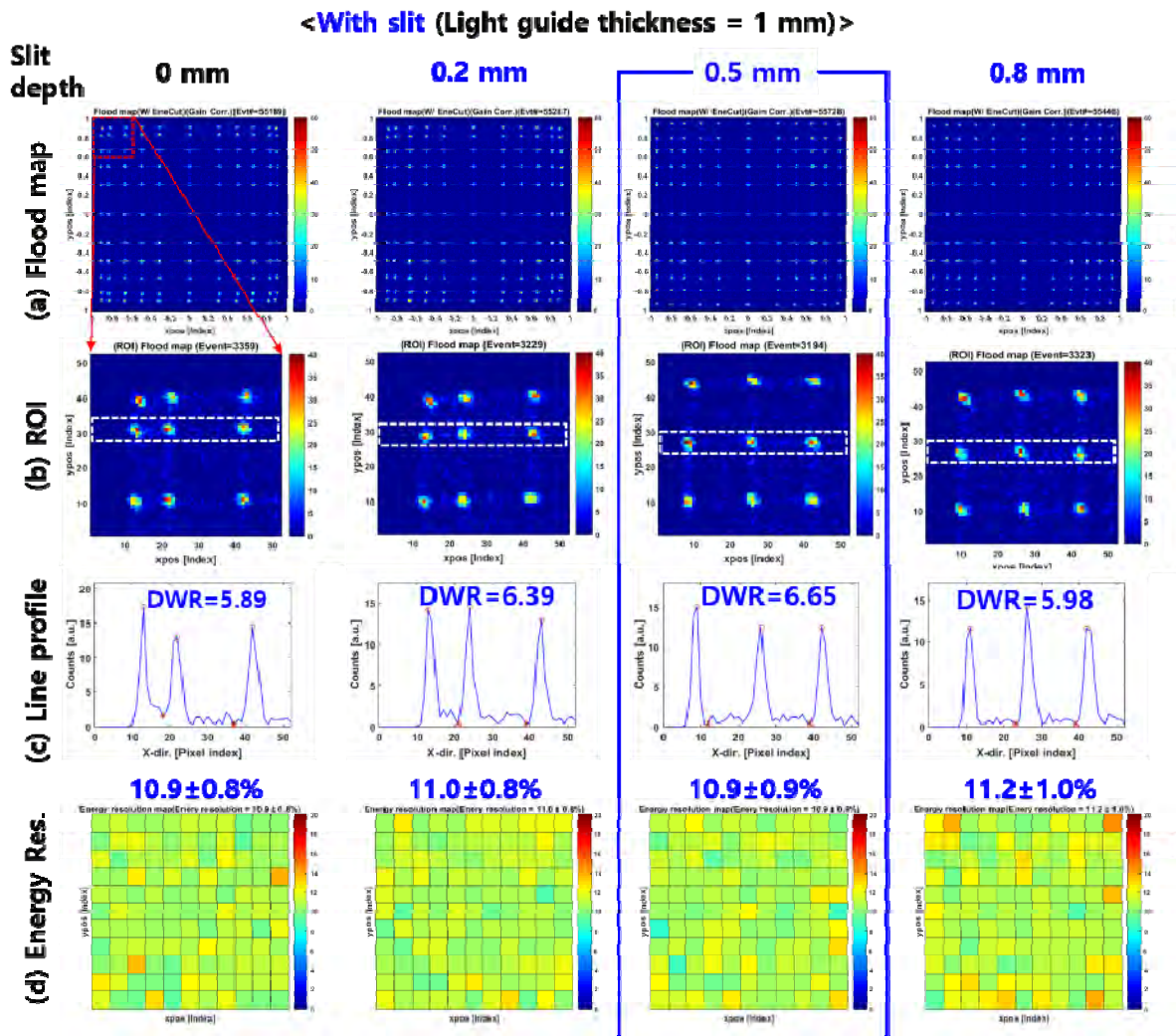
Figure 5. (a) Flood map with various slit depths (0, 0.2, 0.5, and 0.8 mm), (b) ROI, (c) line profile, and (d) energy resolution map.

3.3 Effect of slit on the flood map quality of two-layer DOI PET detector

The corner crystals of 1st and 2nd layers were overlapped each other without slit as shown in Figure 6(a). However, the separation of the 1st and 2nd layer crystals at the corner region could be improved by using a slit depth of 0.5 mm as shown in Figure 6(b).
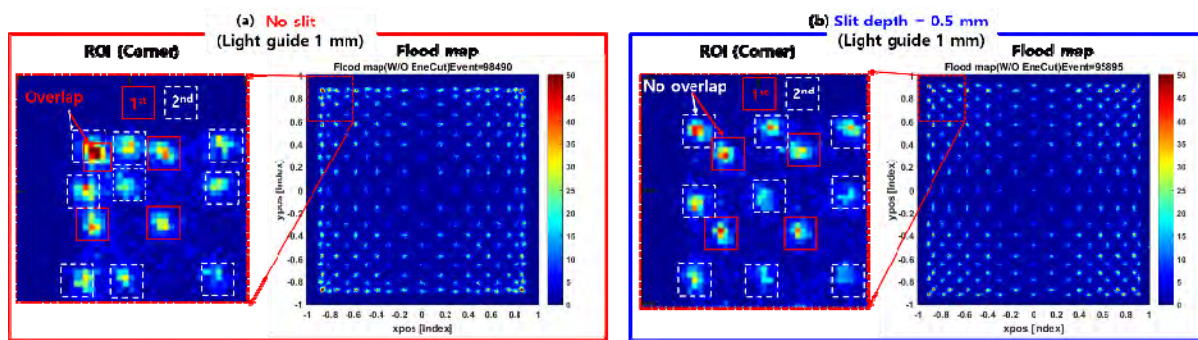
Figure 6. (a) Flood map with various slit depths (0, 0.2, 0.5, and 0.8 mm), (b) ROI, (c) line profile, and (d) energy resolution map.

4. Conclusions

The crystal resolvability could be improved by using four air slits inside the light guide for both non-DOI and two-layer DOI PET detectors. The combination of 1 mm thick light guide and 0.5 mm depth air slits resulted in a best flood map quality in terms of crystal separation. In future, the optimized light guide design using GATEv6.2 optical simulation will be validated by an experimental measurement.

References

[1]   Y-C. Tai, H. We, D. Pal, J. A. O'Sullivan., "Virtual-Pinhole PET" Journal of Nuclear Medicine, vol. 49, no. 3, pp. 471-479, Mar. 2008.

[2]   E. Yoshida, H. Tashima, Y.e Okumura, M. Suga, N. Kawachi, K. Kamada, K. Parodi, T. Yamaya., "Concrete realization of the whole gamma imaging" 2018 IEEE NSS/MIC, M-21-2.

[3]   D Jan van der Laan, Deniss R Schaart, Marnix C. Maas, Freek J. Beekman, Peter Brundonckx, Carel W.E. van Eijk., "Optical simulation of monolithic scintillator detectors using GATE" Physics in Medicine and Biology, vol. 55, no. 6, pp. 1659-1675, Feb. 2010.

[4]   H. G. Kang, S. H. Song, Y. B. Han, K. M. Kim and S. J. Hong, "Lens implementation on the GATE Monte Carlo toolkit for optical imaging simulation" Journal of Biomedical Optics, vol. 23, no. 2, pp. 1-13, Feb. 2018.

Initial results of a prototype brain PET scanner using a time-based digitizer and an FPGA-based real-time coincidence processor

Jeong-Whan Son[1,2], Jun Yeon Won[1,2], Kyeong Yun Kim[1,2], Haewook Park[1,2], Min Sun Lee[1], Seungeun Lee[1,2], Guen Bae Ko[1] and Jae Sung Lee[1,2]

[1] Department of Nuclear Medicine, Seoul National University, South Korea

[2] Department of Biomedical Sciences, Seoul National University, South Korea

Abstract

A prototype brain-dedicated PET scanner was developed with a ring diameter of 254 mm and an axial length of 26 mm. The scanner was based on dual-layer depth-of-interaction detectors—each block consisting of a 14×14 array of 1.78×1.78×12 mm^3 and 13×13 array of 1.78×1.78×8 mm^3 LSO crystals. Time-based digitizers and FPGA-based data acquisition systems were used. The average energy resolutions were 10.7±0.6% and 11.1±1.5% for the upper and lower layer crystals, respectively. The reconstructed brain phantom image showed better spatial resolution and contrast recovery compared to that of a clinical whole-body scanner. The developed PET scanner showed promising results of resolving detailed structures of phantoms without edge artifacts.

1. Introduction

Our group is developing a brain-dedicated PET insert that can be combined with an ultra-high field (7T) MRI system. As the first step of this research, we present a prototype brain PET scanner with a ring diameter of 254 mm and an axial field-of-view (FOV) of 52 mm consisting of two time-based digitizers and FPGA-based data acquisition (DAQ) systems.

2. Materials and methods

2.1 Prototype brain PET scanner

The prototype brain PET system was composed of 14 sectors—each supporting four (2×2) depth-of-interaction (DOI) detector blocks. The PET detector block consisted of a 14×14 array of 1.78×1.78×12 mm^3 (lower layer) and a 13×13 array of 1.78×1.78×8 mm^3 (upper layer) LSO crystals coupled with a 2×2 array of 4×4 silicon photomultipliers (SiPMs) as shown in Fig. 1. The 64 output signals were multiplexed into four position-encoding signals and one timing signal. The present scanner is equipped with a single detector block ring which yields 26 mm axial length. The main characteristics of the PET scanner are summarized in Table I.
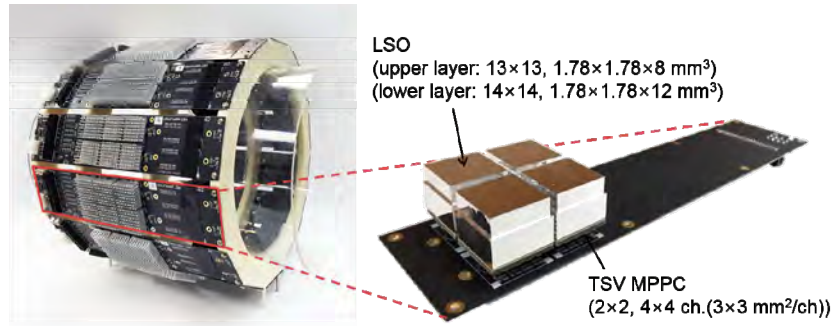
Figure 2. The developed prototype brain PET scanner and its detector sector (axial length extended).

Table 1. Major characteristics of a prototype brain PET scanner

Characteristics	Value
Crystal material	LSO
Crystal block (mm^3)	1.78×1.78×8, 13×13 array (upper layer)
	1.78×1.78×12, 14×14 array (lower layer)
SiPM	TSV MPPC (4×4 channels), 2×2 array
SiPM photosensitive area/ch.	3×3 mm^2
Ring diameter (mm)	254
Axial field-of-view (mm)	26 (present) or 52 (extended)
Energy window (keV)	409–613 (± 20%)
Time window (ns)	± 2

2.2 Data acquisition system

The data were acquired using two time-based digitizers and one coincidence processor. Each time-based digitizer had 132 energy channels and 33 timing channels, which can support up to 33 detector blocks (8 detector sectors). The position-encoding signals were digitized using charge-to-time converters (QTC) that linearly converts the energy into the pulse width. Then, the pulse width was measured using a binary counter with a resolution of 625-ps implemented in a Kintex-7 FPGA (KC705, Xilinx). The timing information was acquired using a time-to-digital converter (TDC) with a 10-ps resolution implemented in the same FPGA[1]. The developed QTC and its energy performance is shown in Fig. 2. Single event data including the position, energy, and arrival time were sent to the master FPGA through 2.5-Gbps transceiver. The coincidence processor implemented in a Virtex-6 FPGA (ML605, Xilinx) compared the arrival times of single event data and generated prompt and delayed coincidence data[2]. The coincidence pairs were transmitted to the acquisition computer using 1-Gbps Ethernet. Data were processed using a custom-built acquisition and system management software tool[3]. In addition, the in-house clock distributor was used to synchronize the clock signals in the DAQ systems.
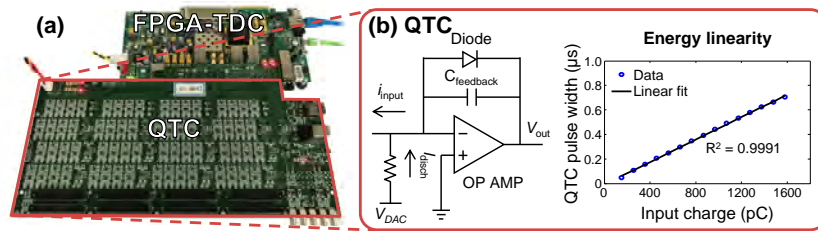
Figure 3. (a) The developed time-based digitizer (i.e., QTC and FPGA-based TDC). (b) The QTC circuit and its energy performance.

2.3 Phantom studies

A two-dimensional Hoffman brain phantom filled with ^{18}FDG was scanned and the reconstructed image was evaluated by comparing with those acquired using a clinical whole-body PET/CT scanner (Siemens mCT). The image was reconstructed using the 3D-OSEM with 32 iterations and 4 subsets. The normalization, attenuation correction, and random correction were applied.

3. Results and discussion

3.1 Physical performance

In each flood histogram of detector blocks, the 365 (14×14 + 13×13) crystals were well resolved. The average energy resolutions were 10.7 ± 0.6% and 11.1 ± 1.5% for the upper and lower layer crystals, respectively. The representative results of a detector block are shown in Fig. 3.
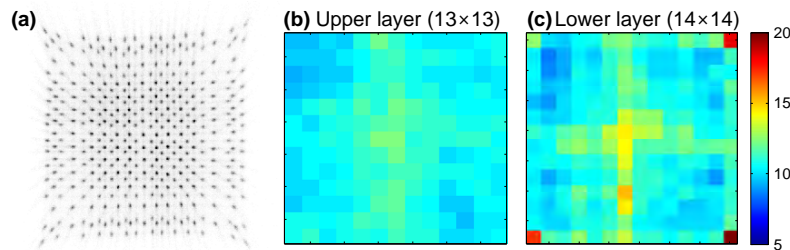
Figure 4. Representative flood map and two-dimensional histograms of energy resolutions of a detector block.

3.2 Phantom studies

The reconstructed Hoffman brain phantom images are shown in Fig. 4. In the mCT64 scanner, spatial resolution was greatly improved by applying PSF modeling (Figs. 4(b) and 4(c)). However, the detailed structures (e.g., the gyri in the occipital cortex) can be observed with less edge artifacts from the image acquired using the developed scanner even without applying PSF and TOF reconstruction.
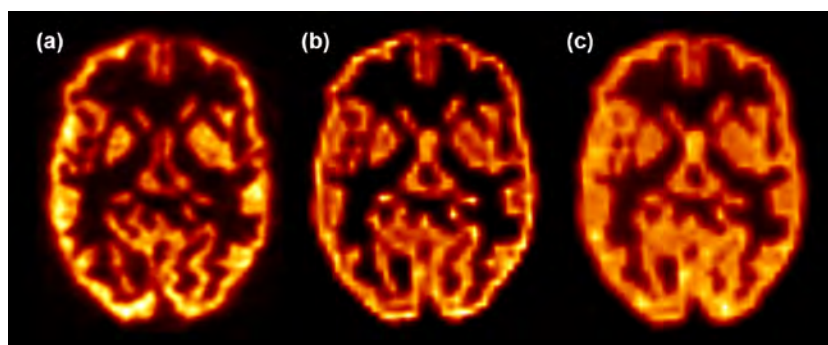
Figure 5. The reconstructed Hoffman brain phantom images. (a) The developed brain PET scanner (no PSF + no TOF), (b) mCT64 (PSF + TOF), and (c) mCT64 (TOF only).

4. Conclusion

A prototype brain PET scanner was developed based on a time-based digitizer and FPGA-based DAQ systems. The developed PET scanner showed promising results of resolving detailed structures of phantoms without edge artifacts.

Acknowledgments

References

[1]   J. Y. Won, S. I. Kwon, H. S. Yoon, G. B. Ko, J.-W. Son, and J. S. Lee, "Dual-phase tapped-delay line time-to-digital converter with on-the-fly calibration implemented in 40nm FPGA," *IEEE Trans. Biomed. Circuits Syst.*, vol. 10, no. 1, pp. 231–242, 2016.

[2]   J.-W. Son, J. Y. Won, and J. S. Lee, "Evaluation of a FPGA-based real-time coincidence module for high count rate PET scanners," *IEEE Nucl. Sci. Symp. Med. Imaging Conf.*, 2017.

[3]   G. B. Ko, K. Y. Kim, H. S. Yoon, M. S. Lee, J.-W. Son, H. J. Im, and J. S. Lee, "Evaluation of a silicon photomultipler PET insert for simultaneous PET and MR imaging," *Med. Phys.*, vol. 43, no. 1, pp. 72–83, 2016.

Basic performance evaluation of a helmet-type PET prototype with four-layer DOI detectors

Go Akamatsu[1], Hideaki Tashima[1], Yuma Iwao[1], Hidekatsu Wakizaka[1], Takamasa Maeda[1], Taichi Yamashita[2], Eiji Yoshida[1] and Taiga Yamaya[1]

[1] National Institute of Radiological Sciences (NIRS-QST), Japan

[2] ATOX Co. Ltd., Japan

Abstract

To fulfill a growing demand for a brain PET imaging with high-resolution and high-sensitivity, we are developing a brain-dedicated helmet-type PET scanner with 4-layer depth-of-interaction detectors. In this study, we evaluated the basic performance, such as spatial resolution, sensitivity and image quality, of the helmet-type PET prototype. As a result, the helmet-type PET prototype exhibited great sensitivity and high spatial resolution. For the image quality evaluation, the 10-mm hot sphere could be clearly visualized. We confirmed the high performance of the helmet-type PET prototype with 4-layer DOI detectors.

1. Introduction

  Brain PET imaging plays important roles in dementia diagnosis, neuro-oncology and molecular imaging research[1,2]. There is a growing demand for a PET scanner with high-resolution and high-sensitivity to achieve more accurate brain imaging. Therefore, we have developed a brain-dedicated helmet-type PET prototype with 4-layer depth-of-interaction (DOI) detectors[3]. To realize clinical applications and commercialization of helmet-type PET scanners, we have to objectively evaluate the basic performance of the prototype. In this study, we evaluated the basic performance of the helmet-type PET prototype.

2. Methods

2.1 Specifications of the Helmet-type PET prototype

  Fig. 1 shows the photograph and the detector arrangement of the helmet-type PET prototype. The scintillation crystal is a Zr-doped GSO and the photodetector is a 64-ch flat panel PMT. Each detector block has a $16 \times 16 \times 4$ crystal array (4 layers) with dimensions of $2.8 \times 2.8 \times 7.5$ mm^3. The total number of the detector block is 54. The energy window is 400-600 keV and the coincidence time window is 20 ns.
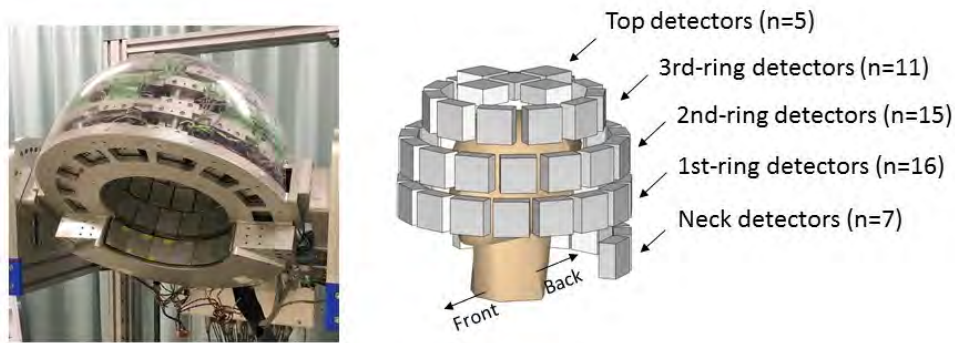
Figure 1. Photograph (left) and illustration (right) of the helmet-type PET prototype.

2.2 Performance evaluation

The performance evaluation consists of spatial resolution, sensitivity, and image quality. Fig. 2 shows the setup for each measurement. Spatial resolution was measured with a ^{22}Na point source. The source was successively positioned at center, 5 cm radial offset and 10 cm radial offset (if possible) in the axial center of each detector ring, respectively. The point source images were reconstructed with filtered back-projection. The average full width at half maximum (FWHM) of the point source images in all three directions was reported as the spatial resolution. Sensitivity was measured with the National Electrical Manufacturers Association (NEMA) sensitivity phantom according to the NEMA NU 2 standard. The source length was shortened compared with the NEMA procedure. For image quality evaluation, we newly developed the brain-size image quality phantom based on the NEMA NU 2 image quality phantom. This phantom has six spheres, of which diameters are 37, 28, 22, 17, 13 and 10 mm. The spheres with diameters of 37 and 28 mm were filled with non-radioactive water. Other spheres were filled with ^{18}F-solutions having a sphere-to-background radioactivity ratio of 4.
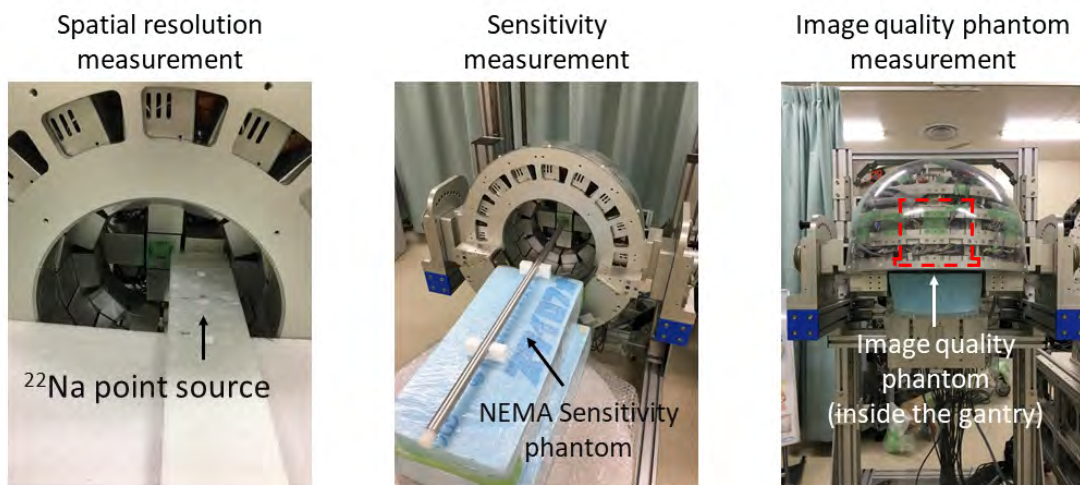
Figure 2. Setups for measurements of spatial resolution (left), sensitivity (center)
and image quality (right) of the helmet-type PET prototype.

3. Results

The spatial resolution was 3–4 mm. The system sensitivity was about 30 kcps/MBq. Figure 3 shows the PET image of the brain-size image quality phantom. The 10-mm hot sphere can be clearly visualized without any artifacts.
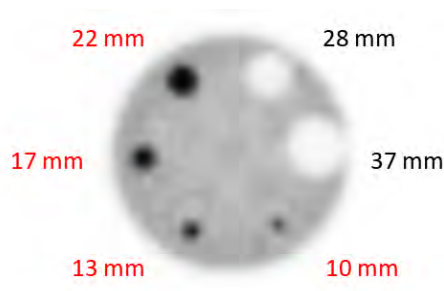
Figure 3. A PET image of the brain-size image quality phantom,
which was obtained by the helmet-type PET prototype.

4. Discussion

The helmet-type PET prototype showed high-resolution (3–4 mm) and high-sensitivity (about 30 kcps/MBq). These values are much better compared with those of recent introduced clinical time-of-flight PET/CT scanners (resolution: 4.1-5.1 mm, sensitivity: 5.7-9.7 kcps/MBq, from the review article[6]). For the image quality evaluation, the overall hot spheres can be visualized without any artifacts. The helmet-type PET prototype has the high potential to achieve high-performance brain PET imaging.

5. Conclusions

Our developed helmet-type PET prototype with 4-layer DOI detectors showed great sensitivity and high spatial resolution. We confirmed the high performance of the helmet-type PET prototype.

References

[1]   Phelps, M. E. PET: the merging of biology and imaging into molecular imaging. *J. Nucl. Med.* **41,** 661–681 (2000).

[2]   Silverman, D. H. *et al.* Positron emission tomography in evaluation of dementia: Regional brain metabolism and long-term outcome. *JAMA* **286,** 2120–2127 (2001).

[3]   Tashima, H. *et al.* Add-on detector position for the second helmet PET prototype: chin vs. neck. in *J. Nucl. Med.* **58,** 431–431.

[4]   NEMA Standards Publication NU 2-2018: performance measurements of positron emission tomographs. Rosslyn, VA: National Electrical Manufacturers Association; 2018. (2018).

[5]   NEMA standards publication NU 2-2012: performance measurements of positron emission tomographs. Rosslyn, VA: National Electrical Manufacturers Association; 2012. (2012).

[6]   Vandenberghe, S. et al. Recent developments in time-of-flight PET. *EJNMMI Phys.* **3,** 3 (2016).

Effect of inter-detector scatter recovery on performance of a brain-dedicated PET system

Seungeun Lee[1], Kyeong Yun Kim[1,2], Min Sun Lee[3] and Jae Sung Lee[1,2]

[1]Department of Nuclear Medicine, Seoul National University Hospital, Korea

[2]Brightonix Imaging Inc., Korea

[3]Molecular Imaging Program at Stanford, Division of Nuclear Medicine, Stanford University, USA

Abstract

Recovering inter-detector scatter (IDS) is one way to improve sensitivity of positron emission tomography (PET) system. We evaluated the effect of IDS recovery on performance of our newly developing brain-dedicated PET scanner with GATE Monte Carlo simulation. The scanner size was 33 cm in diameter and 10 cm in axial length, and the crystal block was composed of dual-layered LSO crystals with thickness of 8 mm and 12 mm. Sensitivities with and without IDS events were measured with a 70 cm rod source placed at the center and 6 cm off-center, varying the number of axial ring and energy windows for IDS events. We used proportional method for IDS recovery, which distributes the number of IDS events proportional to the number of recorded double coincidences along each LOR. To measure image quality, we imaged a brain-sized phantom with different size of hot and cold spheres. Adding IDS events achieved sensitivity of 8.55 kcps/MBq which was 16% higher than using only double coincidences. More IDS events were detected when the source was placed at off-center than center and when wider energy window for IDS was applied. Also, IDS more frequently occurred in scanners with longer axial field-of-view. In image quality analysis, sensitivity increase led to better background variability of hot and cold lesions by reducing statistical error. Contrast recovery coefficient slightly improved in both hot and cold lesions. We suggest that IDS recovery would be an effective way to improve both sensitivity and image quality of PET especially for PET scanners where IDS events are highly detected.

1. Introduction

Inter-detector scatter (IDS) is a type of triple coincidence in positron emission tomography (PET) scanners. IDS occurs by Compton scatter of one 511-keV annihilation photon from a detector block to another. Multiple coincidences are practically rejected because they do not specify the true line-of-responses (LORs). By adding accurately recovered IDS to double coincidences, we can improve sensitivity of PET. Portion of IDS events among total coincidences is highly dependent on scanner geometry: IDS more frequently occurs in the scanner with more compact arrangement of the crystal blocks, smaller-sized blocks, and larger number of blocks. In this study, we investigated effect of IDS recovery in our newly developing brain-dedicated PET scanner with Monte Carlo simulation. We measured sensitivity increase by adding recovered IDS events, and evaluated the impact of IDS recovery on image quality.

2. Methods

2.1. Brain PET scanner geometry

The simulated brain PET scanner had an axial field-of-view (FOV) of 10 cm and an inner diameter of 33 cm (Figure 1). The scanner was composed of 18 sectors in cylindrical arrangement, and each sector consisted of 2 (transaxial) $\times$ 4 (axial) LSO crystal blocks. A crystal block consisted of 11$\times$11 crystals in upper layer and 12$\times$12 crystals in lower layer, which were in dual-layered offset arrangement for depth-of-interaction (DOI) measurement. The sizes of the crystals were 2.09$\times$2.09$\times$8 mm^3 and 2.09$\times$2.09$\times$12 mm^3 in upper layer and lower layer, respectively.
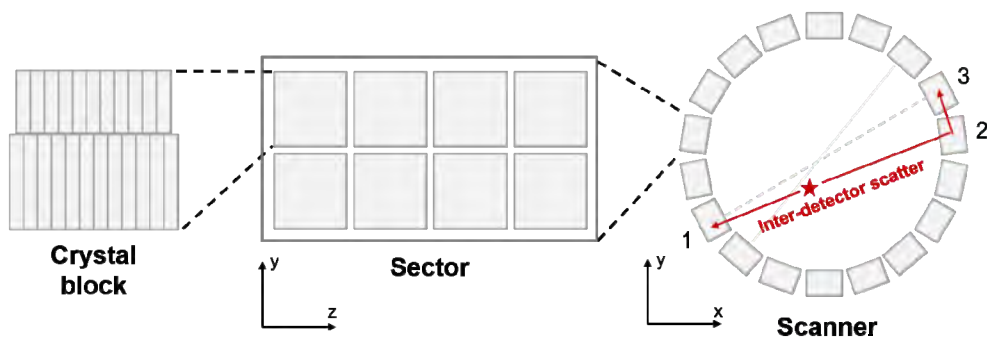
Figure 6. Hierarchy of the brain PET scanner geometry.

2.2. Simulation

We used a GATE Monte Carlo simulation toolkit (v7.0) to count the number of IDS events and apply IDS recovery for imaging. To measure sensitivity of the PET system, 70 cm rod source was placed at the center and 6 cm off-center of the scanner based on the method of NEMA NU2-2007 [1]. To investigate the effect of number of axial rings on the proportion of IDS events among total events, we additionally tested the sector of 2×6 and 2×8 crystal blocks, which cover the axial FOV of 15 cm and 20 cm, respectively.

To measure quality of IDS-recovered images, we designed a simple brain-sized phantom (Figure 2) based on NEMA IEC body phantom [1] and placed the phantom at the center of the scanner. The phantom was filled with water in a cylinder which had 150 mm in both diameter and axial length. To mimic human skull, the side and the top of the cylinder was covered with an 8 mm-thick material which had the same density to skull. 4 hot and 2 cold spheres with different sizes were placed in circle which had the diameter of 70 mm. The activity in the hot spheres was 4 times higher than the activity in the background region.

For the *digitizer* setting of the GATE, energy resolution of the scanner was 10%, and coincidence time window was 4 ns. From *Singles* files of the GATE output, we sorted the events with our customized coincidence logic and recorded the double and triple coincidences individually.
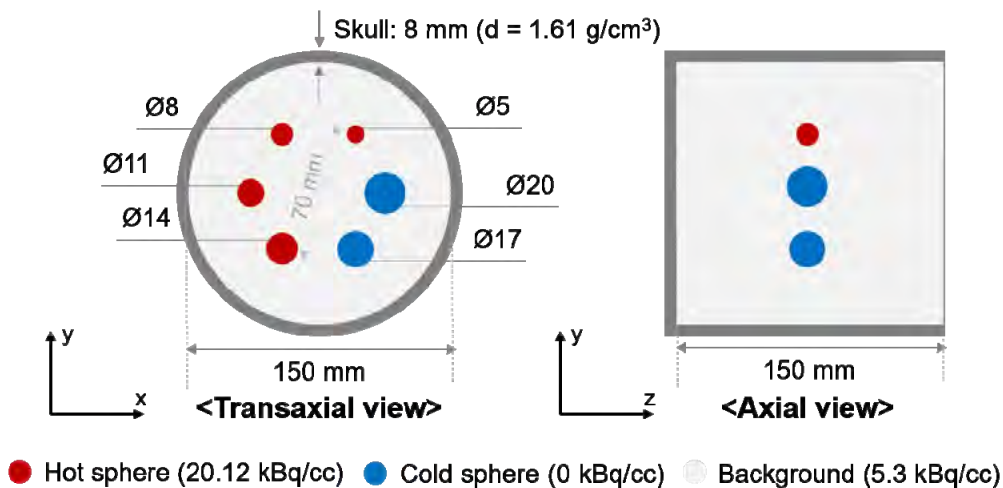
Figure 7. Simulated imaging phantom.

2.3. IDS recovery

We first determined whether the triple coincidences are IDS events by applying certain criteria. This is because triple coincidence contains random triple events and single photon with two scatters besides IDS events. If one deposited energy and sum of other two energies fall into an energy window, the event was assigned as an IDS event. We tested three different energy windows of [220, 750] keV, [350, 650] keV, and [400, 600] keV for IDS events. The energy window applied to double coincidences was [350, 650] keV.

To recover IDS events, we applied proportional method which yields the best performance in our knowledge. The proportional method distributes the number of IDS events proportionally to the number of

recorded double coincidences in LORs [2]. An example of IDS event is shown in Figure 1. When the counts of double coincidences were D_{1-2} and D_{1-3} along LOR_{1-2} and LOR_{1-3}, respectively, and the count of IDS events within these three detector blocks was T_{1-2-3}, the total counts of LOR_{1-2} and LOR_{1-3} are recorded as following:

$$Count_{1-2} = D_{1-2} + \frac{D_{1-2}}{D_{1-2} + D_{1-3}} T_{1-2-3}$$

$$Count_{1-3} = D_{1-3} + \frac{D_{1-3}}{D_{1-2} + D_{1-3}} T_{1-2-3}$$

2.4. Reconstruction and image quality analysis

We applied histogram-based ordered-subset expectation-maximization reconstruction to the phantom data. We compressed the LORs into a single layer to reduce data size and reconstruction time with preserving DOI information. We applied direct normalization with the normalization data from a uniform cylindrical source which emits 511 keV back-to-back gamma rays. Similar to NEMA NU2-2007 method, we measured contrast recovery coefficient (CRC) and background variability (BV) of the reconstructed images of the phantom [1] with increasing number of iterations from 1 to 5.

3. Results and discussion

3.1. Sensitivity

The results of sensitivity measurement are shown in Table 1. Sensitivity increase indicates the ratio of number of recovered IDS events to number of double coincidences. Without IDS recovery, sensitivity of our brain PET system was 7.38 kcps/MBq and 6.93 kcps/MBq when the rod source was place on the center and 6 cm off-center, respectively. With IDS recovery, applying wider energy window yielded higher sensitivity. The maximum sensitivity with IDS events was 8.55 kcps/MBq, which was 16% higher than the sensitivity without IDS events. Wider energy window resulted in higher increase in sensitivity because less IDS events were rejected.

Increasing the number of axial rings, sensitivity increase due to IDS recovery was higher. IDS took a large proportion of coincidence events in PET with longer axial FOV because IDS events with Compton scatter along axial direction are more highly detected. More IDS events were detected when the source was placed off-center than the center. This is because IDS events of scatter angles less than 90° are more likely to be detected from oblique LOR than LORs crossing the center, and cross-section of Compton scatter is higher for smaller angle.

TABLE 1. Sensitivity with and without IDS recovery in different energy windows for IDS events and different number of axial rings. The energy window for double coincidences was [350, 650] keV.

| Source position	Number of axial rings (Axial length)	Sensitivity w/o IDS recovery (kcps / MBq)	Sensitivity w IDS recovery (kcps / MBq) (%Sensitivity increase)		
			[220, 750] keV	[350, 650] keV	[400, 600] keV
Center	4 (10 cm)	7.38	8.55 (15.89%)	8.36 (13.32%)	8.35 (13.23%)
	6 (15 cm)	16.42	19.28 (17.43%)	18.86 (14.65%)	18.81 (14.56%)
	8 (20 cm)	28.61	33.91 (18.53%)	33.06 (15.54%)	33.03 (15.45%)
Off-center	4 (10 cm)	6.93	8.12 (17.30%)	7.93 (14.42%)	7.92 (14.33%)
	6 (15 cm)	15.45	18.25 (18.97%)	17.78 (15.89%)	17.78 (15.79%)
	8 (20 cm)	26.66	31.98 (20.17%)	31.10 (16.89%)	31.08 (16.79%)
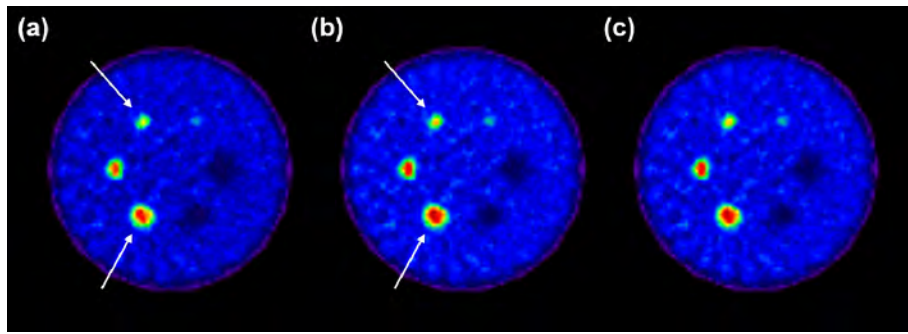
Figure 8. Reconstructed images of the phantom. (a) Without IDS, with IDS recovery applying energy window of (b) [220,750] keV, and (c) [400, 650] keV.
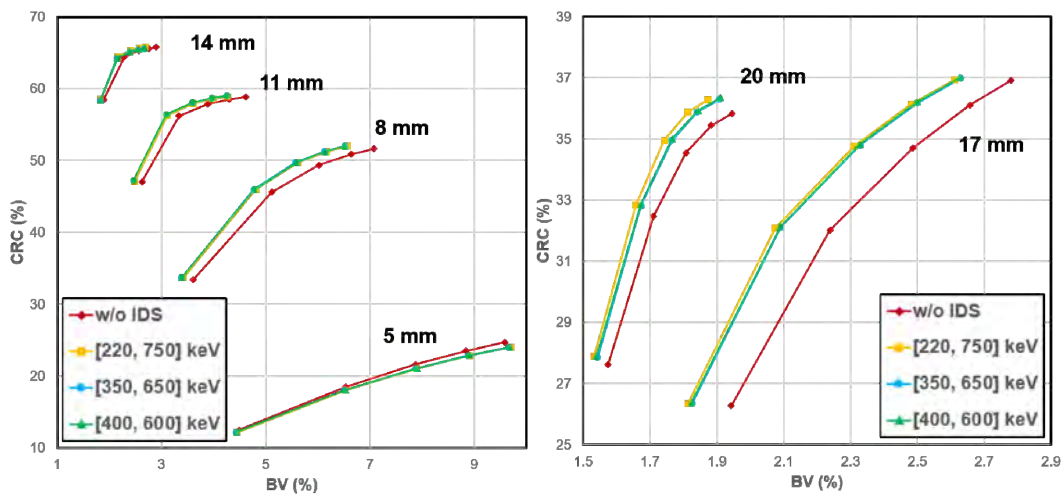

Figure 9. CRC vs. BV of the reconstructed images with and without IDS recovery with iteration numbers of 1 to 5. (a) Hot spheres (5, 8, 11, 14 mm), (b) cold spheres (17, 20 mm)

3.2. Image quality analysis

As shown in Figure 3, overall intensity increased when IDS recovery was implemented. Especially, hot spheres were more clearly shown, which implies the improvement of lesion detectability. Figure 4 shows that IDS recovery improved BV because increased counts of the LORs reduced statistical error. CRC was almost preserved or slightly improved especially in 20 mm cold sphere. However, there was a degradation in 5 mm sphere because only 5 pixels cover the region of interest, resulting susceptibility to image noise. Impact of IDS recovery on image quality is expected to be bigger in PET scanner geometry where the detector blocks are tightly packed or coincidence readout is available in smaller units, so as to detect more IDS events. There were insignificant differences in CRC and BV applying different energy windows because difference in sensitivity increase was less than 2%.

4. Conclusions

We investigated the effect of IDS recovery on sensitivity increase and image quality of our brain PET system. Compared to using only double coincidences, sensitivity increased up to 16% by adding recovered IDS events for reconstruction. As a result, IDS recovery improved CRC and BV of images. In PET systems where IDS event significantly occurs, IDS recovery would be an effective way to improve sensitivity and image quality.

References

[1] NEMA standards publication NU2-2007, Performance measurements of positron emission tomographs. Rosslyn, VA: National Electrical Manufacturers Association, 2007.

[2] Lage et al., Recovery and normalization of triple coincidences in PET, Med. Phys., vol. 42, no. 3, 2015.

Elimination of inter crystal scattering events for the X'tal cube

Munetaka Nitta[1,2], Fumihiko Nishikido[1], Naoko Inadama[1], Hideyuki Kawai[2] and Taiga Yamaya[1]

[1] National Institute of Radiological Sciences (NIRS-QST), Japan

[2] Chiba University, Japan

Abstract

The X'tal cube is PET detector composed of a monolithic scintillator block and multi pixel photon counter (MPPC) covering the scintillator. The 3D segmented array is fabricated in the scintillator by the laser engraving technique. We achieved almost isotropic sub-millimeter spatial resolution of the X'tal cube with segment size of $(0.77 \text{ mm})^3$. For the high spatial resolution PET detector, however, it is concerned that inter crystal scattering (ICS) events degraded the PET reconstruction image because ICS events provide mis-positon information. In this study, we developed the method to eliminate the ICS event. We used the information of difference of pulse height distribution of each MPPC between ICS event and the photo absorption event. For the photo absorption event at a segment, the pulse height distribution shows mean and standard deviation. On the other hand, the ICS event provides different pulse height of each MPPC from the photo absorption event, even if the result of the Anger calculation is the same. We used the reduced chi-square value and set the threshold to estimate if the detected event is ICS event or not. We carried out the scanning experiment to evaluate the response function of the X'tal cube and applied our proposal method. At the central area of the X'tal cube, the ICS event was seen as the long tail component with width of around 4 mm in the response function. By eliminating the ICS events, the ICS tail component was half. Our proposal method eliminated the ICS events efficiently.

1. Introduction

We have developed the X'tal cube. The X'tal cube is PET detector composed of a monolithic scintillator block and multi pixel photon counter (MPPC) covering the scintillator. The 3D segmented array is fabricated in the scintillator by the laser engraving technique. We achieved almost isotropic sub-millimeter spatial resolution by the X'tal cube with segment size of $(0.77 \text{ mm})^{3\,[1]}$. For the high spatial resolution PET detector, however, it is concerned that inter crystal scattering (ICS) events are noise events and degrade the PET reconstruction image because ICS events provide mis-positon information [2]-[5]. Figures 1 show schematic illustrations that an ICS event provides mis-positioning. Results of the Anger-type calculation were the same but the pulse height of each photo detector differed between (a) the photoelectric event and (b) the ICS event. In this study, we developed the method to eliminate the ICS event.

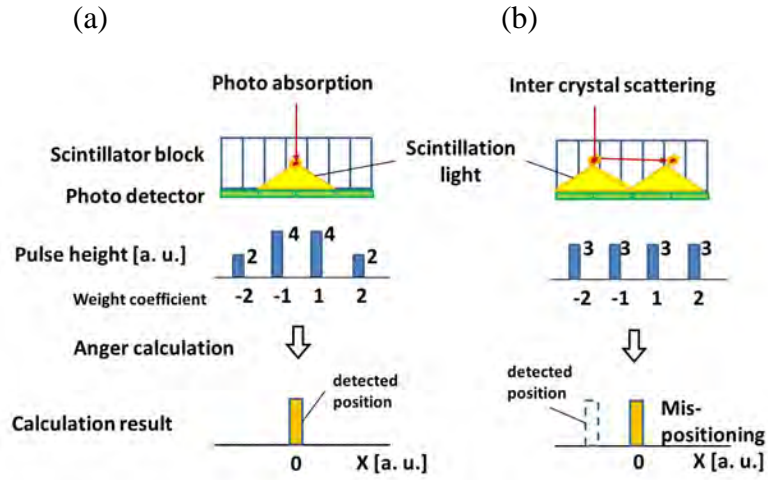(a)   (b)

Figure 1 Schematic illustrations showing that an ICS event brings about mis-positioning. Results of the Anger-type calculation were the same but the pulse height of each photo detector differed between (a) the photoelectric event and (b) the ICS event.

2. Material and methods

2.1 X'tal cube

Figure 2 (a) shows the configuration of the X'tal cube. We prepared the X'tal cube with the LYSO crystal block having a size of $(13.1 \text{ mm})^3$. Six multi pixel photon counter (MPPC) arrays of 4 x 4 (S12642-0404PB-50, Hamamatsu Photonics K.K., Japan) were coupled on six surfaces of the scintillator block. Sensitive area of each MPPC was $(3.0 \text{ mm})^2$. The scintillator block had 3D segmentation in the 17 x 17 x 17 array obtained using the laser process developed by Hamamatsu Photonics K.K [6]. The scintillator block segment size was $(0.77 \text{ mm})^3$. Detection position of a gamma-ray was determined by the 3D Anger-type calculation with 96 MPPC signals. Each segment response in the 3D position histogram corresponded to the detection segment of the X'tal cube.

2.2 Method to discriminate the ICS events

1) Setting threshold for chi-square value of signal

The photo absorption event at a segment (x, y, z) provides the mean value m_{ixyz} and the standard deviation σ_{ixyz}, for the i-th MPPC pulse height distribution. To discriminate the ICS events detected at the segment of (x, y, z), we calculated the chi-square value χ_{xyz}^2 for each event by formula (1)

$$\chi_{xyz}^2 = \sum_{i=1}^{n} (\frac{s_i - m_{ixyz}}{\sigma_{ixyz}})^2 \tag{1}$$

where n is the number of signal readouts used for the calculation. Then we set the threshold value k for the reduced chi-square χ^2/n to eliminate the ICS events as follows.

$$\chi_{xyz}^2 / n < k \tag{2}$$

2) Method to obtain the parameters for the chi-square

To obtain the values of m_{ixyz} and σ_{ixyz} for each segment, we irradiated 511 keV gamma-rays onto the X'tal cube uniformly. Then we obtained the 3D position histogram and set the region of interest (ROI) of one segment response for the segment (x, y, z) and obtained the distribution of each MPPC pulse height. We measured m_{ixyz} and σ_{ixyz} of a peak in the i-th MPPC pulse height distribution by fitting the peak and ICS distributions with the Gaussian function. When the photo absorption event occurs at a segment of the X'tal cube, pulse height s_i would be close to m_{ixyz} for all MPPC outputs and the value of χ^2/n is calculated as around 1. In the case of the ICS events, s_i tends to differ from the value of m_{ixyz} therefore the value of χ^2/n for the ICS events tends to be larger than 1.

2.3 Experiment

Both the uniform irradiation and the scanning experiment were carried out. We obtained a table of the values of m_{ixyz} and σ_{ixyz} by the uniform irradiation experiment of 511 keV gamma-rays from ^{22}Na sources. Then we carried out a fan-beam scanning irradiation experiment to make response functions (RFs) for evaluation of our method. Figure 2 (b) shows the setup of the scanning experiment. A ^{22}Na source was set between a lead a collimator with a slit of 0.2 mm width and a collimator with a slit of 1.0 mm width. The X'tal cube on a moving stage was set in front of the 0.2 mm slit collimator. A BaF$_2$ coincidence detector was set in front of the 1.0 mm slit collimator. Scan pitch of the stage was 0.2 mm. We obtained data for 30 minutes at each offset position. We drew the RFs by counting the events in the ROI corresponding to the segment to be evaluated for each scan position.

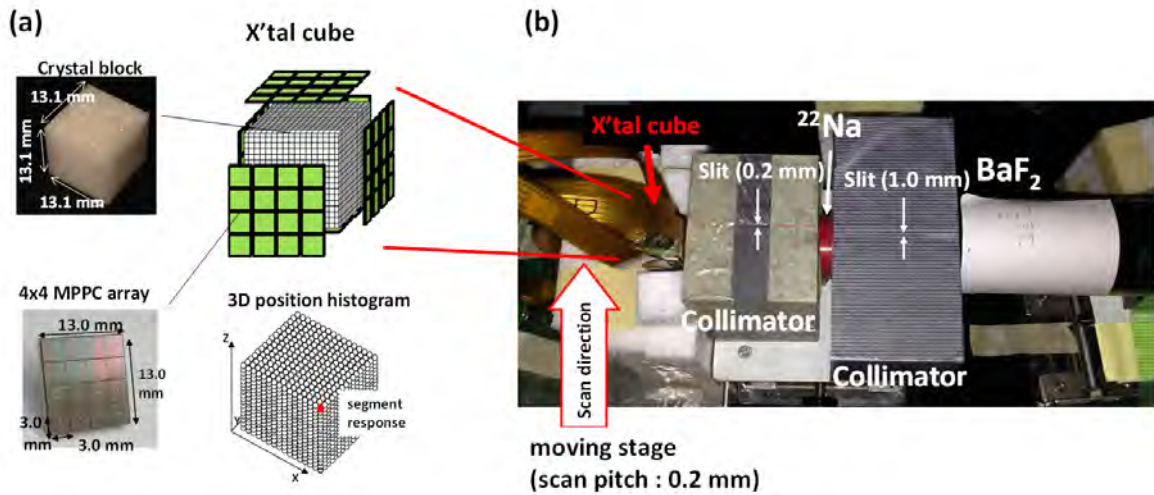Figure 2 (a) configuration of the X'tal cube. (b) Setup of the fan-beam scanning experiment.

3. **Results**

Figure 3 (a) shows 4 MPPC pulse height distributions of 511 keV photo peak events of the central segment response $(x, y, z) = (9, 9, 9)$ as an example. Figure 3 (b) shows the distribution of χ^2/n of the segment $(9, 9, 9)$. A peak was observed below 1 and the tail due to the ICS events was over 1. RFs of 17

segments $(x, z) = (9, 9)$ without and with the thresholds of 1 and 2 are shown in figure 3(c). Those RFs were fitted with two Gaussian functions and a constant. The first Gaussian component was for the true event component; the other Gaussian component was for the ICS background (BG) component and the constant was for the accidental BG events from the ^{176}Lu background [7] and the other environmental BG events. Dashed lines show the region of the segment width of 0.77 mm. Events plotted outside of this region can be considered as the ICS events. The zoomed response function of that region was also shown in the figure 3 (c). The ratio of ICS BG component in the response function without the threshold was 41 %. Table 1 shows RF FWHM, ICS BG FWHM and relative ICS BG area without and with the threshold. By decreasing the threshold, ICS BG FWHM and relative ICS BG area were improved. Over 50% of the ICS distribution of the RF was eliminated with threshold of 1. Then the distribution of ICS BG FWHM was improved from 4.01 mm to 2.07 mm.
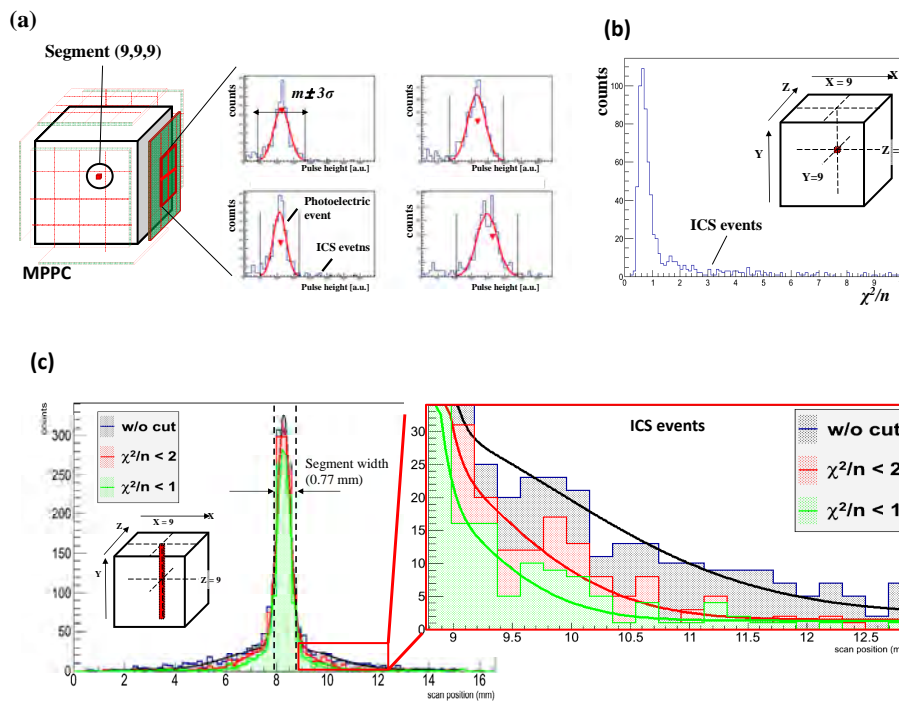
Figure 3(a) Pulse height distributions of 4 MPPCs for 511 keV photo peak events at the segment (9, 9, 9) as an example. (b) The distribution of χ^2/n of the segment (9, 9, 9). (c) the response function of the raw of segments (x, z) = (9, 9) and zoomed response function of tail.

Table 1 RF FWHM, ICS BG FWHM and relative ICS BG area without and with some threshold value of χ^2/n for the RF.

Threshold	RF FWHM (mm)	ICS BG FWHM (mm)	Relative BG ICS area
$\chi^2/n < 1$	0.62	2.07	0.45
$\chi^2/n < 2$	0.65	2.64	0.66
No	0.66	4.01	1

4. Discussion and Conclusion

We proposed the method to discriminate ICS events and proved its feasibility using the X'tal cube with segment size of (0.77 mm)^3. We found that the ICS BG FWHM of 4.0 mm was observed at the central position of the X'tal cube. The ICS distribution was over 5 times wider than the size of the segment and might degrade the contrast of the PET image [5]. By setting the threshold value of 1 for χ^2/n, the distribution of ICS BG FWHM was improved to 2.1 mm and over 50% of the ICS component was eliminated. However, RF FWHM was hardly affected by the ICS event and consistent with the size of the segment. Our proposed method can eliminate the ICS events efficiently.

References

[1] M. Nitta, et al., The X'tal cube PET Detector of Isotropic from (0.8mm)^3 to (0.77mm)^3: Improved X'tal Cube PET Detector for Better Crystal Identification, IEEE NSS/MIC (2015), M4--22 San Diego USA

[2] S-J. Park, W. L. Rogers and N. H. Clinthorne, Effect of inter-crystal Compton scatter on efficiency and image noise in small animal PET module, Nuclear Science Symposium Conference Record IEEE, 4 (2003), 2272 – 2277.

[3] J. R Stickel and S. R Cherry High-resolution PET detector design: modelling components of intrinsic spatial resolution, Phys. Med. Biol., 50 (2005), 179–195.

[4] N. Ghazanfari, M.R. Ay, N. Zeraatkar, S. Sarkar, and G. Loudos, Quantitative assessment of the influence of crystal material and size on the inter crystal scattering and penetration effect in pixilated dual head small animal PET scanner, IFMBE Proceedings 35 (2011), 712-715.

[5] C. F. Lam, et al., An inter-crystal scatter correction method for DOI PET image reconstruction, Jpn. J. Med. Phys., 26 (2006), 118-130.

[6] T. Moriya, et al., Fabrication of finely pitched LYSO arrays using subsurface laser engraving technique with picosecond and nanosecond pulse lasers, IEEE Trans. Nucl. Sci., 61 (2014), 1032-1038.

[7] Melcher CL, J. Schweitzer S. Cerium-doped lutetium oxyorthosilicate: a fast, efficient new scintillator. IEEE Trans Nucl Sci 1992; 39: 502–505.

A hand-held ultra-low dose intraoperative x-ray imaging device for minimally invasive surgery

Haewook Park[1], Kook Nam Han[2], Byeong Hyeon Choi[2], Hyun Koo Kim[2] and Jae Sung Lee[1]

[1]Department of Nuclear Medicine, Seoul National University, Seoul, Korea.

[2]Department of Cardiovascular and Thoracic Surgery, Korea University, Seoul, Korea.

Abstract

In this study, we propose the novel concept of a hand-held intraoperative x-ray imaging device that can resolve the issues of radiation exposure and spatial constraint during the minimally invasive surgery. To demonstrate its feasibility, we performed an *in-vivo* intraoperative imaging using a 30 kg dog; and subsequently, an additional *ex-vivo* imaging study was performed after resecting the lung specimens to confirm the existence of the lung nodule. Also, we have measured a single-shot radiation dose of the proposed device by shooting and averaging the 10 consecutive x-rays under the fixed parameters: tube voltage of 40 kV, tube current of 2 mA, and the exposure time of 20 msec. As a result, we could successfully acquire the high-resolution x-ray images of the lung nodule, showing a remarkable contrast relative to the normal lung tissue with no use of any contrast agent. Moreover, we have shown that our developed device can considerably reduce the radiation exposure (i.e., 0.13 μGy) as compared with the fluoroscopy method (i.e., 5~70 mGy) while providing the real-time visualization of the lung nodules. We expect that our development has a potential to replace the C-arm based real-time lesion detecting method during the minimally invasive surgery, thereby achieving the radiation dose reduction to both surgeons and patients as well as resolving the problems of the operation room being cluttered by the bulky equipment.

Figure 1. Conceptual diagram of the proposed hand-held endoscope-type x-ray imaging device.

1. Introduction

As effective screening tests for early diagnosis of lung cancer are advanced, a minimally-invasive limited lung resection is more widely performed than before because it improves the life quality of patients. For the precise localization of the pulmonary nodule, Computed tomography (CT) guided percutaneous localization and bronchoscopic injection techniques are used [1]. However, the sensitivity of these

techniques is limited for the nodules less than 10 mm, for which the definitive diagnosis is only possible through the surgical operation and the pulmonary nodule excision. Therefore, C-arm fluoroscopy with a contrast agent (e.g., lipiodol) is now performed for better visualization of resection margin of lung nodules. However, the C-arm fluoroscopy has several limitations including the excessive radiation exposure to the medical staffs and the large space occupancy around the surgical table. In this study, we propose the novel concept of a hand-held intraoperative x-ray imaging device that reduces radiation exposure and resolves spatial constraint. This endoscope-type device was designed for the high-resolution real-time x-ray snap-shot imaging during the minimally invasive surgery (figure 1).

2. Materials and Methods

2.1 Mechanical Design

Figure 2(a) illustrates a mechanical design of the proposed intraoperative x-ray imaging device. Both clamp body and manipulator body were made of acetal-based plastic, while the outer rod body and the inner rod body was made of aluminum and the steel, respectively. Figure 2(b) shows the detail of the imaging module that consists of the following three parts:
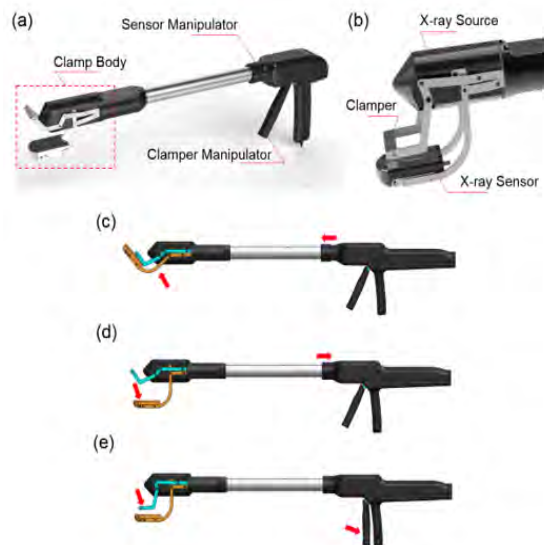

Figure 2. Mechanical design of the proposed intraoperative x-ray imaging device.
(a) Overall view, (b) Magnified view of clamp body. There are three operation modes: (c) Insert-mode, (d) Ready-mode, (e) Image-mode.

Figures 2(c)-2(e) shows the step-by-step operation procedures. The x-ray device is inserted into the human body, as shown in figure 2(c) (insert-mode). Thereafter, the x-ray emission module and the x-ray sensing module are spaced from each other by pulling the sensor manipulator inside the human body, as shown in figure 2(d) (ready-mode). If a lesion is well-positioned by adjusting the clamper manipulator, as shown in figure 2(e) (image-mode), then the x-ray is emitted from the x-ray emission module and sensed by the x-ray sensing module by triggering an external switch.

2.2 Radiation Dose Measurement

For the dose measurement, absorbed radiation dose was measured using a calibrated radiation dosimeter (RaySafe X2, RaySafe, Sweden) while operating the proposed device. The dosimeter was located a one-meter apart from the focal spot of the x-ray source. To obtain a single-shot radiation dose, we shot and averaged 10 consecutive x-rays under the fixed parameters: tube voltage of 40 kVp, tube current of 2 mA, and the exposure time of 20 msec.

2.3 Intraoperative Imaging Study Using a Lung Nodule Model

Furthermore, we have performed an *in-vivo* intraoperative animal imaging study using a 30 kg dog, as shown in figure 3. The developed device was inserted through a 6-cm-wide port. In order to simulate the pulmonary nodule of the cancer patient, the artificial lung nodule model was created based on agar-powder and subsequently injected into the collapsed lung of the anesthetized dog. The intraoperative imaging was conducted during the experiment to see whether the artificial lung nodule can be clearly visualized by the proposed x-ray device. Subsequently, the lung specimens were resected, and an additional *ex-vivo* imaging study was performed to confirm the existence of the agar-model of lung nodule.

3. Results

In the radiation dose measurement, our proposed device yielded an ultra-low radiation dose of 0.13 μGy per single shot, which is approximately 1,000 times smaller than the amount measured in typical chest radiography.

In the intraoperative *in-vivo* and *ex-vivo* lung nodule imaging studies, we could successfully acquire the high-resolution x-ray images of the artificial lung nodule, showing a remarkable contrast relative to the normal lung tissue with no use of any contrast agent (figures 3 and 4).

4. Conclusion and Outlook

In this work, we have introduced the novel concept of intraoperative x-ray imaging, and have demonstrated its feasibility by performing the *in-vivo* and *ex-vivo* x-ray imaging study. Moreover, we have shown that our developed device can considerably reduce the radiation exposure as compared with the fluoroscopy method (i.e., 5~70 mGy) while providing the real-time visualization of the lung nodules [3]. Therefore, we expect that our development has a potential to replace the C-arm based real-time lesion detecting method during the minimally invasive surgery, thereby achieving the radiation dose reduction to both surgeons and patients as well as resolving the problems of the operation room being cluttered by the bulky equipment.

We are planning to perform an additional *ex-vivo* imaging study of the pulmonary nodules resected from the cancer patients as a future work to further demonstrate the usefulness of our proposed device as well as comparing the image quality with and without injecting the contrast agent.
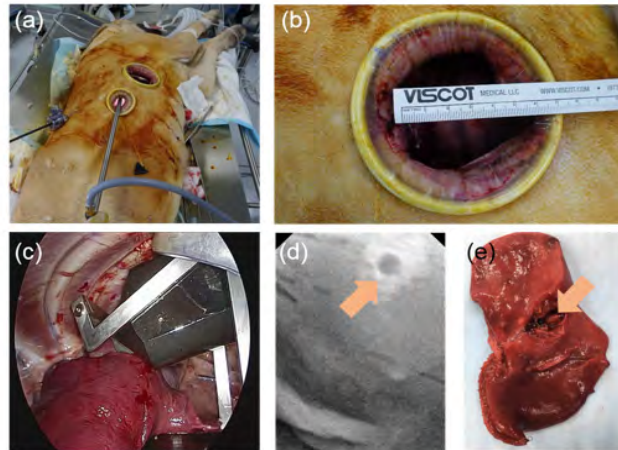
Figure 3. In-vivo intraoperative imaging study. (a) An anesthetized 30-kg-weight dog. (b) The 6-cm-wide port for inserting the developed device. (c) Intraoperative view of the developed x-ray imaging device during the surgical operation. (d) X-ray snap-shot image. (e) Resected specimen.
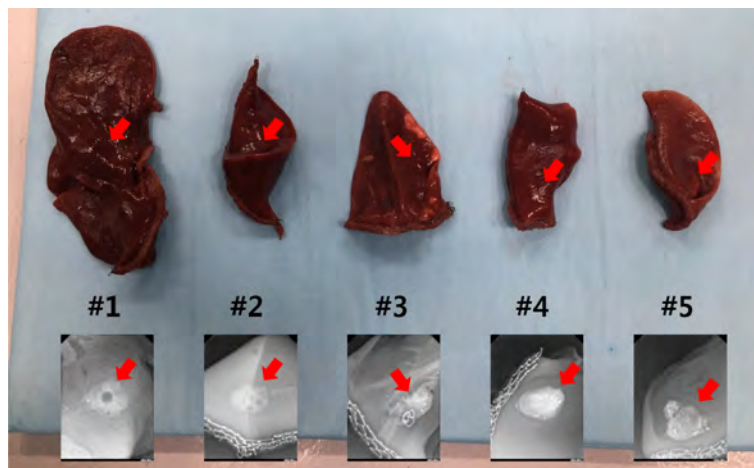
Figure 4. Samples from ex-vivo x-ray imaging study.

References

[1] S. Welter et al., "A new technique for complete intraluminal repair of iatrogenic posterior tracheal lacerations", *Interact. Thorac. Cardiovasc. Surg.,* 2011.

[2] T. F. Molnar et al., "What are the considerations in the surgical approach in pulmonary metastasectomy", *J. Thorac. Oncol.,* 2010.

[3] E. L. Nickoloff et al., "Radiation doses during CT fluoroscopy", *Health. Phys.,* 2000.

Evaluation of time-of-flight PET detector using LFS with 10 mm length and MPPC module

Sodai Takyu[1], Eiji Yoshida[1], Fumihiko Nishikido[1], Hideaki Tashima[1] and Taiga Yamaya[1]

[1] National Institute of Radiological Sciences (NIRS-QST), Japan

Abstract

A new TOF PET detector module which consists of 4.1 mm sized LFS scintillators and multi pixel photon counters (MPPCs) is now commercially available (C13500-4075LC-12, Hamamatsu Photonics K.K.). In this paper, we fabricated a one-pair prototype of the TOF PET detectors based on the TOF PET detector module and evaluated its basic performance. We obtained the averaged energy resolution of 11.7 ± 0.7 % at 511 keV after energy correction and the averaged CRT value of 250 ± 8 ps FWHM in 144 channels.

1. Introduction

PET images are reconstructed assuming that a radioactive source exists on the line connecting a detector pair which has detected annihilation gamma rays in coincidence. A performance index to indicate the accuracy to determine the 'coincidence' is defined as 'time resolution'. A good time resolution improves the signal-to-noise ratio of the PET images by the effect of using TOF information and by the reduction of random coincidence [1]. A new TOF PET detector module which consists of 4.1 mm sized LFS scintillators and multi pixel photon counters (MPPCs) is now commercially available (C13500-4075LC-12, Hamamatsu Photonics K.K.) [2]. In this paper, we fabricated a one-pair prototype of the TOF PET detectors based on the TOF PET detector module and evaluated its basic performance.

2. Material and methods

The TOF PET detector module has a 12×12 array of the MPPCs each coupled to a 4.1×4.1×20 mm^3 LFS crystal scintillator in a one-to-one manner according to the catalog specifications. Although the module does not have DOI detection capability, a 280 ps coincidence resolving time (CRT) is available. The module processes all readout signals by circuits behind the detector as shown in Figure 1 a) and gathers the energy, timing, and position information as a list-mode data format. The size of each MPPC is 4×4 mm^2 with 75 µm pitch and 12×12 channels.

In this study, the 12×12 array of 4×4×10 mm^3 LFS scintillators were optically connected to the MPPC channels in a one-to-one manner. For energy correction, a relationship between gamma ray energy and the pulse height (analog-to-digital-converter (ADC) channel) was investigated using point sources with different energies (^{22}Na, ^{137}Cs, ^{152}Eu, ^{176}Lu, ^{54}Mn and ^{133}Ba). After energy correction, the averaged energy resolution at 511 keV in 144 channels was calculated. Then, those two detectors were oppositely placed with a 12 cm distance between them. A ^{22}Na point source (1.5 MBq) was placed at the center and the coincidence measurement was performed for 10 minutes (Figure 1 a)). After coincidence processing, time

resolution of each MPPC channel was obtained as the full width at the half maximum in the spectrum of the time differences in the measured coincidence data. The energy window of 450 to 580 keV was applied.

3. Results and discussion

As a result of investigation of relationship between gamma ray energy and the ADC channel, linearity degradation due to the MPPC saturation was seen. Therefore, we carried out energy correction. The averaged energy resolution at 511 keV after the energy correction was 11.7 ± 0.7 %. Figure 1 b) shows the 2D-distribution of CRT values. The averaged CRT value in 144 channels was 250 ± 8 ps FWHM, which was 30 ps better than 280 ps which is the catalog specifications using LFS scintillator with the crystal size of $4.1 \times 4.1 \times 20$ mm^3. The reason for the difference was presumed to be that the average optical path length of photons reaching the MPPC surface became shorter as the crystal length became shorter.
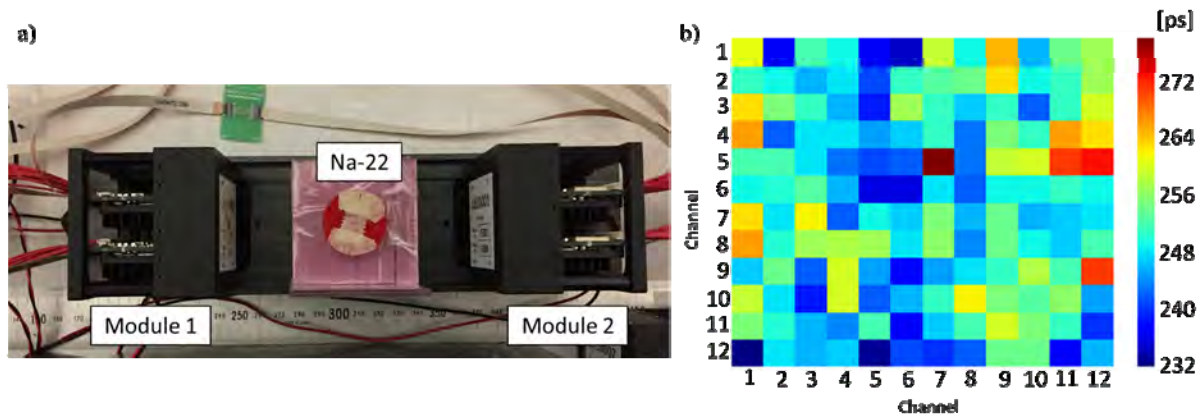

Figure 1. A photo of the experimental setup (a) and the 2D-distribution of CRT values (b).

4. Conclusions

We evaluated performance of a one-pair prototype of the TOF PET detectors using the new MPPC module (C13500 series) and obtained an excellent timing resolution of 250-ps CRT.

Acknowledgments

References

[1]   S. Vandenberghe, et al., "Recent developments in time-of-flight PET," EJNMMI Physics, vol. 3, no.3, pp. 1-30, 2016.

[2]   http://www.hamamatsu.com/jp/en/community/mppc/4411.html.

Three Dimensional Inpainting of Brain MRI Using Deep Neural Networks

Seung Kwan Kang[1], Seong A Shin[1], and Jae Sung Lee[1]

[1] Seoul National University, Seoul, Korea

Abstract

We propose a deep-learning based inpaiting technology that allows the generation of 3D MR images from more sparsely acquired 2D images. The convolutional neural network consisted of 3D operations whose architecture followed the mixture of DenseNet and Unet. We observed that anatomical details in brain cortices and ventricles are well recovered by the neural network. Both the quantitative and qualitative evaluation shows that the proposed method outperforms the linear interpolation in terms of the similarity in the inpainted images and segmented tissue probability maps as the original 3D MRI

1. Introduction

Anatomical details provided by T1-weighted magnetic resonance imaging (MRI) with high resolution three-dimensional (3D) sequences allow a wide range of brain imaging research including the quantitative measurements of brain tissue volume and cortical thickness. However, since longer scan times and greater data storage are required for 3D sequences, 2D MR images are conventionally obtained for the purpose of diagnostic utility in everyday clinical practice. This may hinder adoption of various advanced techniques for research purposes when working with clinical data. Therefore, in this study, we propose a deep-learning based inpaiting technology that allows the generation of 3D MR images from more sparsely acquired 2D images.

2. Methods

2.1 Convolutional Neural Network

Inspired by the previous works on classification problem, we borrowed the idea from DensetNet [1] architecture to improve the performance of network. DenseNet preserves the features of previous layer by concatenating every passing layer. It can be expressed by:

$$x_l = H_l([x_0, x_1, \ldots, x_{l-1}])$$ (1)

where represents the feature map of ith layer and H_l the composition of activation function and normalization operation such as batch normalization. We call these concatenated layers as a dense block. At the end of the dense block, the transition layer sub-samples the image with strided ($2\times2\times2$) convolution.

The features from dense blocks in convolutional stage are concatenated with deconvolution dense blocks to yield better backpropagation of gradients. This architecture is also similar with well-known network, called U-net [2]. Figure 1 shows the detail structure of network architecture employed in this research.
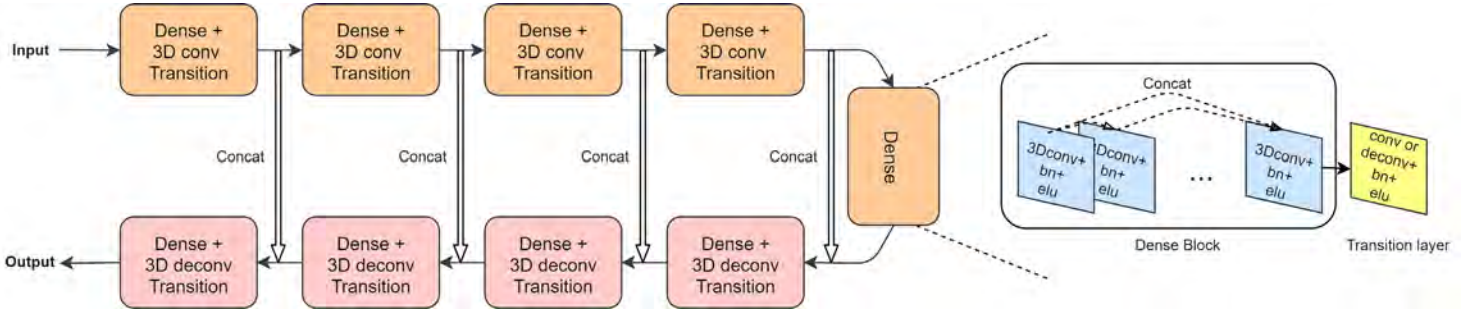
Figure 10. Network architecture.

2.2 Datasets and Training Details

Six hundred and eighty-one T1-weighted 3D MRI scans obtained in the Korean Brain Aging Study for Early Diagnosis and Prediction of Alzheimer 's Disease (KBASE) were used to train and test the deep neural networks. A T1-weighted 3D ultrafast gradient echo sequence was also obtained in a $208 \times 256 \times 256$ matrix with voxel sizes of $1.0 \times 0.98 \times 0.98$ mm. Of the 681 datasets, 527 were used to train the neural networks and the other 154 to validate the trained networks.

The used batch size m was 12, and the total number of training patch was 439,479. The AMSgrad that can correct for the non-converging property of ADAM algorithm was used for minimizing the given loss function. The initial learning rate was 0.0003, which were decayed 1/10 after 20 epochs. We trained our network for 60 epochs.

2.3 Evaluations

For the test data set, we calculated peak to signal ratio (PSNR) and structural similarity (SSIM) within the brain region using the mask obtained from the BET:

$$\text{PSNR} = 10 \log_{10}\left(\frac{MAX_I^2}{MSE}\right), \quad \text{SSIM} = \frac{(2\mu_x\mu_y + c_1)(2\sigma_{xy} + c_2)}{(\mu_x^2 + \mu_y^2 + c_1)(\sigma_x^2 + \sigma_y^2 + c_2)} \tag{2}$$

where μ and σ are mean and variance or covariance of two images, respectively. We calculated both metrics in coronal and sagittal planes.

We also performed segmentation of brain tissues for three data sets (original 3D MRI and 3D MRI recovered from 2D MRI using proposed neural network and linear interpolation) using SPM 12. The SPM 12 provided the tissue probability maps of gray matter (GM), white matter (WM), and cerebrospinal fluid (CSF).
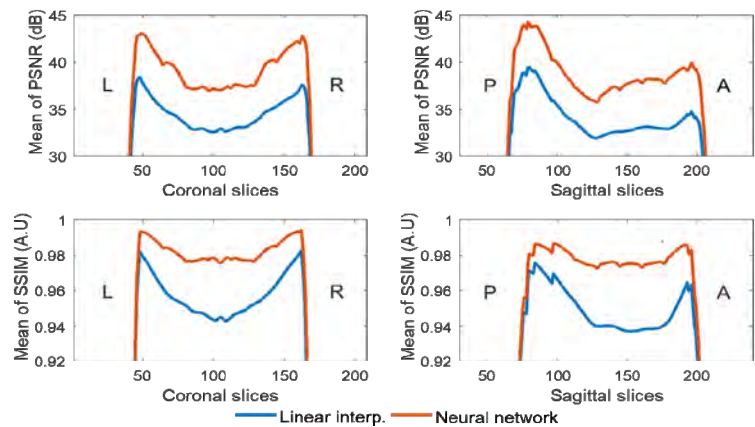

Figure 2. Mean of PSNR and SSIM for test set.

3.   Results and Discussion

The Figure 2 shows the plots of the PSNR and SSIM along the coronal and sagittal slices. Both metrics show that the proposed neural network yielded more similar images as the 3D MRI than conventional linear interpolation.

The Figure 3a shows the coronal and sagittal images and GM tissue probability maps segmented from them. The mean squared errors between the inpainted and original 3D MRIs for the different tissue probability maps are shown in Figure 3b that also indicates that proposed method outperforms the linear interpolation. It is also notable that the noise level in the neural network output was lower than original 3D MRI.
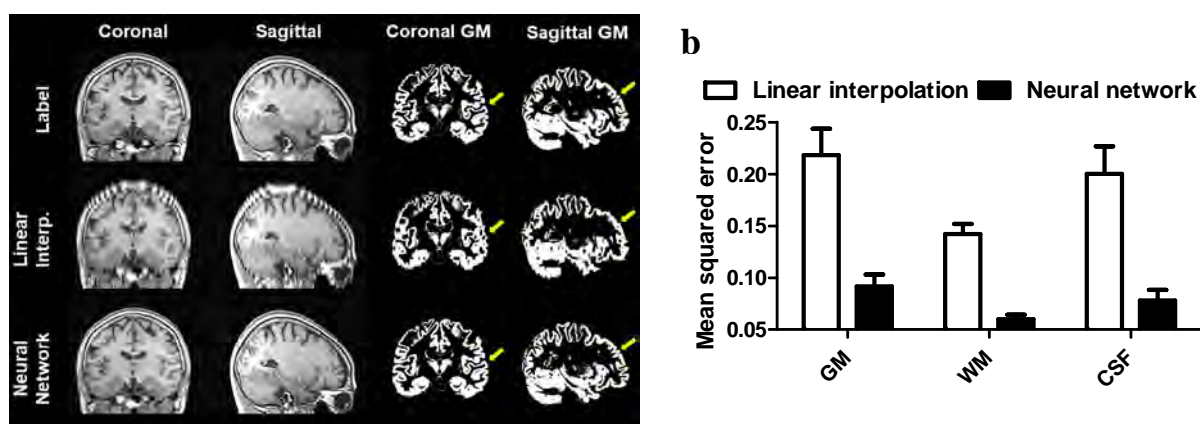

Figure 3. **a**. Coronal and sagittal view with the result of segmentations. **b**. Mean squared calculation for obtained tissue probability maps (GM, WM and CSF).

4.   Conclusions

In this study, we proposed a deep neural network to produce inpainted 3D MR images from the intermittently sampled 2D MR images. Patch-based training the network was performed using large-sized data set (439,479 patches) by simultaneously minimizing and content and perceptual loss. Both the quantitative and qualitative evaluation shows that the proposed method outperforms the linear interpolation in terms of the similarity in the inpainted images and segmented tissue probability maps as the original 3D MRI

References

[1]   Huang, Gao, et al. "Densely connected convolutional networks." Proceedings of the IEEE conference on computer vision and pattern recognition. Vol. 1. No. 2. 2017.

[2]   Ronneberger, Olaf, Philipp Fischer, and Thomas Brox. "U-net: Convolutional networks for biomedical image segmentation." International Conference on Medical image computing and computer-assisted intervention. Springer, Cham, 2015.

[3]   Johnson, Justin, Alexandre Alahi, and Li Fei-Fei. "Perceptual losses for real-time style transfer and super-resolution." European Conference on Computer Vision. Springer, Cham, 2016

Detector response modeling for β+-γ emitter imaging of the whole gamma imager

Hideaki Tashima[1], Eiji Yoshida[1], Yusuke Okumura[2,1], Mikio Suga[2], Naoki Kawachi[3], Kei Kamada[4], Katia Parodi[5] and Taiga Yamaya[1]

[1] National Institute of Radiological Sciences (NIRS-QST), Japan

[2] Chiba University, Japan

[3] Takasaki Advanced Radiation Research Institute (Takasaki-QST), Japan

[4] C&A Corporation, Japan

[5] Ludwig-Maximilians-Universität München, Germany

Abstract

The whole gamma imaging (WGI) is our concept combining positron emission tomography (PET) and Compton imaging to utilize various radionuclides for imaging. The WGI is realized by inserting a scatterer ring into a PET detector ring so that the PET detector ring functions as an absorber detector. The β+-γ emitter imaging, which we also call 3-gamma imaging, is one of applications for the WGI. A β+-γ emitter such as ^{44}Sc emits a positron and a single gamma ray at almost the same time, resulting in emission of three gamma rays. Detecting the annihilation photons by the PET detector ring and the single gamma ray by the Compton imaging manner, we can identify the radionuclide position at the cross section of the line-of-response (LOR) and the Compton cone surface. In this study, we proposed a detector function model necessary for the 3-gamma imaging. We used the model to generate back projection image of a β+-γ emitter acquired by the first WGI prototype developed for a proof-of-concept. As a result, the image generated by the proposed model was clearer than that by LOR information only.

1. Introduction

We have proposed the whole gamma imaging (WGI) as a new concept of nuclear medicine instrumentation. The WGI is combining principles of the positron emission tomography (PET) and the Compton imaging. A scatterer ring is inserted into the conventional PET detector ring so that the PET detector ring works as an absorber detector of the Compton imaging as well. Realization of the WGI enables 1) sensitivity improvement for PET nuclides, 2) single photon emitter imaging, and 3) 3-gamma imaging [1, 2, 3] with one single system. The 3-gamma imaging targets β+-γ nuclides such as ^{44}Sc [4], which emits 1157 keV single gamma ray at almost the same time as the positron decay. In this study, we propose a detector response model necessary for the 3-gamma imaging of the WGI.

2. Methods

2.1 Detector response model of the 3-gamma imaging

PET detectors are arranged in a ring shape to measure the coincidence of two 511 keV pair gamma rays

emitted in opposite directions with the positron decay and annihilation, and the position of the radiation source is determined on the line (line-of-response: LOR) connecting two detection points. The distribution of the radiation sources is estimated by the principle of the tomographic image reconstruction using multiple LOR information. On the other hand, Compton imaging utilizes the energy and position information measured at both scatterer and absorber detectors. The position of the radiation source is determined on the surface of a cone (Compton cone) with the vertical axis connecting detection positions, the vertex at the detection position in the scatterer, and the half-cone angle equal to the scatter angle determined by the Klein-Nishina equation using the energy information. Let the energies measured at the scatterer and the absorber be E_s and E_a, respectively. The scatter angle θ can be expressed with the following equation:

$$\theta = \arccos\left(\left(\frac{1}{E_s + E_a} - \frac{1}{E_a}\right)m_e c^2 + 1\right), \tag{1}$$

where m_e is the mass of electron, c is the speed of light in vacuum. The 3-gamma imaging, which detects three gamma rays emitted from β^+-γ emitter, can determine the radiation source position on intersecting points of the LOR and the Compton cone. As shown in figure 1, let $\mathbf{c}$ and $\mathbf{c'}$ be the coincidence detection positions, $\mathbf{d}$ be the directional vector from $\mathbf{c}$ toward $\mathbf{c'}$, $\mathbf{s}$ be the detection point in the scatterer, $\mathbf{a}$ be the detection point in the absorber, $\mathbf{n}$ be the directional vector from $\mathbf{a}$ toward $\mathbf{s}$, and t be the distance between $\mathbf{c}$ and the intersection point $\mathbf{p}$ of the line and the cone surface. Then, $\mathbf{p}$ can be determined by solving following system of equations:

$$\begin{cases} \mathbf{p} = \mathbf{c} + t\mathbf{d} \\ \dfrac{(\mathbf{p} - \mathbf{s}) \cdot \mathbf{n}}{|\mathbf{p} - \mathbf{s}|} = \cos\theta \end{cases}. \tag{2}$$

We should note that the energy information acquired in actual situations contains errors depending on the energy resolution of the detectors; therefore, obtained scatter angle contains error as well. Therefore, our proposed detector response model includes blurring modeled as 2D Gaussian distribution on the LOR depending on the angular blurring of the cone. The deviation parameters σ_1, σ_2 of the 2D Gaussian distribution are given by the deviation of the solution of equation (2) with respect to t.
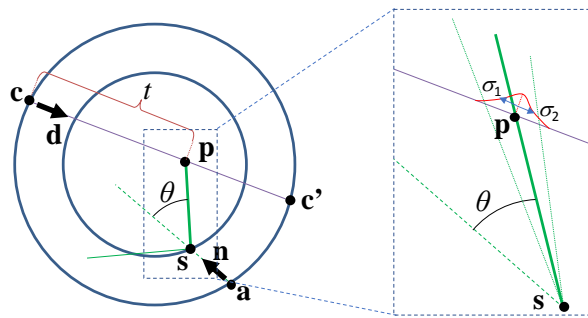

Figure 1. Detector response

2.2 Experiment

We generated a back-projection image of ^{22}Na data measured with our world's first WGI prototype for a proof of concept [5] by using the proposed detector response model. The image was compared that back projected using only the LOR information. The ^{22}Na is a β^+-γ emitter which emits 1275 keV single gamma ray simultaneously with the positron emission. Although the ^{22}Na cannot be used as a biological tracer due to its long half-life, we can use it for test source for system evaluation. We measured a point source of ^{22}Na placed at several offset from the center of the field-of-view for 120 min for each position.

3. Results

Figure 2 shows a WGI back projection image using the proposed detector response model and that using only LOR information for the same list-mode data set. The proposed model could generate clearer image.
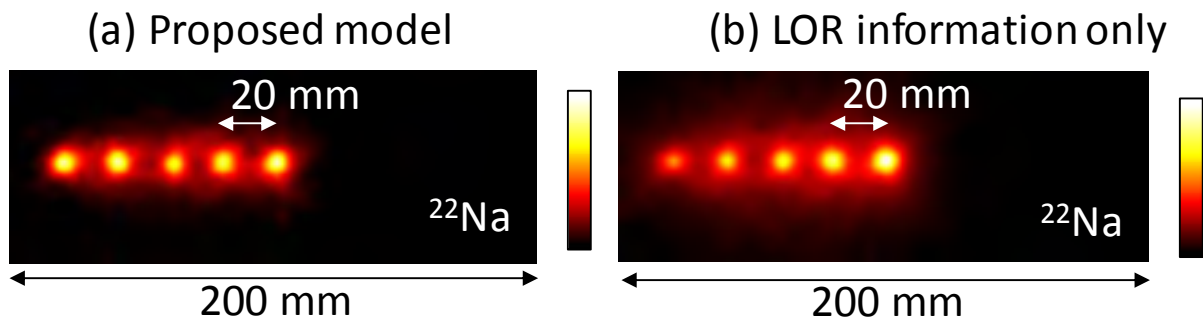

Figure 2. WGI images of ^{22}Na generated by simple back projection using the proposed detector response model (a) and using LOR information only (b).

4. Discussion

In this study, we used ^{22}Na to demonstrate the effectiveness of the detector response model proposed to make clear images for the 3-gamma imaging of the WGI. While the ^{22}Na cannot be used for biological subjects due to its long half-life, ^{44}Sc has the most appropriate candidate for its suitable half-life of 4 h and single gamma energy of 1.157 keV. We are currently working on the application of the 3-gamma imaging using ^{44}Sc with a collaboration with pharmaceutical study groups.

5. Conclusions

We proposed the detector response model necessary to realize the 3-gamma imaging, one of the WGI concepts, and we applied the model to the ^{22}Na data measured by the WGI prototype. The result showed that 3-gamma imaging is possible with the model and the consideration of the 3-gamma response improved clearness of the image.

Acknowledgments

References

[1]	C. Grignon, J. Barbet, M. Bardiès, et al., "Nuclear medical imaging using β+γ coincidences from 44Sc radio-nuclide with liquid xenon as detection medium. Nucl Instr Meth Phys Res Sect A, 571, pp. 142-145, 2007.

[2]	C. Lang, D. Habs, K. Parodi, et al., "Sub-millimeter nuclear medical imaging with high sensitivity in positron emission tomography using β+γ coincidences," Journal of Instrumentation, 9, P01008, 2004.

[3]	Z. Liang and R. Jaszczak, "Comparisons of multiple photon coincidence imaging techniques," IEEE Trans. Nucl. Sci., 37, pp. 1282-1292, 1990.

[4]	C. Müller, M. Bunka, J. Reber, et al., "Promises of Cyclotron-Produced 44Sc as a Diagnostic Match for Trivalent β$^-$-Emitters: In Vitro and In Vivo study of a ^{44}Sc-DOTA-Folate Conjugate," J. Nucl. Med., 54 (12), pp. 2168-2174, 2013.

[5]	E. Yoshida, H. Tashima, Y. Okumura, et al., "Concrete realization of the whole gamma imaging concept," IEEE NSS&MIC: M-21-2, Atlanta, 2017.

Geant4 simulation of whole-gamma imaging system using silicon scatterer detectors for low-energy imaging

Fumihiko Nishikido[1], Yusuke Okumura[1], Eiji Yoshida[1], Hideaki Tashima[1] and Taiga Yamaya[1]

[1] National Institute of Radiological Sciences (NIRS-QST), Japan

Abstract

Whole gamma imaging (WGI) is our concept to combine PET and Compton imaging so as to utilize all measured gamma rays for imaging. In the last year, we developed the first WGI prototype which used GSO scintillation detectors for the absorber and GAGG scintillation detectors for the scatterer. However, the energy resolution of the scatterer was much worse than the best energy resolution which have been reported for GAGG, and the limited energy resolution resulted in degraded performance of the Compton imaging. An alternative approach, we investigated the use of a silicon (Si) detector for the scatterer. We investigated performance of the WGI with the Si scatterer detector by Geant4 simulation. We compared performances between the first WGI prototype (GAGG +GSO WGI) and the WGI with Si scatterer (Si +GSO WGI). In the simulation, the total sensitive volume of the scatter for both WGI was almost same. As a result, the Si +GSO WGI achieved better angular resolutions than those of the GAGG +GSO WGI for all gamma ray energies. Although the sensitivity of the Si +GSO WGI was about lower than that of the GAGG +GSO WGI for high energy gamma rays, higher sensitivity was achieved for low energy gamma rays due to high scattering fraction of silicon. It is concluded that the WGI with the Si scatterer can improve spatial resolution of Compton imaging.

1. Introduction

A Whole gamma imaging (WGI) is our concept to combine positron emission tomography (PET) and Compton imaging so as to utilize all measured gamma rays for imaging. In the last year, we developed the first WGI prototype, in which an additional scatterer detector ring was inserted in the bore of a PET ring[1]. The PET detectors were used not only for PET measurement but also as an absorber in the Compton imaging. For a triple-gamma-ray (i.e., $\beta^+ + \gamma$) emitting radionuclide such as ^{44}Sc (two 511 keV + 1157 keV photons), which emits two annihilation radiations and single gamma rays almost at the same time, the source position on the line of response can be determined by a Compton cone (here we call this triple-gamma imaging) (Fig.1).

The prototype WGI system used GSO scintillation detectors for the absorber and GAGG scintillation detectors for the scatterer. The GSO detectors had 4-layer DOI capability. The scatterer consisted of a single-layer GAGG scintillator array coupled with a multi-pixel photon counter (MPPC) array. However, the energy resolution of the scatterer was much worse than the best energy resolution which have been reported for GAGG, and the limited energy resolution resulted in degraded performance of the Compton imaging. We thought this was due to the saturation effect of the MPPCs.

As an alternative approach, we investigated the use of a silicon (Si) detector for the scatterer. Although the density of Si is much smaller than that of GAGG, potentially good energy resolution of Si may work well especially for lower energy gamma-rays. In this paper, we report simulation results of between the first WGI prototype (GAGG +GSO WGI) and the WGI with Si scatterer (Si +GSO WGI) by Geant4 simulation[2] [3].
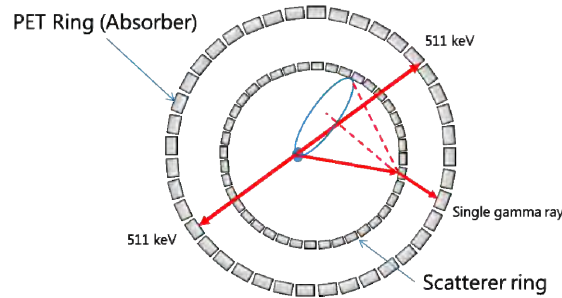

Figure 1. Principle of the triple-gamma imaging with WGI.

2. Methods

In order to estimate performance of the WGI using the Si absorber, we compared performances between the 1st WGI prototype (GAGG+GSO WGI) and the WGI with Si absorber (Si+GSO WGI) by Geant4 simulation. Simulation geometries are shown in Fig. 2. The PET scanner (i.g. absorber) consisted of 4 rings of 24 PET detectors. Each PET detector consisted of a $16 \times 16 \times 4$-layer array of GSO crystals (1.9 mm $\times$ 1.9 mm $\times$ 4.0 mm). The diameter of the PET ring was 66 cm. Table 1 summarize parameters of the scatterer detector of both WGI systems. The scatterers of the GAGG+GSO WGI consisted of a $16 \times 16 \times$ 1-layer array of GAGG crystals. The 20 scatterers were arranged in a ring structure and the number of rings was 2. As a result, the ring diameter and axial field of view were 20 cm and 5.2 cm, respectively. The simulation parameters of the Si detector for the simulation were the same as those of the Si chip which we are developing. The segment pitch assumed in the simulation was 0.9 mm $\times$ 0.9 mm. The thickness of the Si chip was 0.6 mm. The 10 Si chips were stacked to obtain the same thickness as the scatterers of the GAGG+GSO WGI. The 10 Si scatterers were also arranged in ring structure and the number of rings was 1. As a result, the ring diameter and axial field of view were 20 cm and 4.32 cm, respectively. Therefore, the total volumes of both scatterers were almost the same. Energy resolution for the GAGG and Si were set to 16.9 % and 0.62% at 511 keV, respectively. A point source was located at the center of the detector rings. Three gamma-ray energies (320, 511 and 1157 keV) were used in the simulations.
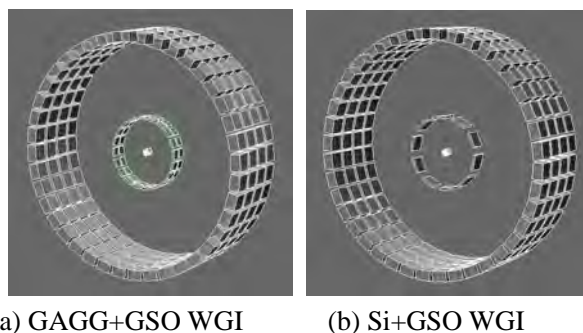
(a) GAGG+GSO WGI   (b) Si+GSO WGI

Figure 2.Simulated geometries.

Table 1. Parameters of the scatterer detectors used in the simulation

	GAGG scatterer	Si scatterer
Material	GAGG	Silicon
Segment pitch	1 mm × 1 mm	0.9 mm × 0.9 mm
Thickness	6 mm	0.6 mm
Array size of detectors	24 mm × 24 mm	48 mm × 48 mm
Num. of layers	1	10
Total thickness of detectors	6 mm	6 mm
Num. of detectors in each ring	20	10
Num. of rings	2	1

3. Results

Figure 3 shows the angular resolution measure (ARM) for each measurement condition. Gaussian curve fitting was applied and FWHMs were calculated to evaluate the angular resolution. The angular resolutions of the GAGG+GSO WGI were 31.67, 19.95 and 8.67 deg for 320, 511 and 1157 keV gamma rays, respectively. The angular resolutions of the Si+GSO WGI were 9.05, 4.29 and 2.60 deg for the respective gamma ray energies. Table 2 summarizes the ARMs for all simulation conditions. Sensitivity was calculated from the number of coincidence events in two detectors. Table 3 shows the sensitivities of the two different absorbers. The sensitivities of the GAGG+GSO WGI were 0.074, 0.244 and 0.225% for 320, 511 and 1157 keV gamma-rays, respectively. The sensitivities of the Si+GSO WGI were 0.080, 0.105 and 0.074% for the respective gamma-ray energies
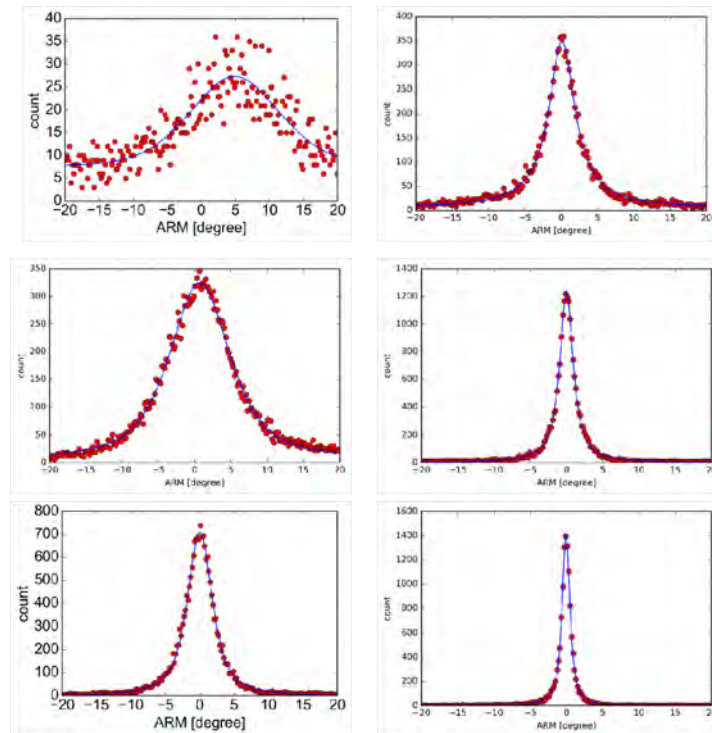

Figure 3.ARM distribution of the two different absorbers for 320, 511 and 1157 keV gamma-rays.

Table 2. Angular resolution in FWHM of the two different absorbers for 320, 511 and 1157 keV gamma-rays.

	320 keV	511 keV	1157 keV
GAGG	31.67°	19.95°	8.67°
Si	9.05°	4.29°	2.60°

Table 3. Sensitivity of the two different absorbers for 320, 511 and 1157 keV gamma-rays

	320 keV	511 keV	1157 keV
GAGG	0.074 %	0.244 %	0.216 %
Si	0.080 %	0.105 %	0.073 %

4. Discussions and conclusions

We investigated the use of the Si detector for the scatterer by Geant4 simulation. Simulation results showed that the WGI with the Si scatterer could improve spatial resolution of Compton imaging. One issue was the efficiency, but we showed that Si worked well for lower energy gamma-rays. Now, we are developing double-sided strip silicon detector for the scatter detector and will evaluate performances of the developed Si detector in the future work.

References

[1] T. Yamaya, E. Yoshida, H. Tashima, et al., "Concrete realization of the whole gamma imaging concept," 2017 IEEE NSS & MIC, M-21-2, 2017.

[2] S. Agostinelli, J.Allison, K.Amako, et al., "Geant4—a simulation toolkit," Nucl. Instrum. Methods Phys. Res. A 506, 250–303, 2003

[3] J.Allison, K.Amako, J. Apostolakis, et al., "Geant4 developments and applications," IEEE Trans. Nucl. Sci. 53 270–8, 2006

In-beam PET measurement of washout in rabbit using ^{11}C and [15]O ion beams

C Toramatsu[1, 2], H Wakizaka[1], A Mohammadi[1], M Nitta[1], Y Iwao[1], F Nishikido[1], E Yoshida[1],
A Kitagawa[1], Y Hirano[3] and T Yamaya[1]

[1] National Institute of Radiological Sciences (NIRS-QST), Japan

[2] Tokyo Women's Medical University, Tokyo Japan

[3] Nagoya University, Nagoya, Japan

Abstract

In particle therapy, in-beam positron emission tomography (PET) is expected to enable *in situ* noninvasive confirmation of the treatment delivery. For accurate range and dose verification or three-dimensional (3D) volume imaging, however, correction of the biological washout effect in a living body is necessary. In this study, we implanted ^{11}C and [15]O ion beams into rabbit brain, and observed the diffusion process to the whole body. Data were acquired by our large-bore in-beam PET 6th-prototype, which enables 3D in-beam imaging. Regions of interests (ROIs) were set as a 3D positron distribution and the time activity curves (TACs) of the brain, heart and lung region were acquired. A difference between diffusion process in ^{11}C ions and the [15]O ions was observed. This study provided the new data to investigate the biological washout mechanism.

1. Introduction

In-vivo monitoring of the range is a key enabler for precise particle therapy. A practical approach is PET imaging of positron emitters generated through fragmentation reaction, however, correction of biological washout is essential. The main positron emitters are [11]C ($T_{1/2} = 20.39$ min) and [15]O ($T_{1/2} = 2.03$ min) produced by the (p, pn) reaction channels of ^{12}C and [16]O in the patient soft tissue, respectively. Especially for in-beam or in-room PET, [15]O is the prevalent contributor, due to its short half-life. In previous study, we measured washout rate in a rabbit brain, and a difference between washout speed in carbon ions and the oxygen ions was observed[1]. In this study, we observed diffusion process of implanted oxygen ions as well as carbon ion beam in rabbits to provide accurate modelling of the biological washout.

2. Methods

Radionuclide beams of ^{11}C and [15]O were generated as secondary beams in the HIMAC. And the brain of anaesthetized rabbits were irradiated with these two radionuclide beams. PET imaging was started simultaneously with the start of irradiation using our original large-bore in-beam PET 6th-prototype. Experimental set up was shown in figure 1. ROIs were set in 3D-PET images and TACs of the ROIs were acquired. The washout rate was obtained based on the multiple component model analysis[2].
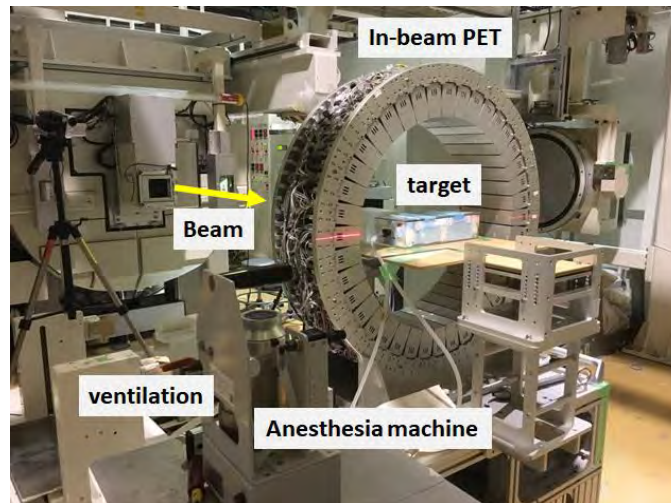
Figure 1. The experimental setup with the large-bore in-beam PET 6th-prototype for rabbit brain irradiation.

3. Results

PET image revealed that implanted ^{11}C and ^{15}O ion beam in brain diffused out in entire body in few seconds after irradiation due to washout effect. Figure 2 shows spatial distributions in the whole rabbit body (summed images of 10 minutes measurement) of (a) ^{11}C and (b) ^{15}O irradiations. Images were fused with the CT image. The PET intensity was concentrated in the regions that had high blood volume. In the case of ^{11}C irradiation, TACs of ROI value in heart and lung showed single exponential decay [Figure 3 a) and b)], while two components in the washout process were observed in the case of ^{10}O irradiation [Figure 3 c) and d)].
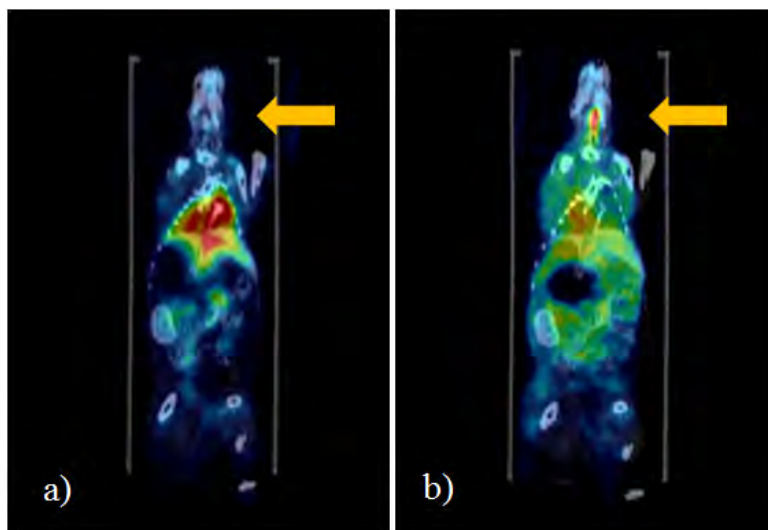

Figure.2 PET images of Rabbit whole body fused with CT image in condition of (a) ^{11}C and (b) ^{15}O irradiation.
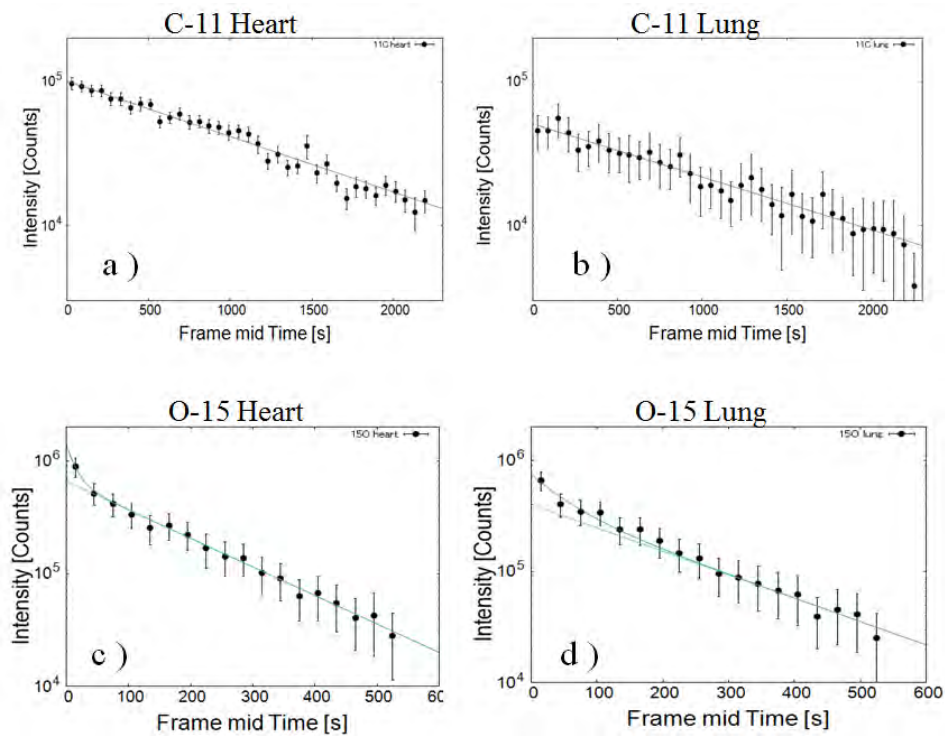
Figure.3 TACs of heart (a) and lung (b) with fitting results in condition of ^{11}C irradiation, and that of heart (c) and lung (d) in condition of ^{15}O irradiation.

4. Conclusions

These results suggested that implanted ^{11}C and ^{15}O ion beam washed out and circulated in entire body of rabbit. The speed and ratio of washout vary by each ion beam and by each organ. This study provided important data to investigate the biological washout mechanism and establish an accurate washout correction model.

Acknowledgments

References

[1]   Toramatsu, C., et al.: Washout effect in rabbit brain: in-beam PET measurements using 10C, 11C and 15O ion beams. *Biomedical Physics & Engineering Express*, *4*(3), 035001.

[2]   Mizuno H et al 2003 Washout measurement of radioisotope implanted by radioactive beams in the rabbit Phys. Med. Biol. 48 2269–81